Self-healing Function of Various Oxide Ceramic-based Nanocomposites Dispersed Ni Particles

(Ni 粒子を分散した各種酸化物セラミック基ナノコンポジットの自己治癒)

PHAM VU HAI

Graduate School of Engineering
Nagaoka University of Technology

Research Supervisor

Associate Professor NANKO MAKOTO

Department of Mechanical Engineering
Nagaoka University of Technology
Nagaoka, Niigata 940-2188, Japan

Abstract

Aim of the present dissertation is to develop the self-healing function of ceramic-based composites for high-temperature applications such as gas turbine engines or jet engines. Engineering ceramics have many excellent properties that are suitable for high-temperatures applications. Unfortunately, applications of ceramics must face huge challenges on their brittle property due to the covalent and ionic bonds. Over the last few decades, many studies have been conducted to fabricate ceramic-based composites incorporated with non-oxide phases for toughening the ceramics. The recent interests on ceramic-based composites are the self-healing functions induced by the oxidation of non-oxide phases at high temperatures. Oxidation of the non-oxide phases develops oxidation products which fill up surface cracks. This effect causes the reduction of stress concentrations at crack tips and consequently involves in strength recovery. The mechanism of self-healing function is attributed to the volume expansion and/or the diffusion of cations caused by oxidation of non-oxide phases within the matrices. From this inspiration, self-healing functions of Ni/Al_2O_3, Ni/(ZrO_2+Al_2O_3) and Ni/mullite nanocomposites are investigated and discussed in this present dissertation. Investigation of self-healing function for each nanocomposite is conducted and discussed via mechanical properties, surface crack-disappearance by thermal oxidation, self-healing-induced strength recovery and oxidation resistance. High-temperature bending tests are applied to estimate the self-healing performance of Ni/Al_2O_3 and Ni(ZrO_2+Al_2O_3) nanocomposites at high temperatures. Influences of Al_2O_3 grain size on self-healing effectiveness as well as oxidation resistance of Ni/Al_2O_3 nanocomposites are discussed from the oxidation kinetic

point of view. Influence of YZ (Y_2O_3 stabilized tetragonal ZrO_2) on self-healing performance of Ni/(YZ+Al_2O_3) nanocomposites is also discussed. Based on the investigations of self-healing function for alumina-based and mullite-based composites, the roles of matrices on self-healing performance are discussed.

Ni/Al_2O_3 nanocomposites exhibit a great self-healing performance at high temperatures caused by the oxidation of Ni particles. Ni/Al_2O_3 nanocomposites could be suitable for the components in hot sections of gas turbine engines. However, high-temperature strength of Ni/Al_2O_3 nanocomposites must be improved. Dispersion of YZ is one of the solutions for high-temperature strength of Ni/Al_2O_3 nanocomposites. YZ dispersion does not influence significantly on self-healing performance. Nevertheless, YZ accelerates the oxidation rate of the composites. For further studies, the oxidation resistance of Ni/(YZ+Al_2O_3) could be improved by dopants of silicon carbide (SiC), silicon (Si) or yttrium (Y). Ni/mullite nanocomposites possess the best self-healing performance among the investigated composites. With a great oxidation resistance and excellent self-healing performance, Ni/mullite nanocomposites are potential for high-temperature applications. For further applications, mechanical properties of Ni/mullite must be improved.

Acknowledgements

First and foremost I would like to thank my advisor, Prof. Nanko Makoto. It has been an honor to be his Ph.D. student. I greatly appreciate all his contributions of time, ideas, and funding to make my Ph.D. experience productive and stimulating. The joy, enthusiasm and optimism he has for research was contagious and motivational for me, even during tough times in the Ph.D. pursuit. I am also thankful for all the advice, supports he has given me for my life in Japan. He has been an excellent example as a successful scientist and professor who has inspired me not only in my research but also in my life.

I would like to acknowledge the members of Nanko Laboratory, who have contributed immensely to my personal and professional time at Nagaoka. The group has been a source of friendships as well as good advice and collaboration. I am especially grateful for helps of Daisuke Maruoka, Hitoshi Abe, Teppei Tsuzuki, who stuck with me in my research. I also would like to appreciate Mai Dung Do, Khanh Dang, Hien Nguyen, for always helping me during my stay in Nagaoka. Other past and present group members that I have had the pleasure to work with or alongside are Suares-Vazquez Santiago, Assayidatul Laila, Hiroki Yoshikawa, Takahiro Kamoda, Kazuki Onoda.

The studies of high-temperature bending strength discussed in this dissertation would not have been possible without the high-temperature bending test equipment at Nakao Laboratory at Yokohama National University. I am particularly indebted Prof. Wataru Nakao and his students for their discussions, collaboration and hospitality during my stay at Yokohama.

In regards to the micro Vickers hardness tester, I thank Prof. Shigeharu Kamado (Nagaoka University of Technology) and his students. They have helped me with the operating instructions and allowed me using the instrument.

In my later work of characterizations for oxidation products on Ni/mullite system, I am thankful to Prof. Yuichi Otsuka in Nagaoka University of Technology for helping me

with the operation of Raman spectroscopy. He gave me some advice and spent his valuable time to help me clarifying the oxidation products of Ni/mullite system.

For the studies on high-temperature oxidation, I have appreciated Prof. Thuy Dang Nguyen (Hanoi University of Science and Technology) and Prof. Shigenari Hayashi (Tokyo Institute of Technology) who have spent time discussing with me. I am especially grateful for discussions and advice from Prof. Hayashi on oxidation kinetics and influences of Al_2O_3 grain boundaries on oxidation behavior at high temperatures of Ni/Al_2O_3 composites.

For this dissertation, I would like to thank my reading and oral defense committee members: Prof. Masakazu Okazaki, Prof. Yukio Miyashita, Prof. Tomoyuki Homma, and Prof. Wararu Nakao for their time, interest, helpful comments and insightful questions.

I gratefully acknowledge the funding sources that made my Ph.D. work possible. My work was financial supported by the Japan Science and Technology Agency in the frame of the Advanced Low Carbon Technology Research and Development program. I was honored to be granted a scholarship for the last two years of Ph.D. course from the Kyoritsu International Foundation.

My time at Nagaoka was made enjoyable in large part due to the many friends and groups that became a part of my life. I am grateful for time spent with friends, for my backpacking buddies and our memorable trips into many places in Japan, and for many other people and memories.

Lastly, I would like to thank my family for all their love and encouragement. For my parents who supported me in all my pursuits. For my beloved uncle, Dr. Cuong Kien Ngo, who has inspired me with a love of science and encouraged me in every pursuit in my life. For my brother, who has been my left hand and my right hand, my confidant and my friend in Vietnam when I am away from home. Thank you.

Hai Vu Pham
Nagaoka University of Technology
March 2016

List of contents

List of Tables

List of figures

Chapter I
Introduction

1.1 Ceramics.

Engineering materials are often divided into three primary distinct classes, metals, ceramics and polymers, based on the types of atoms involved and bonding between them. Composites are combinations of more than one material and often involve ceramics, as schemed in Figure 1.1. Metals consist of atoms held together by delocalized electrons that overcome the mutual repulsion between the ion cores. The delocalized electrons give metals many characteristic properties such as good thermal and electrical conductivity. Because of their bonding, many metals have close packed structures and plastically deform at room temperature. Polymers are macromolecules formed by covalent bonding of many simpler molecular units which are called mers. The bonding between the molecular chains controls many of their properties. Ceramics are usually associated with mixed bonding, a combination of covalent, ionic bonds and sometimes metallic bonds. Figure 1.2 shows the differences in atom bonding of metals and ceramics. The structure of metallic bond is very different from that of covalent and ionic bond. The ionic bonds join metals to nonmetals, covalent bond join nonmetals to nonmetals and the metallic bonds are bonding between metal atoms. Due to the metallic bonds in metals, local bonds can be easily broken and reformed that gives metals many unique properties. Unlike the metallic bonds in metals, covalent and ionic bonds in ceramics determine many of their characteristic properties such as brittleness, poor electrical and thermal conduction and so on [1-3].

The brittleness of ceramics can be recognized from personal experience, such as dropping a dinner plate. The reason that the majority of ceramics are brittle is the mixed ionic-covalent bonds. The valence electrons in ionic-covalent bonds are transferred or shared to each other. The electrons are thus strongly bonded and unable to delocalize as electrons in metallic behave. It is also the reason of the poor electrical and thermal conduction of ceramics. The valence electrons are tied up in bonds and are not free as

they are in metals. Beside the properties mentioned above, ceramics are known as great materials that have good compressive strength, chemical insensitivity and transparent.

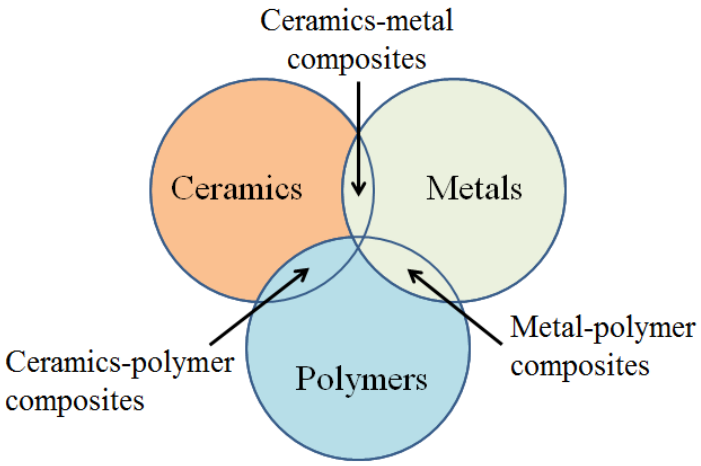

Fig. 1.1. Venn diagram of three primary distinct material classes and their composites.

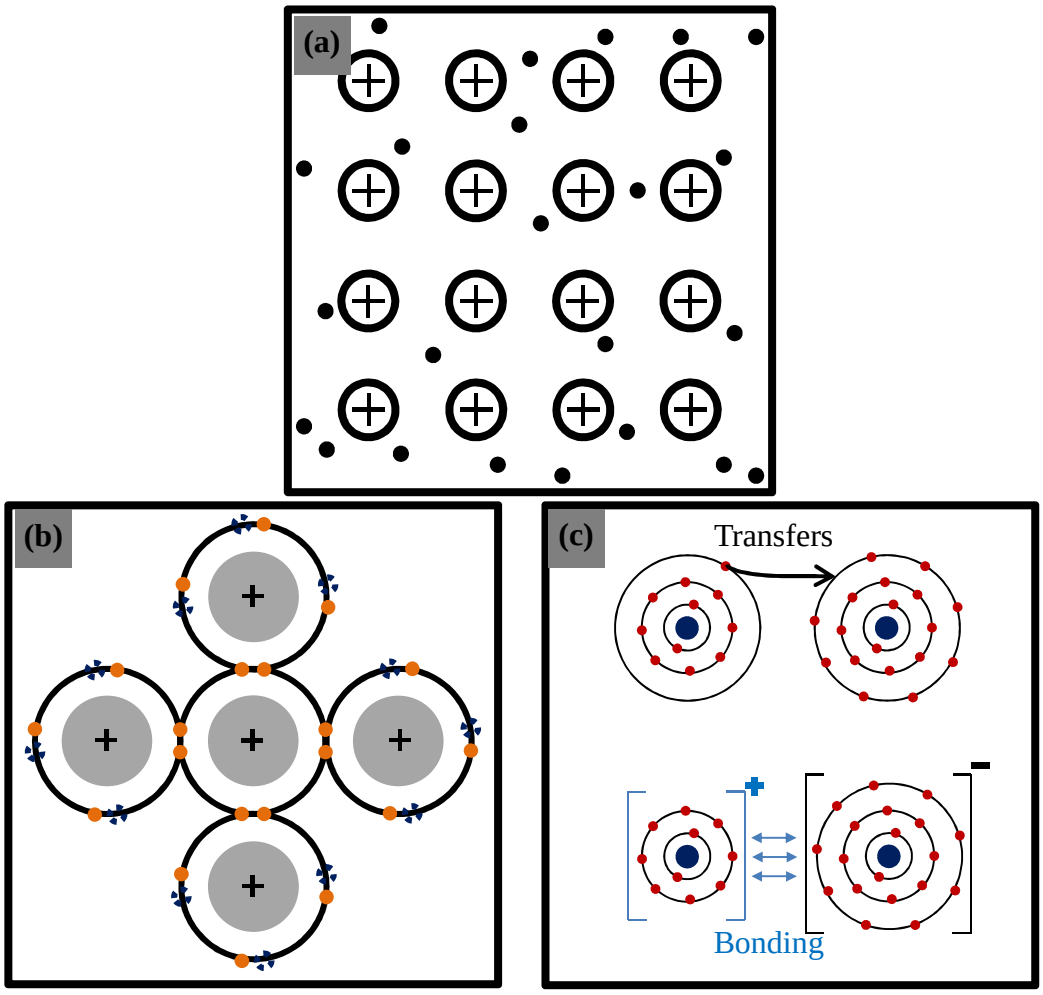

Fig. 1.2. Illustrations demonstrate the atom bonds in (a) metallic bonds, (b) covalent bonds and (c) ionic bonds.

1.2 Applications of Ceramics.

Ceramics are the oldest materials made by humans and also among the most recent materials utilized today. The applications of ceramics are diverse from bricks and tiles to electronic and magnetic components [4], as shown in Table 1.1. Use of ceramics is commonly classified as traditional and advanced ceramics. Traditional ceramics which include high-volume items such as bricks and tiles, toilet bowls, and pottery are usually based on clay and silica. Nowadays, they can be produced either by traditional methods or advanced manufacturing techniques with computer-assisted process control. The advanced ceramics are also referred as special, technical or engineering ceramics. Whereas the traditional ceramics are usually manufactured in high-volume, the advanced ceramics are often produced in small quantities at higher prices. The advanced ceramics exhibit superior mechanical properties, corrosion/oxidation resistance, or electrical, optical and/or magnetic properties. Unlike the traditional ceramics have been utilized for over 10,000 years, advanced ceramics have generally been developed only within the last 100 years. With the rapid development of technology, advanced ceramics are expecting to be one of the important engineering materials.

One of the recent interests on advanced ceramics is the applications at high temperatures such as gas turbines and jet engines. Fig. 1.3 shows the schematic diagram of a gas turbine engine. When the engine is started, the compressors in the cold section compress the intake air which is mixed with fuel in the hot section combustor. The hot gases drive the turbine section. The turbine blades thus work under a severe environment. The turbine blades utilized todays are composed of Nickel-based superalloys which are operated at high temperatures up to 1370ºC [5-8]. To protect the Ni based superalloys from damage due to oxidation, creep, melting, thermal fatigue, and stress-induced fatigue failures, the blades are air cooled and applied low thermal conductivity coatings. Even though the Ni based superalloys are protected with the coating layers, they are still operated at 1000ºC where the superalloys exhibit poor strength. On the other hand, the turbine engines must increase the operation temperature to improve the efficiency [9]. It is necessary to seek for potential materials that are able to operate at higher temperatures.

Engineering ceramics are refractory materials, thus suitable for these applications. Unfortunately, they are brittle materials with low fracture toughness. In order to meet the demand for increasing their fracture toughness, many attempts have been made to fabricate ceramic-based composites incorporated with metallic and/or non-metallic dispersoids. With the numerous interests and studies focus on the development of ceramic matrix composites, the materials are approaching to meet all the demands for the next generation of gas turbine engines.

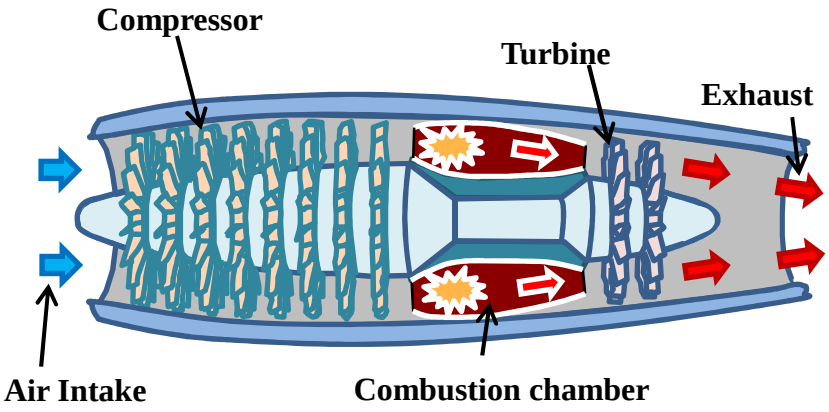

Fig. 1.3. Schematic diagram of a gas turbine engine.

Table 1.1 Properties and Applications for Ceramics [4].

Property	Example	Application
Electrical	$Bi_2Ru_2O_7$	Conductive component
	Doped ZrO_2	Electrolyte in solid-oxide fuel cells
	Indium tin Oxide (ITO)	Transparent electrode
	SiC	Furnace elements for resistive heating
	$YBaCuO_7$	Superconducting quantum interference
	SnO_2	Electrodes for electric furnaces
Dielectric	α-Al_2O_3	Spark plug insulator
	$PbZr_{0.5}Ti_{0.5}O_3$ (PZT)	Micropumps
	SiO_2	Furnace bricks
	(Ba,Sr) TiO_3	Dynamic random access memories
	Lead magnesium niobate	Chip capacitors
Magnetic	γ-Fe_2O_3	Recording tapes
	$Mn_{0.4}Zn_{0.6}Fe_2O_4$	Transformer cores in touch tone phones
	$BaFe_{12}O_{19}$	Permanent magnets in loudspeakers
	$Y_{2.66}Gd_{0.34}Fe_{4.22}Al_{0.68}Mn_{0.09}O_{12}$	Radar phase shifters
Optical	Doped SiO_2	Optical fibers
	α-Al_2O_3	Transparent envelopes in street lamps
	Doped $ZrSiO_4$	Ceramic colors
	Doped (Zr,Cd)S	Fluorescent screens (electron microscope)
	$Pb_{1-x}La_x(Zr_zTi_{1-z})_{1-x/4}O_3$ (PLZT)	Thin-film optical switches
	Nd doped $Y_3Al_5O_{12}$	Solid state lasers
Mechanical	TiN	Wear-resistant coatings
	SiC	Abrasives for polishing
	Diamond	Cutting tools
	Si_3N_4	Engine components
	Al_2O_3	Hip implants
Thermal	SiO_2	Space shuttle insulation tiles
	Al_2O_3 and AIN	Packages for integrated circuits
	Lithium-alumino-silicate glass ceramics	Supports for telescope mirrors
	Pyrex glass	Laboratory glassware and cookware

1.3 Ceramic-based composites.

Ceramic based composites were fabricated and studied because of the major concern on the low fracture toughness with poor reliability of ceramic matrix. The desire to toughen ceramics is not new. For instance, toughening of brick using straw was known in ancient times. The basic idea is how to stop crack propagation. Nowadays, a number of potential toughening mechanisms have been proposed [10-12]. The ceramic-based composites may be fabricated with incorporation of platelets [13-16], fibers or whiskers [17-20], particulates [21-26], nanotubes or nanosheet [27-29] for toughening. Depending on the geometry and characteristic, the dispersoids act as crack inhibitors with different mechanisms [30, 31]. The toughening mechanisms for ceramics are summarized in Table 1.2 [4]. The most common toughening mechanisms are described as shown in Fig. 1.4. With the differences in volume fraction of reinforcement, Young's modulus of matrix and reinforcement and strength of the matrix/reinforcement, the effectiveness of reinforcement may be very varied. Among the above mechanism, fiber-reinforced ceramic composites is one of the most successful techniques [32].

Table 1.2 Classification of toughening mechanisms in ceramics [4].

General mechanism	Detailed mechanisms
● Crack deflection	Tilt and twist out of crack plane around grains and second-phase additions.
● Crack bowing	Bowing in crack plane between second-phase crack-pinning points
● Crack branching	Crack may subdivide into two or more roughly parallel cracks
● Crack tip shielding by process zone activity	Microcracking Transformation toughening Ductile yielding in process zone
● Crack tip shielding by crack bridging	Second-phase brittle fibers with partial debonding Frictional and ligamentary grain bridges Second-phase ductile ligament bridging

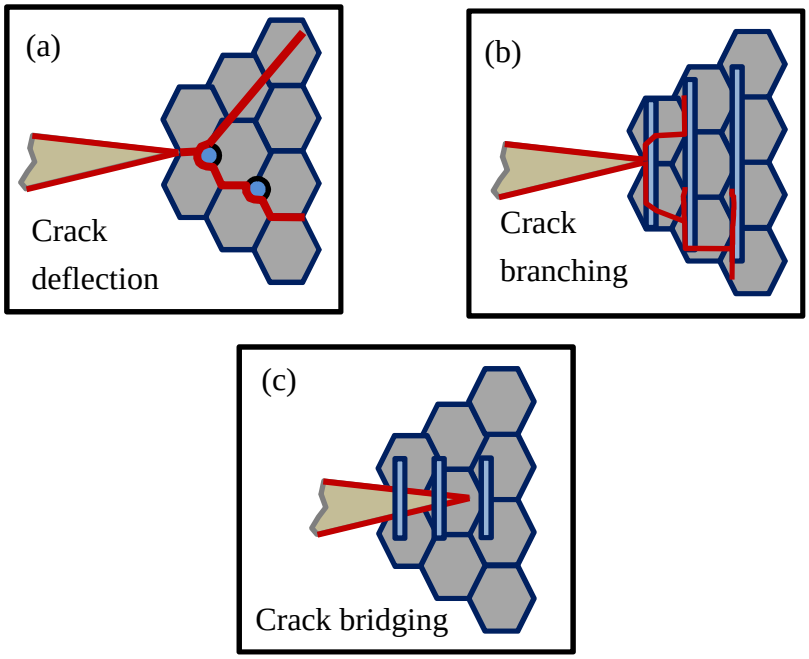

Fig. 1.4. Schematic diagram shows the toughening mechanisms in ceramic matrix composites, (a) crack deflection, (b) crack branching and (c) crack bridging.

With regards to fiber-reinforcement ceramic composites, *Nakao* proposed a new concept in material design in which, the fiber reinforcement ceramic composites associate with self-healing function [33]. Fig. 1.5 shows the illustration to describe this idea. The fiber bundles, which are coated by non-oxide interlayers, reinforce in ceramic matrix. With this structure, the composites are expecting to have higher fracture toughness obtained by fiber pull-out effect. The pull-out effect in fiber reinforced ceramic is caused by the slip of the interface between fiber and matrix during crack propagation. Besides, the occurrence of cracking can be recovered by the self-healing function at high temperatures. The interlayers are exposed in the air at high temperatures by crack propagation. Oxidation of the interlayers produces the oxidation product which acts as a healing material. Hence, the fiber reinforced self-healing ceramics are anticipated to serve longer time and more reliable with the ability of healing by itself. With respect to this proposal, the ceramic matrix must have the self-healing function as well.

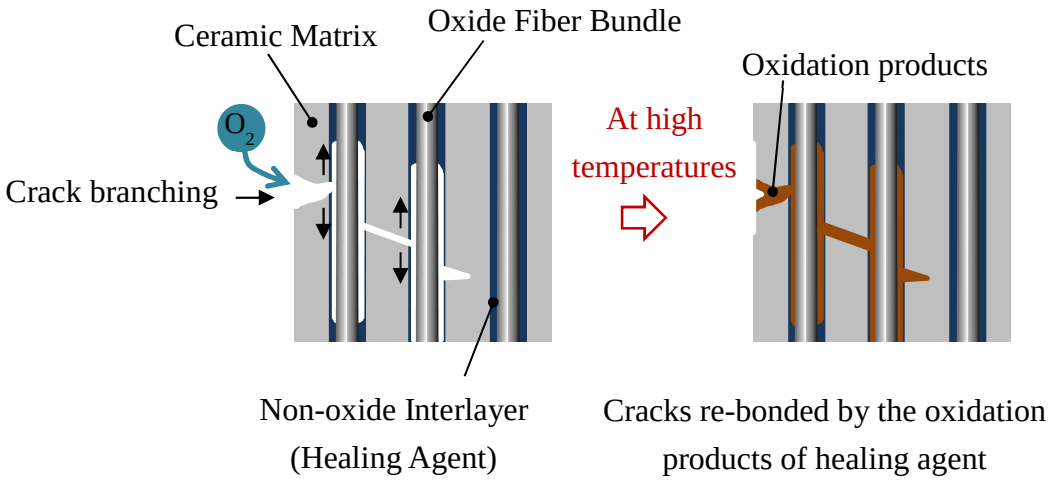

Fig. 1.5. Schematic illustrates the toughening mechanism and self-healing function of fiber reinforcement ceramic matrix composites proposed by Nakao [33].

1.4 Self-healing function of ceramics based-composites.

Self-healing in ceramics can be traced back to 1970's [34, 35] when the idea was to heal the surface cracks caused by grinding, cutting, thermal shocking, impacting and so on. The monolithic alumina was heat-treated up to 1700 or 1900ºC in order to gain its strength recovery. Although, its result of 4-point bending tests shows less effective on strength recovery. For instance, by heat-treatment at 1900ºC, bending strength of the sample recovered from 35.9 to 148 MPa which was much lower than that of as-received one (323 MPa). The crack-healing mechanism at that time was the re-sintering process where cracks seem to heal via the disappearance of void space between adjacent grains. Due to the less effectiveness and complex requirements for crack-healing, this approach has limited work attributed to it today.

Self-healing in ceramics only has been developed rapidly since 1992 when *Choi* et al. reported the self-healing function obtained in silicon nitride (Si_3N_4) ceramics [36]. The Si_3N_4 ceramics containing MgO additives were oxidized at high temperatures and formed $MgSiO_3$ accompanied with N_2 gas. The oxidation kinetics of this system was controlled by the diffusion of Mg^{2+} through the grain boundary toward the surface. The outward

diffusion of Mg^{2+} created an oxidation product layer which healed surface cracks and resulted in strength recovery. However, more extensive oxidation leads to strength degradation due to formation of new flaws by the evolution of N_2 gas at the surface. Lately in 1995, *Chu* et al. developed the self-healing function in SiC/mullite composites [37]. The oxidation of SiC phase in mullite matrix at high temperatures induced the formation of oxidation products associated with volume expansion as shown in Fig. 1.6. The volume expansion caused the reduction of stress concentration on crack tips which consequently involved strength recovery. Since the study was reported, self-healing function of ceramic-based composites has been considered as a promising solution for high-temperature applications of ceramics.

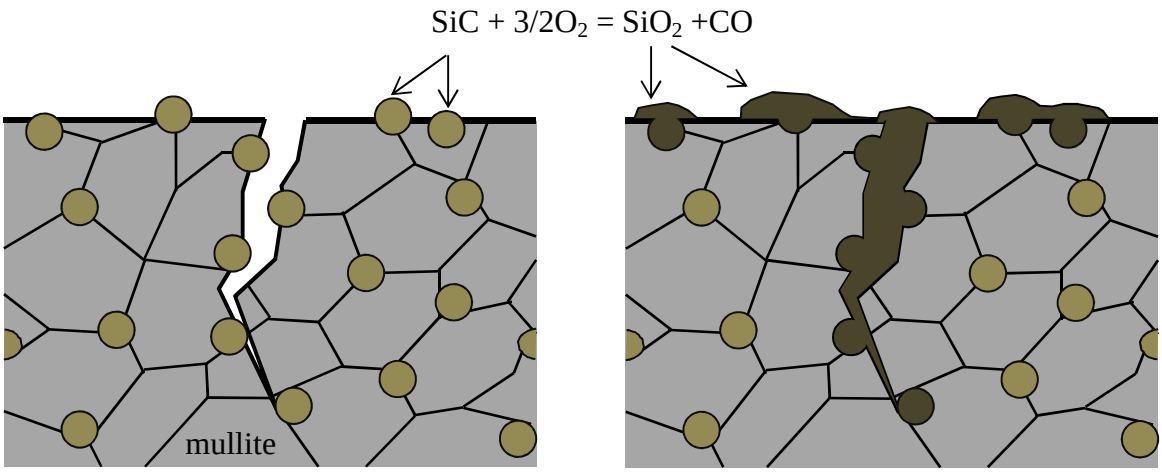

Fig. 1.6. Schematic illustrates the self-healing mechanism of SiC/mullite matrix composites.

Chapter II
Literature review and scope of the self-healing in ceramics

2.1 Self-healing in ceramics.

Since the self-healing of SiC/mullite was reported, numerous studies have been conducted for the development of self-healing ceramics. Table 2.1 describes ceramics and composites which have self-healing. In general, SiC dispersed ceramic matrices have self-healing function available at temperatures above 1300ºC. The self-healing mechanism of SiC dispersed ceramic matrices was attributed to the oxidation of SiC induced volume expansion. From this aspect, volume expansion factors of healing agents which undergo oxidation reaction were considered and shown in Table 2.2 [38]. Among the listed healing agents, $TiSi_2$ has the highest volume expansion factor (ϕ=1.67). As a consequence, $TiSi_2$/mullite has the self-healing function which is obtained by heat-treatment in air at 600ºC for 1 h [39]. However, the $TiSi_2$/mullite exhibits very poor mechanical strength (~180 MPa). Moreover, mechanical strength of the composite decreases as heat-treatment time increases.

In few rare cases, SiC/ZrO_2 composites exhibit the surface crack-disappearance obtained by heat-treatment at 800ºC in air [40]. However, bending strength of SiC/ZrO_2 degraded considerably from 700 MPa at room temperature to 180 MPa at 800ºC. To solve this problem, some attempts have been made to fabricate SiC/ZrO_2 associated with Al_2O_3 [41] or TiO_2 [42]. Nevertheless, adding more additives leads to increase the required temperature for self-healing.

Meanwhile, self-healing in some MAX phase ceramics such as Ti_3AlC_2 [43], $Zr_2Al_4C_5$ [44] and Cr_2AlC [45] have been reported as well. Most of the MAX phases possess impressive healing abilities because of significant formation of oxidation products at 1000ºC. Nonetheless, besides the positive products (Al_2O_3, TiO_2, ZrO_2), the oxidation process also induced the negative products such as CO_2 gas. For a long-term service, the flow of CO_2 gas leads to the formation of flaws at the surface which degrade the mechanical strength of the components. On the other hand, applications of these MAX

phases must be taken into consideration of their oxidation resistance due to their sensitive oxidation and active diffusion at high temperatures.

Table 2.1 Development of self-healing function in various ceramic matrices.

	Dispersoids (Healing Agent)		Matrices (Based Materials)	Oxidation products for self-healing	Healing Temp. *T*/ ºC	Strength recovery (*)	Ref.
Composites	SiC	Particles	Si_3N_4	SiO_2	~1300	O	[46, 47]
			Y_2O_3+Si_3N_4	SiO_2, Y_2SiO_7			[48-50]
			Al_2O_3	SiO_2			[51-54]
			Mullite	SiO_2			[55-57]
			Y_2O_3+Mullite	SiO_2, Y_2SiO_7			[58]
			$MgAl_2O_4$	SiO_2			[59]
			ZrO_2	SiO_2	~800	O	[40]
			Al_2O_3+ZrO_2	SiO_2	~1000	O	[41]
			TiO_2+ZrO_2	SiO_2			[42]
		Whiskers	Al_2O_3	SiO_2	~1300	O	[60]
		Particles & Whiskers	Mullite	SiO_2			[61]
	TiC		Al_2O_3	TiO_2	~1000	Δ	[62]
	$Ti_2Al_{0.5}Sn_{0.5}C$		Al_2O_3	TiO_2, SnO_2	~900	O	[63]
	$TiSi_2$		Mullite	TiO_2, SiO_2	~600		[39]
	Co		Al_2O_3	$CoAl_2O_4$	~1200	O	[64]
	NiAl		Al_2O_3	$NiAl_2O_4$			[23]
	Ni		Al_2O_3	$NiAl_2O_4$			[65]
	Mo		Al_2O_3	$Al_2(MoO_4)_3$	~700	X	[66-67]
	$MoSi_2$		Al_2O_3+ZrO_2	$ZrSiO_4$, Si-O	~1100	Δ	[68]
Monolithic	-		Ti_2SnC	TiO_2, SnO_2	~800	O	[69]
	-		Ti_3AlC_2	Al_2O_3, TiO_2	~1100	-	[43]
	-		$Zr_2Al_4C_5$	ZrO_2, Al_2O_3	~900	Δ	[44]
	-		Cr_2AlC	Al_2O_3, $(Cr,Al)_2O_3$	~1100	O	[45]
	-		$(MoNb)Si_2$	SiO_2, Nb_2O_5	~1200	O	[70]

(*) Strength recovery: (O) Full, (Δ) Partially; (X) No.

Table 2.2 Volume expansion factors of healing agents which undergo oxidation reaction.

Oxidation reaction	Volume expansion factor ϕ (ϕ=$\Delta V/V_o$)
$2Ti_2AlC+12/2O_2 \rightarrow 4TiO_2+Al_2O_3+2CO$	0.54
$Si_3N_4+3O_2 \rightarrow 3SiO_2+2N_2$	0.84
$SiC+3/2O_2 \rightarrow SiO_2+CO$	1.00
$Si+O_2 \rightarrow SiO_2$	1.07
$2CrSi_2+11/2O_2 \rightarrow Cr_2O_3+4SiO_2$	1.20
$TiSi_2+3O_2 \rightarrow TiO_2+2SiO_2$	1.67
$Ni+Al_2O_3+1/2O_2 \rightarrow NiAl_2O_4$	0.22

2.2 Self-healing ceramic composites by metallic-healing agents.

Self-healing function at high temperatures has been also reported lately for metal/ceramic-based composites such as Ni/Al_2O_3 [65], Co/Al_2O_3 [64], and Mo/Al_2O_3 [66]. Unlike the volume expansion-induced crack-disappearance of SiC/ceramic composites, the diffusion of metallic cations plays the major role in self-healing performance of metal/ceramic composites. With the diffusion mechanism, self-healing of metal/ceramics composites is expected to perform repeatedly. Fig. 2.1 demonstrates the oxidation mechanism which induces surface crack-disappearance of metal/ceramic composites. As soon as the composites are applied at high temperatures in the air, the metallic phase on the surface is oxidized. The oxidation of metallic phase induces the diffusions of metallic cations (M^{2+}) and oxygen ions (O^{2-}) which create the surface layer and oxidized zone. While the formation of the surface layer is responsible for self-healing function, the development of oxidized zone is representative for oxidation resistance of the composites. The developments of oxidized zone and the surface layer are very varied, depending on characteristics of dispersoids, matrix materials or dopants. For example, *Nanko* described the oxidation mechanism in various metal/ceramics composites [71]. In which, the inward diffusion of O^{2-} in Ni/ZrO_2 composites occurred much faster than the outward

diffusion of Ni^{2+}. Without the outward diffusion of Ni^{2+}, the oxidation of metallic phase caused the volume expansion which induced the formation of cracks at oxidized zone. This phenomenon caused the rapid formation of oxidized zone without the surface layer.

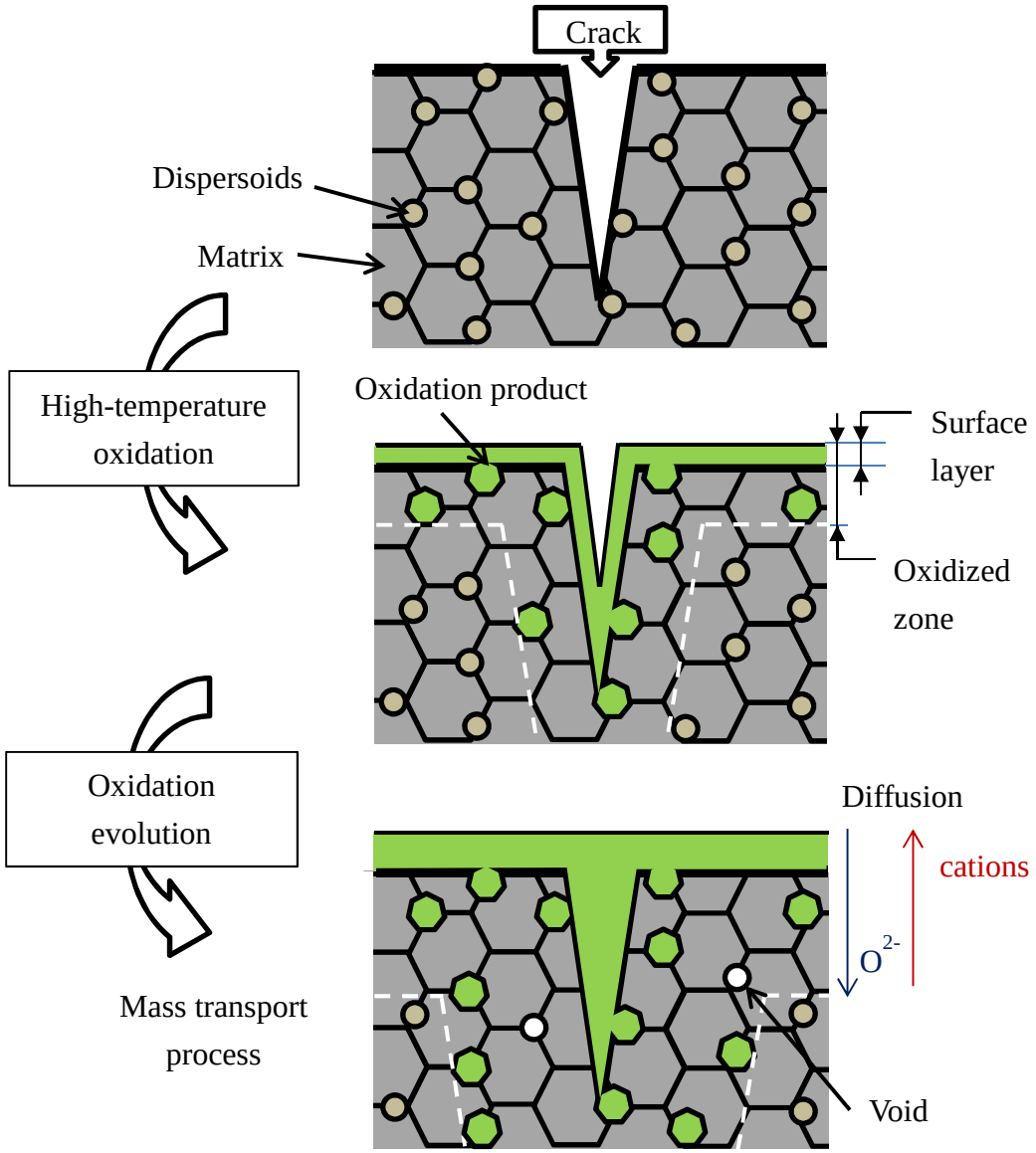

Fig. 2.1. Schematic describes the self-healing and oxidation mechanism of metal/ceramic composites at high temperatures.

From a kinetic point of view, Mo/Al_2O_3 would be a great self-healing composite. Unfortunately, the oxidation product of this system, $Al_2(MoO_4)_3$ is unstable at high-temperatures. It decomposes to form MoO_3 which is evaporated easily at high

temperatures. As a consequence, the self-healing function of Mo/Al_2O_3 exhibits poor effectiveness on strength recovery. Self-healing of Ni/Al_2O_3 composites is quite similar with that of Co/Al_2O_3 composites. The surface cracks completely disappeared by the formations of surface layers which were composed by oxidation products, $NiAl_2O_4$ or $CoAl_2O_4$. Both Ni and Co are famous with magnetic properties [72]. However, fabrication of Ni/Al_2O_3 is easier and cheaper than that of Co/Al_2O_3. Consequently, self-healing in Ni/Al_2O_3 composites draws more attention than the others. In other words, metallic Ni is considered to be a potential dispersoid for self-healing function of ceramic-based composites.

2.3 Self-healing Ni/Al_2O_3 nanocomposites as potential candidates.

Self-healing of Ni/Al_2O_3 was firstly reported by *Nanko* et al. in 2009 [65]. The surface cracks with approximately 180 μm in length completely disappeared by heat-treatment at 1200ºC for 6 h in the air. The self-healing mechanism was clarified to be the oxidation of Ni phase within Al_2O_3 matrix induced self-healing. As described in the previous section, self-healing effectiveness of Ni/Al_2O_3 depends on the formation of $NiAl_2O_4$ surface layer resulting from the outward diffusion of Ni^{2+} along Al_2O_3 grain boundaries. In the meantime, the inward diffusion of O^{2-} creates the internal oxidized zone. The outward diffusion of Ni^{2+} and inward diffusion of O^{2-} were thought to have a strong relationship. Reduction of inward diffusion O^{2-} might motivate the outward diffusion of Ni^{2+}. *Maruoka* et al. reported Si-doping decreased the growth rate of oxidized zone of Ni/Al_2O_3 composites effectively at 1200ºC [73]. Following the study, investigations of self-healing for Al_2O_3 matrix composites dispersed with Ni and SiC [74]; Ni and Si or Ni and Y [75] were conducted. Doping of SiC, Si or Y contributes to improve effectively the oxidation resistance of the composites. However, they show less influence on self-healing performance. Besides, some of the dopants give bad influence on mechanical strength of the composites. Lately in 2012, *Maruoka* et al. studied the strength recovery of Ni/Al_2O_3 as a function of surface crack-disappearance by heat-treatments in the air [76]. The study concluded that full strength recovery of

Ni/Al_2O_3 can be achieved even with 50% of surface crack disappearance. However, the strength recovery of the composites was examined by bending tests at room temperature. The effectiveness of self-healing on strength recovery at high temperatures still stays unclear. It is necessary to conduct high-temperature bending tests to clarify this fact. Also from the study, the formation of $NiAl_2O_4$ surface layer at early stage of oxidation process was described and shown in Fig. 2.2. The $NiAl_2O_4$ rigs form on the surface of Al_2O_3 matrix by the diffusions at grain boundaries. It suggests that the grain boundary diffusion is an important factor determining the oxidation kinetic of the composites. In other words, size of Al_2O_3 grains may influence on their self-healing effectiveness, oxidation resistance, as well as mechanical properties. Therefore, fabrication of Ni/Al_2O_3 nanocomposites by ultrafine grain of Al_2O_3 is proposed for the investigation of self-healing function.

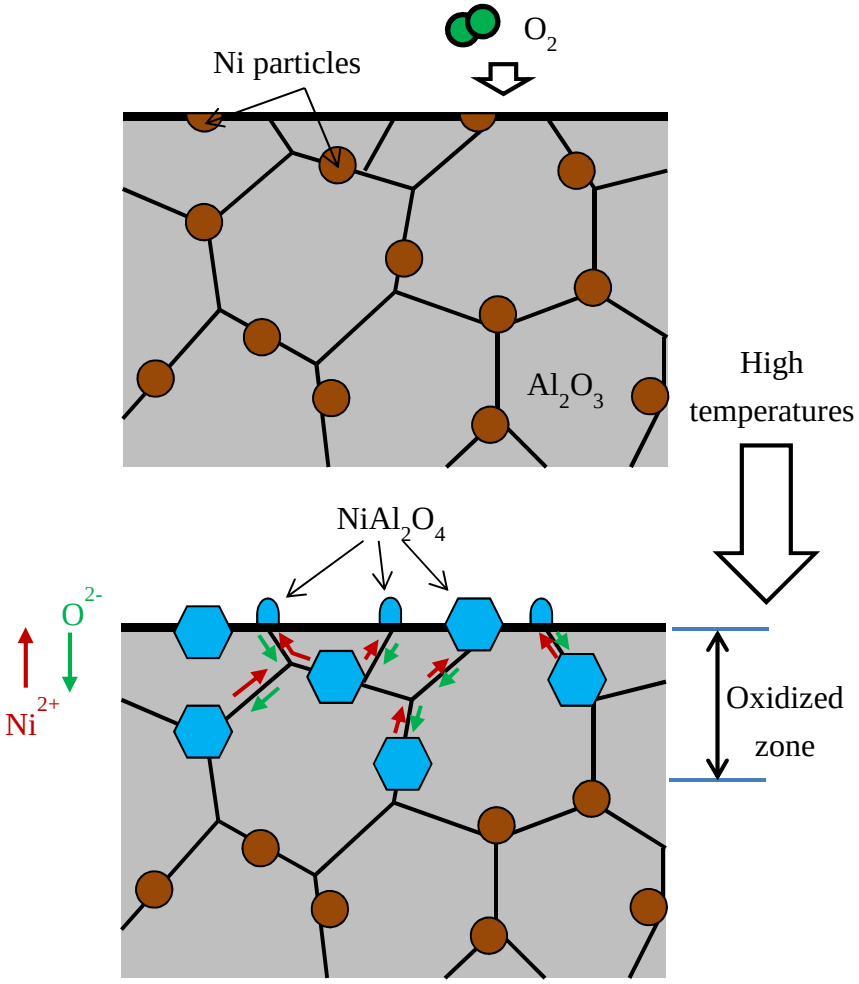

Fig. 2.2 Speculative illustrations for oxidation kinetics of Ni/Al_2O_3 composites.

2.4 Scope of the present dissertation

The overall aim of the present dissertation is to develop the self-healing function for Ni particles dispersed oxide ceramic-based composites which are Ni/Al_2O_3, Ni/(ZrO_2+Al_2O_3) and Ni/mullite nanocomposites. Ni/Al_2O_3 nanocomposites are fabricated by using ultrafine grained Al_2O_3. Self-healing function of Ni/Al_2O_3 is estimated through the surface crack-disappearance, self-healing induced-strength recovery at high temperatures and oxidation resistance. The surface crack-disappearance is evaluated by the fraction of surface crack length before/after heat-treatments in the air. The effectiveness of self-healing function on strength recovery at high temperatures is studied by high-temperature bending tests. Oxidation resistance of Ni/Al_2O_3 nanocomposites is investigated through the growth of oxidized zone by heat-treatments in the air. The influence of Al_2O_3 grain sizes on their oxidation resistance and self-healing function is discussed. Investigation of self-healing function for Ni/(ZrO_2+Al_2O_3) nanocomposites is followed the same procedures of Ni/Al_2O_3 nanocomposites. The influence of ZrO_2 on their self-healing function is then discussed. Investigation of self-healing function for Ni/mullite is conducted as an alternative choice. Mullite matrix is known as a greater material than Al_2O_3 in terms of creep property and oxidation resistance. However, mullite exhibits poor mechanical properties which may restrict their applications.

The major topics are presented and discussed as following:

1. Self-healing function of Al_2O_3-based nanocomposites dispersed Ni nano-particles (in chapter 3).
2. Influence of Al_2O_3 grain size on self-healing and oxidation resistance of Ni/Al_2O_3 composites (in chapter 3).
3. Self-healing function of Al_2O_3-based nanocomposites co-dispersed Ni and ZrO_2 nano-particles (in chapter 4).
4. Influence of ZrO_2 dispersion on self-healing, oxidation resistance and high-temperature bending strength of the composites (in chapter 4).
5. Self-healing function of mullite-based composites dispersed nano-Ni particles (in chapter 5).

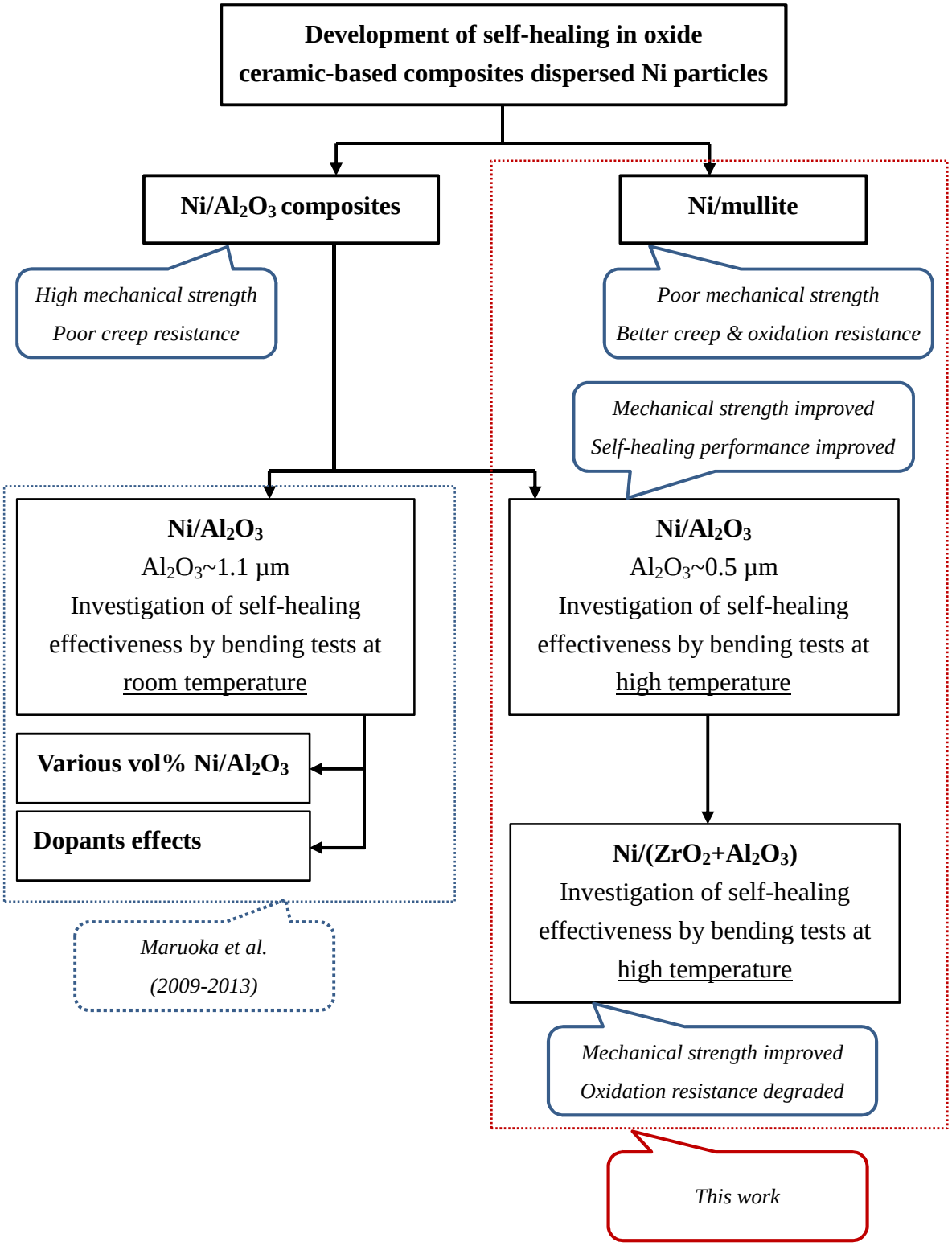

Fig. 2.3 Flow-chart explains the scope and strategy of studies discussed in the present dissertation.

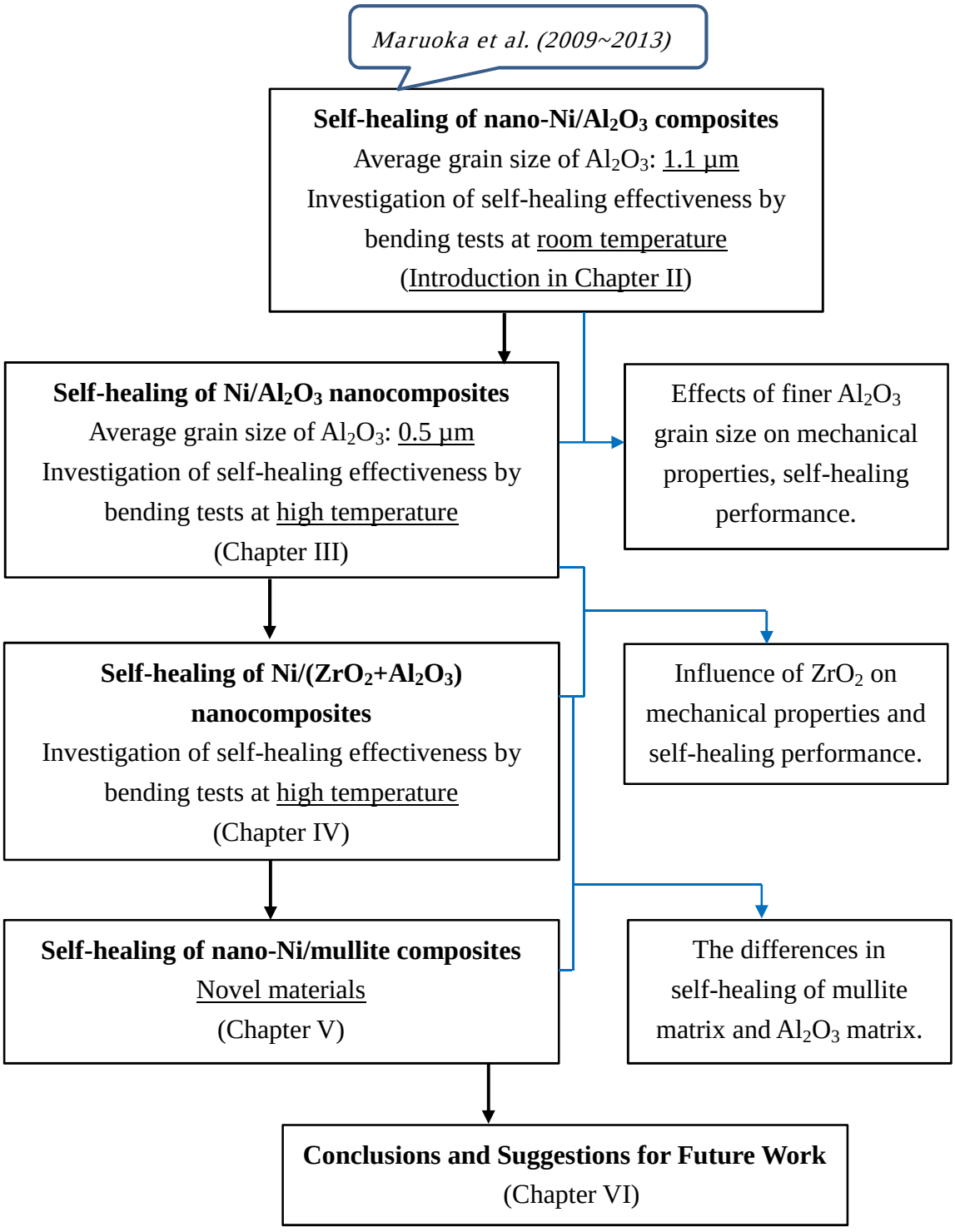

Fig. 2.4 Flow-chart shows the structure of the present dissertation.

Chapter III
Self-healing Function and High-temperature Strength of Ni/Al_2O_3 Nanocomposites with Ultrafine Al_2O_3

3.1 Background.

Grain size of Al_2O_3 matrix is an important factor controlling many properties of Ni/Al_2O_3 composites, as mentioned in the previous section. In this chapter, Ni/Al_2O_3 nanocomposites were fabricated by using ultrafine grained Al_2O_3 produced by pulsed electric current sintering (PECS) technique. The influences of Al_2O_3 grain size on their mechanical properties, surface crack-disappearance and oxidation resistance are investigated and discussed. Since the self-healing function of Ni/Al_2O_3 nanocomposites are expected to be a great solution for high-temperature applications, the healing toughness at high temperatures must be examined. Hence, high-temperature bending tests for Ni/Al_2O_3 nanocomposites are carried out in order to study their strength recovery at high temperatures.

3.2 Experimental procedure

Specimen preparation of 5 vol% Ni/Al_2O_3 nanocomposites was conducted in the following procedure. A slurry mixture containing $Ni(NO_3)_2.6H_2O$ (Kojundo Chemical Laboratory Co. Ltd), α-Al_2O_3 (Taimei Chemicals Co. Ltd, TM-DAR, d = 0.14 μm) and distilled water was prepared by ball-milling for 24 h in a plastic bottle with alumina balls (5 mm in diameter). This slurry mixture was dropped into a boiling flask that was pre-heated at 400ºC to dry up water and decompose nickel nitrate rapidly. The dried powder mixture then was dried ball-milled for 3 h in a plastic bottle by using Al_2O_3 balls with 5 mm in diameter. The powder mixture was then reduced in a stream of the Ar-1%H_2 gas mixture at 600ºC for 12 h to obtain fine nickel particles dispersed in the Al_2O_3 matrix. After the reduction process, the powder mixture was ball-milled in a plastic bottle with ethanol and alumina balls with 5 mm in diameter for 24 h to reduce the

agglomeration of the powder mixture. Drying at 80ºC for 12 h and manual crashing by a mortar were then carried out. The powder mixture was consolidated with a graphite die by PECS at die temperature of 1200ºC for 5 min holding time under 50 MPa in uniaxial pressure in a vacuum. The relative density (R.D.) of all fabricated specimens attained at least 99% of the theoretical density. Fig. 3.1 shows a scanning electron microscope (SEM) image of the fractured surface of an as-sintered specimen. Nickel particles, which could be observed as bright contrast dots, were homogeneously dispersed in the matrix. The average particle size of Ni particles was approximately 200 nm while that of Al_2O_3 was approximately 500 nm.

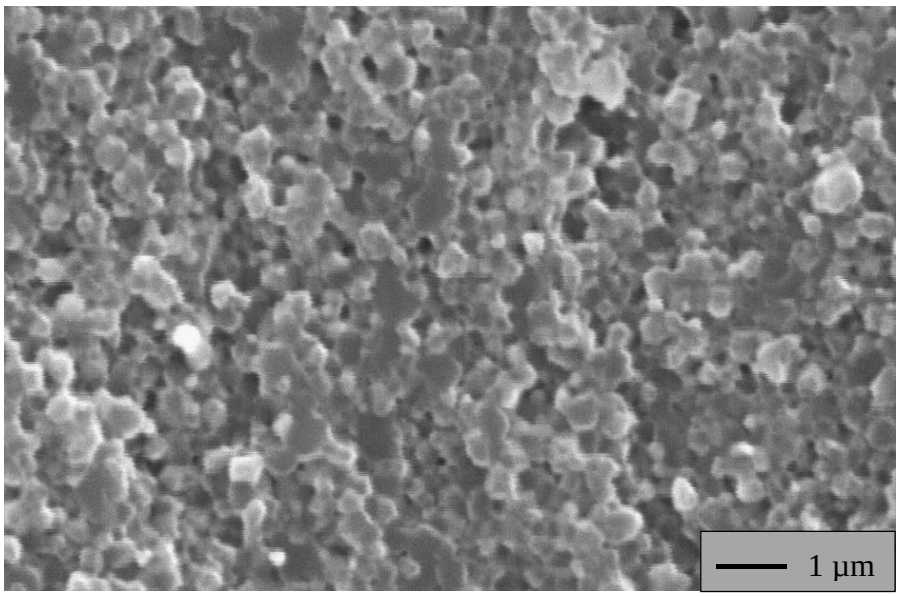

Fig. 3.1. SEM image of the fractured surface of an as-sintered specimen.

Mechanical properties of the nanocomposites such as relative density, Vickers hardness (H_v), fracture toughness (K_{IC}) and bending strength (σ_b) were evaluated at room temperature. Vickers hardness and fracture toughness were conducted, following JIS R 1610 standard and Indentation fracture method [77], respectively.

In order to investigate the surface crack-disappearance by heat-treatments, three cracks were induced on polished surface for each sample by Vickers indentation at a loading of 49 N for 10 s. Average length and depth of cracks induced on sample surface were 180 μm and 90 μm, respectively (Fig. 3.2). Each Vickers indentation produces four cracks on

specimen surface as shown in Figure 3.2a. The crack size was approximately 180 μm in length. Figure 3.2b shows the cross-sectional view of a Vickers indentation observed on the fractured surface. The dashed line indicates the front of the semi-elliptical crack introduced by the Vickers indentation. The crack depth was approximately 90 μm. Effectiveness of surface crack-disappearance after heat treatment at temperatures ranging from 1100 to 1300ºC for 1~24 h was estimated by scanning electron microscope (SEM) and X-ray diffraction (XRD) for phase identification. The details of evaluation method for surface crack-disappearance were described by *Maruoka* et al. [74, 76].

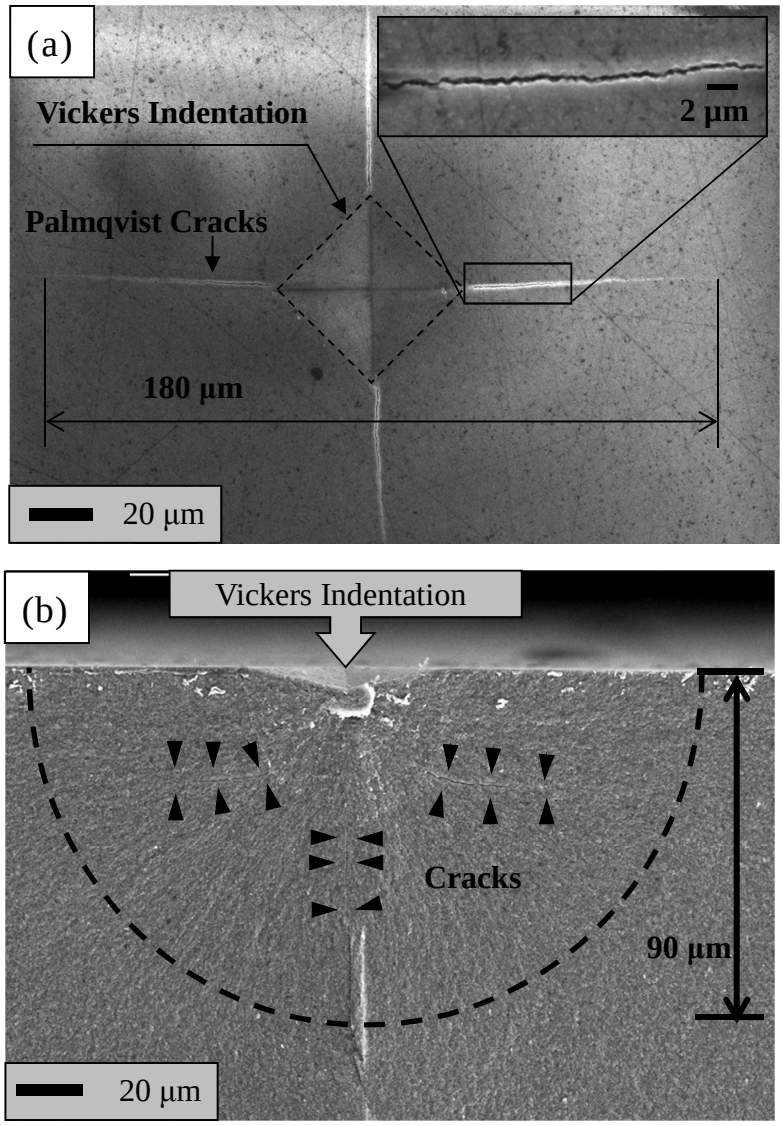

Fig. 3.2. SEM images of Vickers indentation from (a) the top view and (b) cross-sectional view of as-cracked specimen.

Investigation of strength recovery by surface crack-disappearance was conducted through high temperature bending tests. Sintered specimens were cut into a rectangular shape (3×4×26 mm) for conducting three-point-bending tests with 16 mm in the span distance. Specimen surface was ground by using a grinding wheel consisting of diamond grains with 30 μm in grain size and then polished with 2 μm-diamond particle slurry. The polished specimens are referred to as-sintered specimens, hereafter. Three Vickers indentations were introduced at the center of the specimen tension surface by applying a loading of 49 N for 10 s. The specimens with introduced Vickers indentations are referred to as-cracked specimens, hereafter. Fig. 3.3 illustrates the geometry of surface cracks introduced on the specimen surface by Vickers indentations and placement of specimen during three-point bending test. As the surface cracks can be completely healed by heat-treatment in the air at 1200ºC for 6 h [65, 76], as-healed specimens were prepared by heat-treatment of as-cracked specimens at this condition. The heat-treatment temperature was monitored by using an R-type thermocouple located near the specimens. Three-point bending tests were conducted in the air with a cross-head speed of 0.5 mm/min at room temperature and temperatures ranging from 800 to 1200ºC for as-sintered, as-cracked and as-healed specimens. Three specimens were carried out at every testing condition to obtain the mean value of bending strength as the function of testing temperatures. The testing schedule of high-temperature bending tests was described as shown in Fig. 3.4.

For investigation of oxidation resistance of the nanocomposites, oxidation tests were conducted at temperatures ranging from 1100 to 1350ºC for 1 up to 48 h in the air with a heating rate 400ºC/h. The tested samples were put on alumina balls (3 mm in diameter) in an alumina crucible and exposed in the air at the investigated conditions. Oxidized samples were then cross-sectioned and polished with 2 μm-diamond particle slurry. Phase identification of the samples was carried out by XRD. Oxidation evolution of heat-treated samples was evaluated via the growth rate of oxidized zone observed on cross-sectioned surface by SEM.

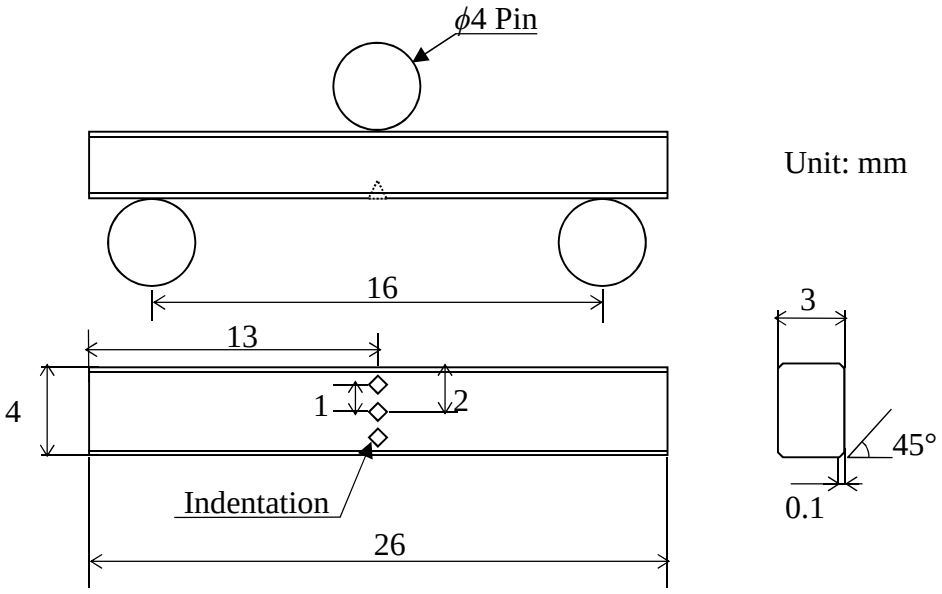

Fig. 3.3. Geometry of cracks introduced on sample surface by Vickers indentations and loading system during three-point bending test.

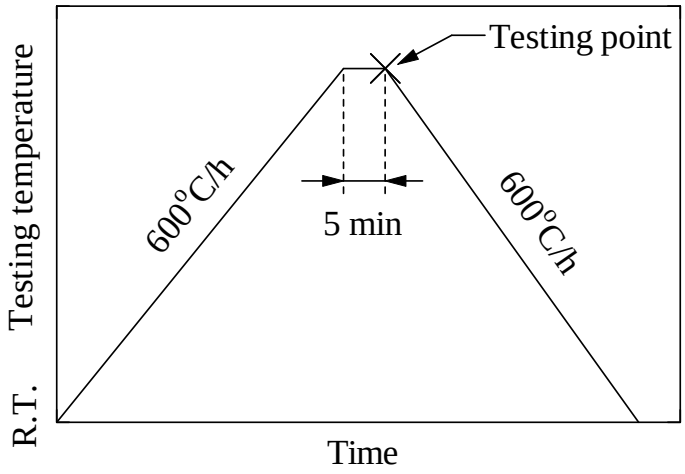

Fig. 3.4. Schematic illustration of testing schedule for high-temperature bending strength.

3.3 Results and discussion

3.3.1 Mechanical properties

Table 1 shows mechanical properties of Ni/Al_2O_3 nanocomposites in comparison with the other reported results [21, 76, 78-81]. Depending on the starting materials and fabrication method, some materials achieved very fine Ni and Al_2O_3 grain size but had not completely densified yet [21, 78]. On the other hand, some materials had improvement in density. However grain growth occurred rapidly [76, 79, 80]. By applying a proper fabrication and using very fine Al_2O_3 powder, the 5 vol% Ni/Al_2O_3 of this study was almost fully densified and resulting to very fine grain size after sintering. The nanocomposites achieved outstanding fracture toughness of 6.1±0.5 $MPam^{1/2}$ and maintained very high level of bending strength, 995±90 MPa.

Table 3.1. Mechanical properties of Ni/Al_2O_3 composites fabricated by various methods

Sample	Fabrication method	R.D. [%]	$d_{Al_2O_3}$ μm	d_{Ni} μm	K_{IC}/ $MPam^{1/2}$	σ_b/ MPa	$H_{v/}$ GPa
5%Ni/Al_2O_3 [This study]	PECS	>99	0.5	0.1	6.1	995	20
5%Ni/Al_2O_3 [76]	PECS	>99	1.1	0.3	5.8	490	20
5%Ni/Al_2O_3 [78]	Pressureless	>96	0.5	0.15	4.2	526	-
5%Ni/Al_2O_3 [21]	Hot press	>98	0.64	0.1	3.5	1090	-
5.5%Ni/Al_2O_3 [79]	Hot press	>98	1.2	0.6	4.1	500	-
5%Ni/Al_2O_3 [80]	PECS	>98	1.4	0.3	3.2	650	16
α-Al_2O_3 [81]	Pressureless	>98	5	-	3.5	380	15

3.3.2 Surface crack-disappearance

Figure 3.5 shows SEM images of sample surfaces with introduced cracks before and after heat-treatment at various conditions. Dashed lines present the outline of Vickers indentation. Without heat-treatment, cracks that are indicated by white arrows could be observed clearly as shown in Fig. 3.5a. Length and width of these cracks were

approximately 60 and 0.5 μm, respectively (Fig. 3.5b). At 1100°C, surface cracks completely disappeared after heat-treatment for 24 h (Fig. 3.5c and d). With shorter annealing time, cracks only partly disappeared at this condition. Heat-treatment at 1200°C for 1 h, 80±14% of cracks disappeared on sample surface, as shown in Fig. 3.5e and Fig. 3.5f. Increasing annealing time, cracks on sample surface completely disappeared as shown in Fig. 3.5g and Fig. 3.5h. According to *Maruoka* et al. [76], effectiveness of self-healing was depended on formation of $NiAl_2O_4$ which is referred to diffusion of Ni^{2+} along grain boundaries. Finer grain size of Al_2O_3 leads to accelerate self-healing performance. Besides, finer microstructure involves in formation of oxidation product more homogeneously on sample surface.

Figure 3.6 shows XRD patterns of sintered samples before and after heat-treatment in air in order to identify compounds formed on sample surface. Before heat-treatment, there were only two dominant substances that were α-Al_2O_3 and Ni detected on sample surface (Fig. 3.6d). After heat-treatment at 1100ºC for 24 h in air, appearance of $NiAl_2O_4$ significantly rose and replaced for the existence of Ni-metallic particle, as shown in Fig. 3.6c. Fig. 3.6b shows the intensity of $NiAl_2O_4$, which formed after heat-treatment at 1200ºC for 1 h, was almost similar to the term of sample after heat-treated at 1100ºC for 24 h. At 1200ºC for 6 h (Fig. 3.6b), there were some weak intensity peaks of Ni metallic particles detected. Instead of that, $NiAl_2O_4$ that was attributed to being a key factor responsible for crack-healing rapidly formed and covered sample surface. According to the ternary phase diagram of the Ni-Al-O system [82], $NiAl_2O_4$ is the only oxidation product. NiO does not coexist with Al_2O_3. It has been discussed elsewhere [64, 73, 74].

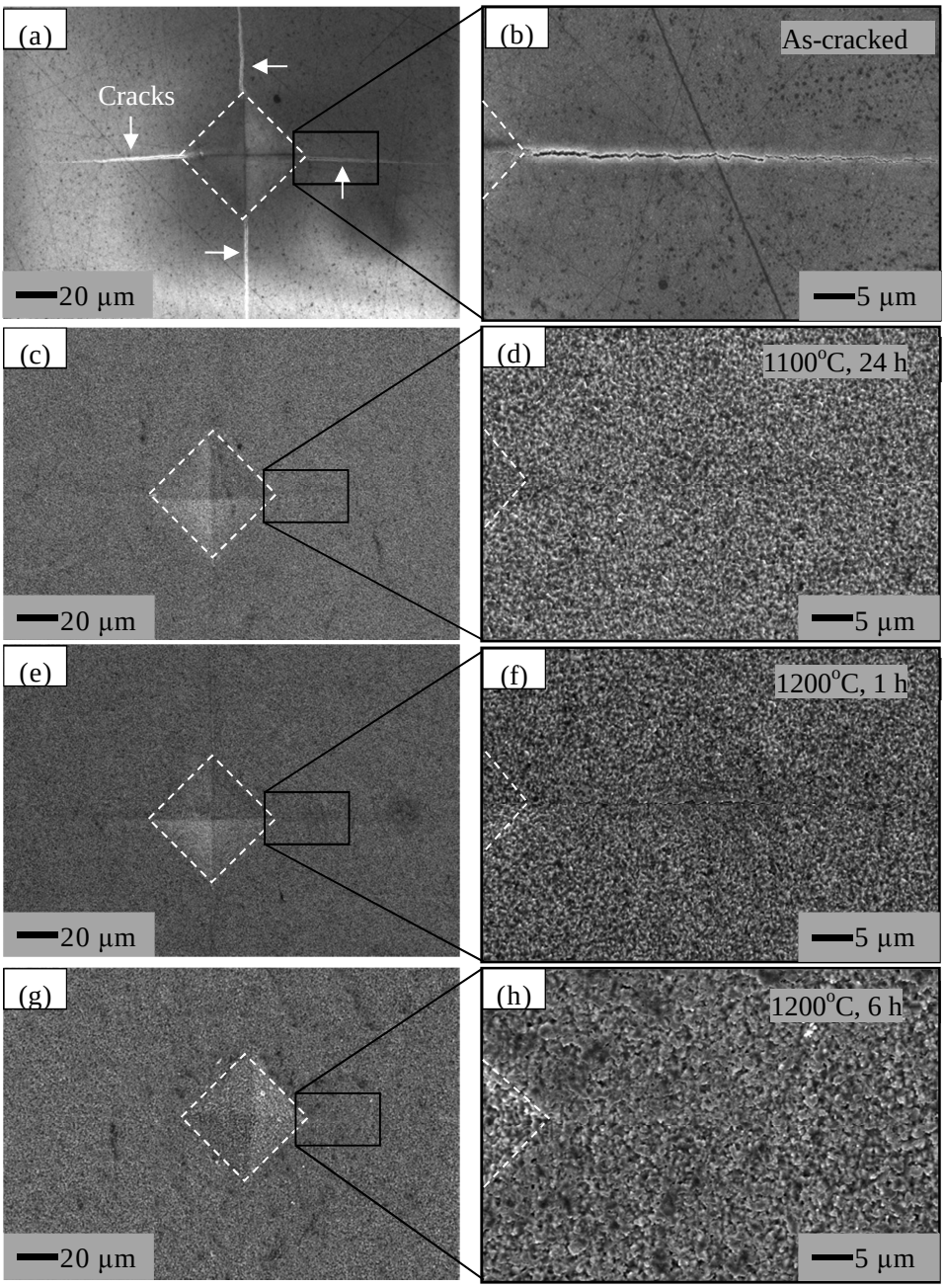

Fig. 3.5 SEM images of surfaces of as-cracked sample (a) and (b), sample heat-treated at 1100°C for 24 h in air (c) and (d), sample heat-treated at 1200°C for 1 h in air (e) and (f), sample heat-treated at 1200°C for 6 h in air (g) and (h).

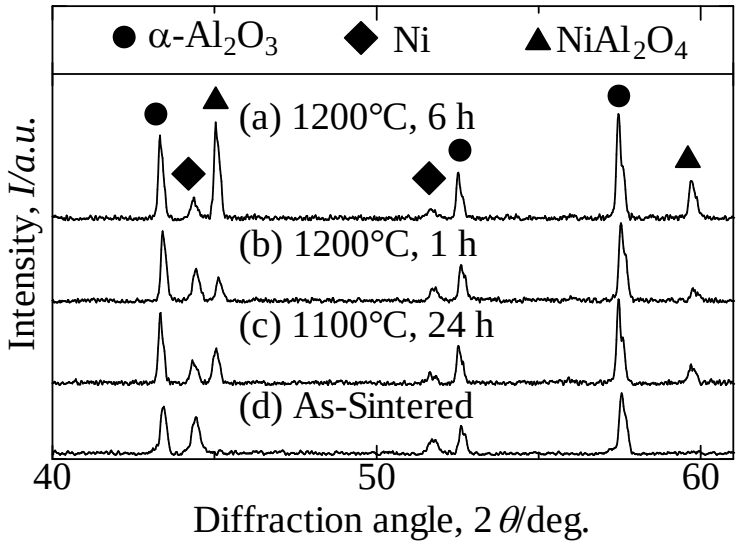

Fig. 3.6 XRD patterns of the sintered Ni/Al_2O_3 samples with/without heat-treatments in air.

3.3.3 Self-healing-induced strength recovery

Figure 3.7 shows the results of high-temperature bending tests of as-sintered, as-cracked and as-healed specimens. At room temperature, bending strength of as-sintered specimens was determined as 995±85 MPa. Bending strength of as-cracked specimens (three Vickers indentations introduced on each specimen) only achieved 120±5 MPa. By heat-treatment at 1200ºC for 6 h in the air, cracks on as-healed specimens were completely healed as shown in Figure 3.5g. As a result, as-healed specimens achieved 890±15 MPa in bending strength, which is as same as that of as-sintered specimens. At 800ºC, bending strength of as-sintered and as-healed specimens decreased to the values of 545±140 MPa and 505±35 MPa, respectively. While, that of as-cracked specimens slightly increased to 165±35 MPa. Bending strength of as-sintered, as-healed and as-cracked specimens at 1000ºC was 405±75, 480±70 and 190±10 MPa, correspondingly. When the temperature reached to 1200ºC, the value of as-healed specimens was 200±10 MPa, while that of as-cracked specimens obtained 130±10 MPa. At this critical temperature, the plastic deformation of as-sintered specimens occurred at a loading of 205 MPa. Two specimens out of three tested ones did not fracture during the high-temperature bending tests, as shown in Fig. 3.8. Fig. 3.9 shows the applied force as

a function of displacement during high temperature bending tests of Ni/Al_2O_3 specimens. Ni/Al_2O_3 specimens exhibited both elastic and plastic deformations at 1200ºC as seen in Fig 3.9 a. The applied force suddenly increased from 300 N to 1300 N when the specimen reached and contacted the lower jig due to the bending of the specimen. The Ni/Al_2O_3 specimens did not show any plastic deformation at 1100ºC, as shown in Fig. 3.9b.

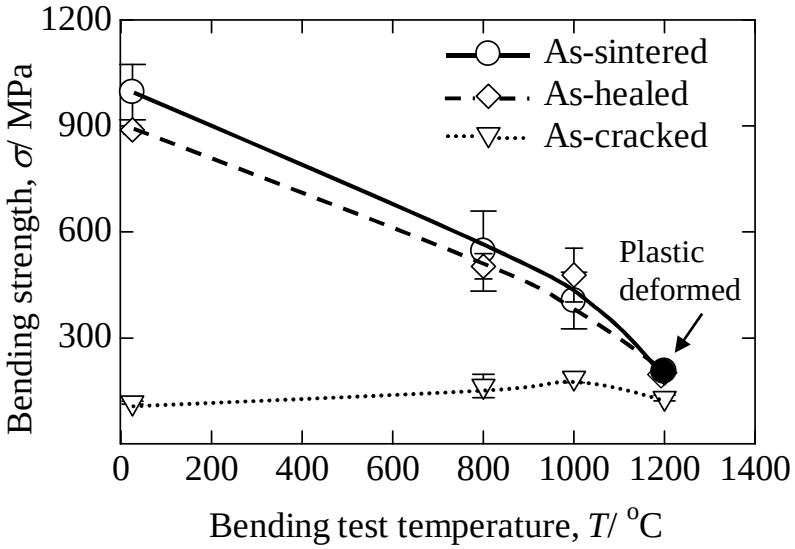

Fig. 3.7 Bending strength of as-sintered, as-cracked and heat-treated specimens as a function of bending test temperatures.

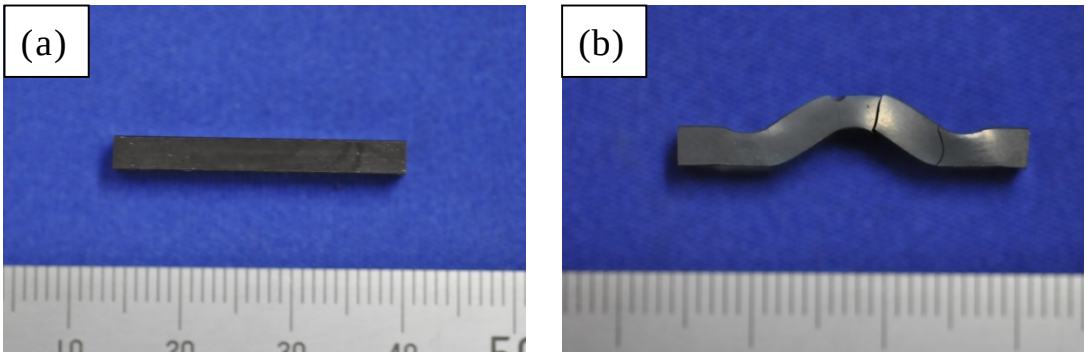

Fig. 3.8. Photographs show the morphology of the as-sintered specimen (a) before and (b) after high-temperature bending test conducted at 1200ºC.

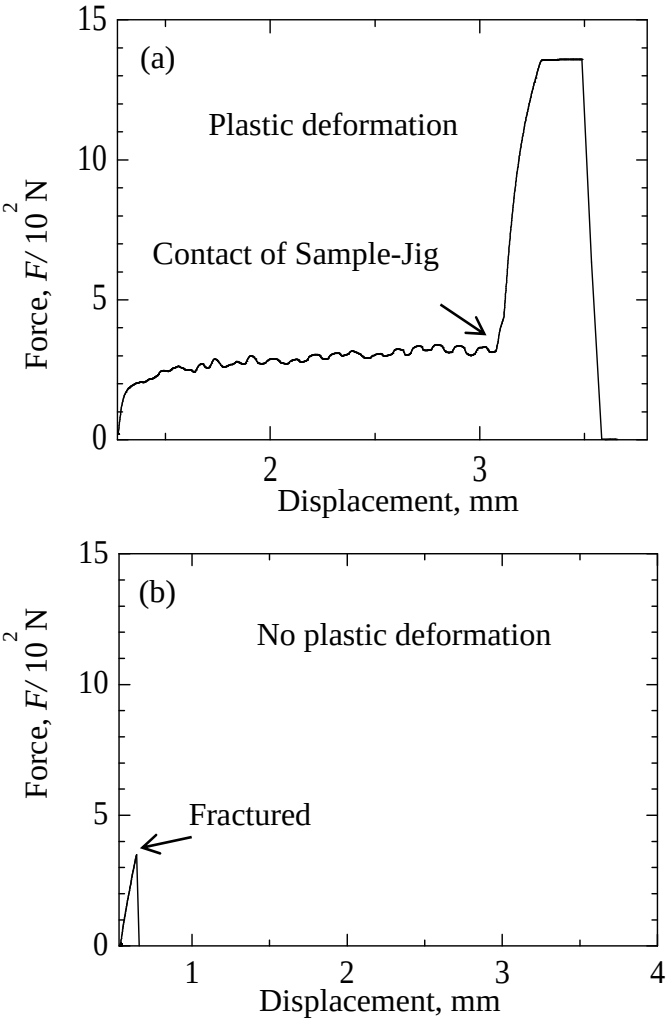

Fig. 3.9. Applied force as a function of displacement during high temperature bending tests for Ni/Al_2O_3 nanocomposites at (a) 1200 and (b) 1100ºC.

Bending strength of as-sintered specimens was tested at room and temperatures ranging from 800 to 1200ºC to evaluate the performance of the nanocomposite at high temperatures. At room temperature, the as-sintered specimens exhibited great bending strength due to the ultrafine microstructure as shown in Fig. 3.1. Nonetheless, the bending strength of as-sintered specimens dramatically decreased as increase of testing temperature. Evans *et al.* reported that high-temperature mechanical strength of general polycrystalline ceramics depend on slow crack growth caused by cavitations and/or grain boundary sliding [83]. Niihara *et al.* reported the mechanical degradation at high temperatures of 5 vol% SiC/Al_2O_3 was worse than that of monolithic Al_2O_3 ceramic due to a mismatch stress [25]. The mismatch stress of the nanocomposite at high temperatures

was caused by the difference in coefficients of thermal expansion (CTE) of the dispersiod and the matrix that propagated slow crack growth at cavities. The similar behaviors have been reported in Al_2O_3 based nanocomposites by Niihara *et al*. [26, 84]. Figure 3.10 shows the temperature dependence of the bending strength for Ni/Al_2O_3, SiC/Al_2O_3 [26], W/Al_2O_3 [84] and monolithic Al_2O_3 [26]. Among these nanocomposites, SiC/Al_2O_3 has the highest bending strength at high temperatures. This manner could be explained by the smaller difference in CTE of SiC/Al_2O_3 than the other composites. On the other hand, the interface energy between the Ni particles and Al_2O_3 grains could be one of the factors that affect the mechanical behavior of the composites at high temperatures, as demonstrated in Fig. 3.11. Tuan *et al.* reported the interfacial fracture energy for Ni/Al_2O_3 system is lower than the transgranular fracture energy [85]. It means that the fracture mode in Ni/Al_2O_3 system is intergranular one. Whereas, the interfacial fracture energy for SiC/Al_2O_3 system is higher than the transgranular fracture energy [86]. This implies that the fracture mode in SiC/Al_2O_3 system is the transgranular fracture. In other words, the dispersion of Ni particles has less effectiveness in inhibition of grain boundary sliding than the dispersion of SiC at high temperatures.

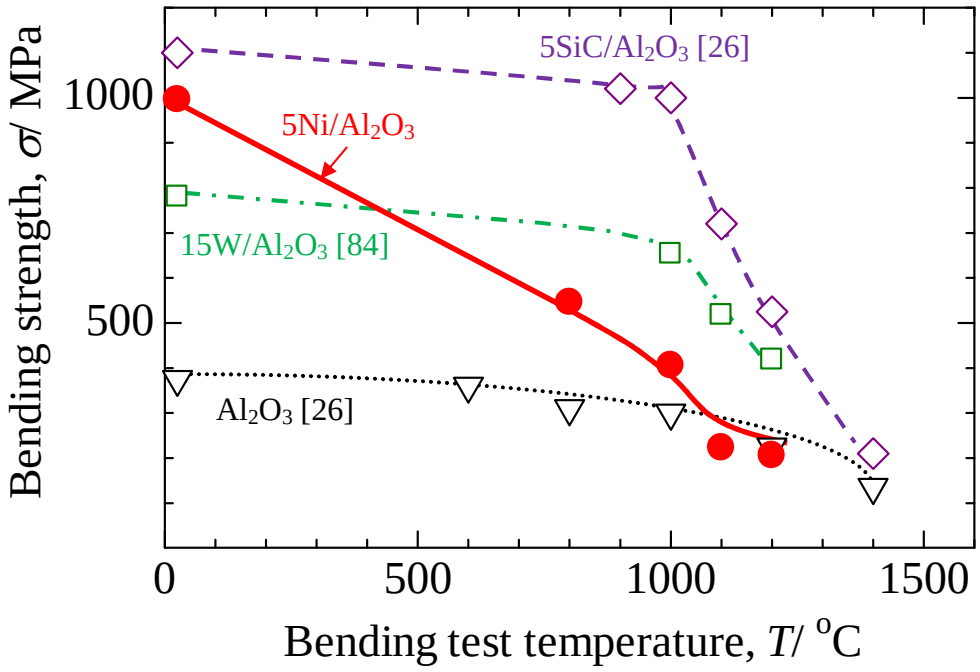

Fig. 3.10 Temperature dependence of the bending strength for 5 vol% Ni/Al_2O_3 and the other nanocomposites reported by Niihara et al..

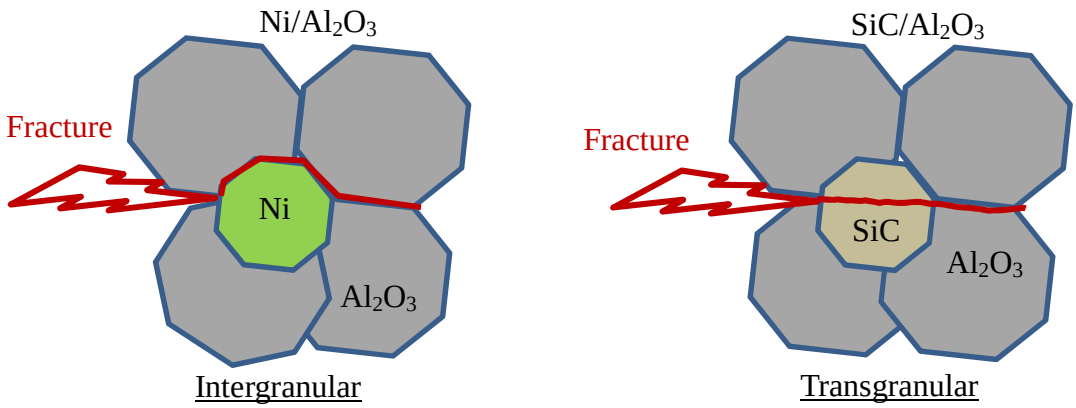

Fig. 3.11. Fracture mechanisms of Ni/Al_2O_3 and SiC/Al_2O_3 composites.

The situation became totally different when the high-temperature bending tests of as-sintered specimens were conducted at 1200ºC. As-sintered specimens were able to deform and stand against their failure at this critical temperature. As shown in Fig. 3.8b, the specimen was deformed and did not fracture during the high-temperature bending test. The cracks on the as-sintered specimen shown in Fig. 3.8b only appeared during the cooling process of the bending test. From the mechanical point of view, the Ni/Al_2O_3 nanocomposites must be operated at the temperatures below 1000ºC.

In order to evaluate the effectiveness of self-healing function at high temperatures, bending tests were conducted for as-healed specimens at room temperature, 800, 1000 and 1200ºC. Bending strength of as-healed specimens at room temperature was 890 MPa, as high as that of as-sintered specimens. As discussed by Maruoka *et al.*, the recovery of bending strength was attributed to the effect of the self-healing mechanism [64]. Fig. 3.12a shows the fractures of as-healed specimens after bending tests conducted at room temperature indicating that the fracture of specimens propagated from the outside of introduced indentations. It indicates that the Vickers indentations were no longer being the highest stress concentration points. The same phenomena were observed on as-healed specimens conducted at higher temperatures, as shown in Fig. 3.12b, c and d. The self-healing-induced mechanical recovery was not affected by the testing temperatures. Although the self-healing function is effective at high temperatures, the bending strength of as-healed specimens decreased as increase of testing temperatures. This behavior was similar to the mechanical behavior at high temperatures of as-sintered specimens. On the other hand, values of bending strength of as-healed specimens conducted at 800 and

1000ºC were comparable with that of as-sintered specimens conducted at the same temperatures. The self-healing induced strength recovery of Ni/Al_2O_3 nanocomposites is available at high temperatures.

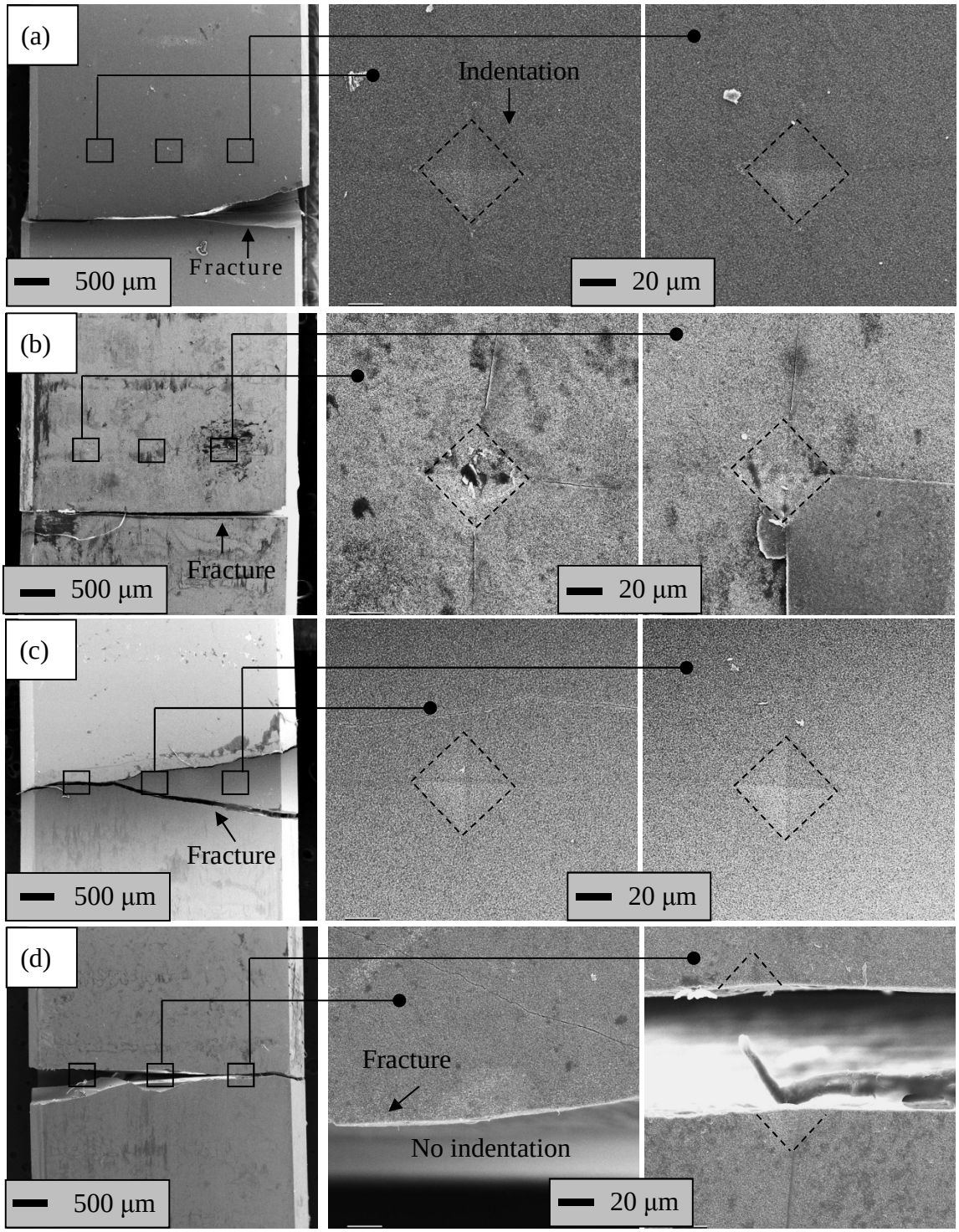

Fig. 3.12. SEM images show the fractures of as-healed specimens in bending tests conducted at (a) room temperature, (b) 800, (c) 1000 and (d) 1200ºC.

High-temperature bending tests were conducted for as-cracked specimens in order to estimate their performance at high temperatures as damaged stage and to compare with that of as-healed specimens. In general, brittle materials fracture and fail from the highest stress concentration at the largest defects. As shown in Fig. 3.13a and b, the as-cracked specimen fractured along all the introduced Vickers indentations during the bending tests conducted at room temperature and 800ºC. Above 800ºC, the bending strength of as-cracked specimens slightly increased as increase of testing temperatures. The fractures of as-cracked specimens that were conducted at 1000 and 1200ºC did not propagate across all the cracks introduced by Vickers indentations, as shown in Fig. 3.13c and d. Fig. 3.14 shows XRD patterns of exposed surface for as-cracked specimens after bending tests conducted at room temperature, 800, 1000 and 1200ºC, which mean the formation of $NiAl_2O_4$-oxidation product after high-temperature bending tests. Taking account of the testing schedule as shown in Fig. 3.4, the testing specimens were heated up to the testing temperature with a heating rate of 600ºC/h in the air. It suggests that the oxidation product was formed during the heating process of high-temperature bending tests. From the reasons above, the increase of bending strength of as-cracked specimens as increase in testing temperature was attributed to the effect of self-healing mechanism on mechanical strength. In other words, partial recovery of bending strength in Ni/Al_2O_3 nanocomposite is able to obtain rapidly when it is applied at high temperatures.

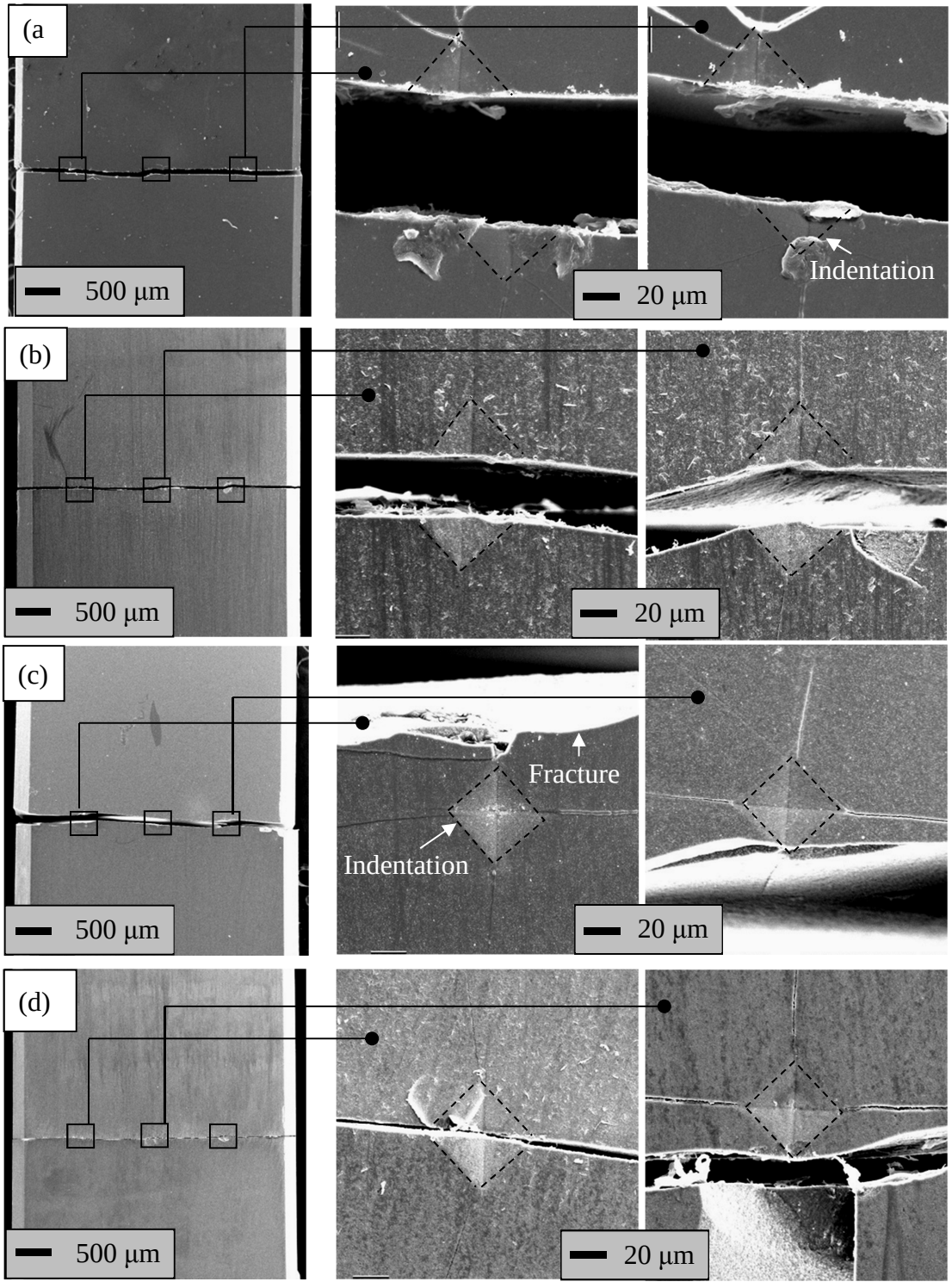

Fig. 3.13. SEM images of as-cracked specimens showing the fracture after bending tests conducted at (a) room temperature, (b) 800, (c) 1000 and (d) 1200ºC.

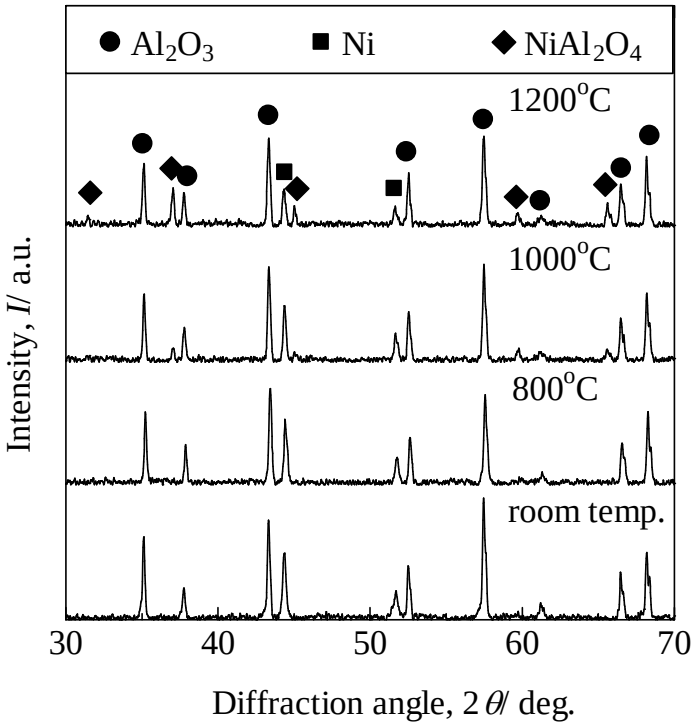

Fig. 3.14. XRD patterns of exposed surface for as-cracked specimens after bending tests conducted at room temperature, 800, 1000 and 1200ºC.

While the as-sintered specimens showed the superplasticity at 1200ºC, the as-healed specimens performed the different plasticity at the same condition. The superplasticity of as-sintered specimens was attributed to a result of the ultrafine microstructure of the composite [87-91]. Xue *et al.* reported the deformation at 1300ºC of high-purity alumina that had the average grain size of 0.5 μm [91]. Although the ultrafine-grained alumina exhibited the low initial flow stress at the deformation temperatures, grain-growth-induced strain hardening gave rise to high flow stress causing cavitation and cracking. The grain growth during deformation can be reduced by a small addition of MgO [89] or ZrO_2 [90]. Unlike the superplasticity of as-sintered specimens, the as-healed specimens fractured during the high-temperature bending tests conducted at 1200ºC. They did not show any deformation capability to stand against their failure. This behavior was caused by the formation of the internal-oxidized zone, where all of the Ni particles were oxidized. Fig. 3.15 shows the fractured surface of an as-healed specimen after high-temperature bending

test conducted at room temperature. The as-healed specimens were heat-treated at 1200ºC for 6 h in the air before the high-temperature bending tests. The heat-treatment induced the formation of oxidized zone, in which, metallic Ni particles no longer existed. According to the ternary phase diagram of the Ni-Al-O system, $NiAl_2O_4$ was the only oxidation product that has a melting temperature of 2110ºC [82]. Taking account of the cracks that were induced by Vickers indentation as shown in Fig. 3.2b, the internal region consisting of the cracks became the exposed region. Fig. 3.16 shows a Vickers indentation from the fractured surface of an as-healed specimen after high-temperature bending test conducted at 1200ºC. The depth of the oxidized zone with the introduced indentation was approximately 90 μm while that of the oxidized zone without the indentation was approximately 18 μm. The internal region consisting of the cracks became the oxidized region that resisted the deformation of the as-healed specimen. On the other hand, the result of high-temperature bending tests indicated that bending strength of as-healed specimens was similar with that of as-sintered specimens. In other words, high-temperature bending strength of Ni/Al_2O_3 nanocomposite was not affected by the oxidized zone.

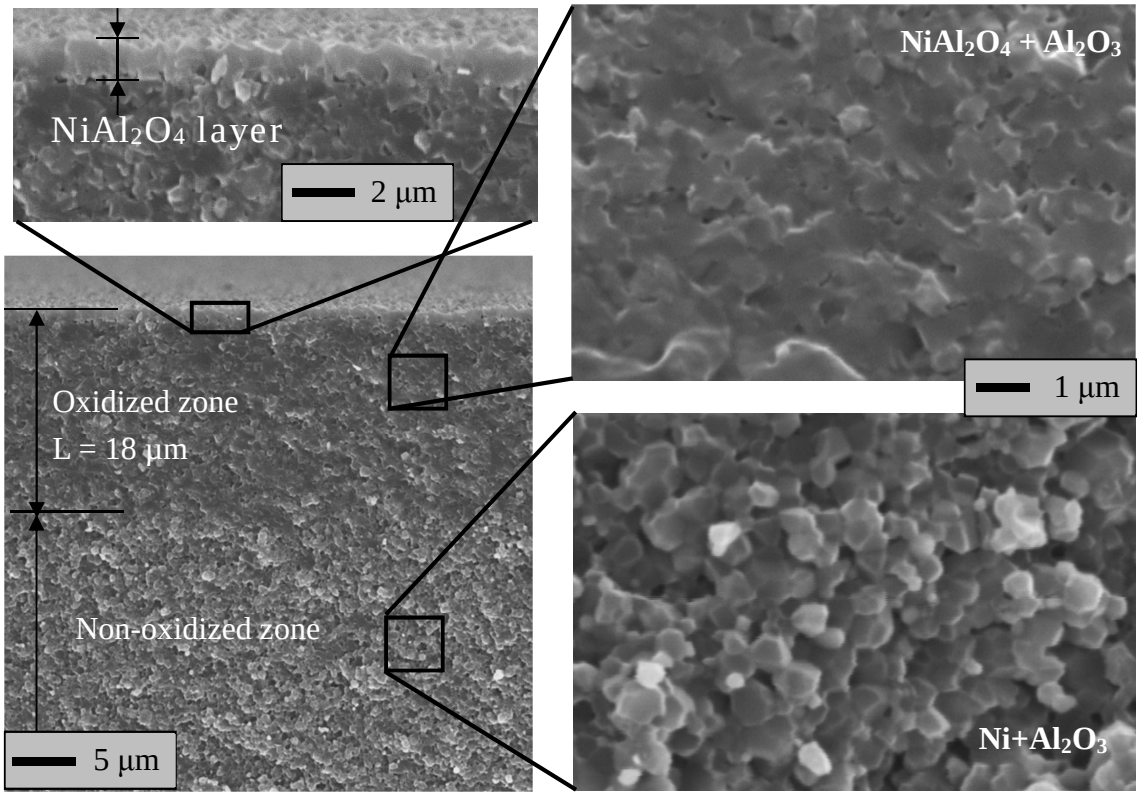

Fig. 3.15. SEM images show the fractured surface of an as-healed (1200ºC for 6 h) specimen after high-temperature bending test conducted at room temperature.

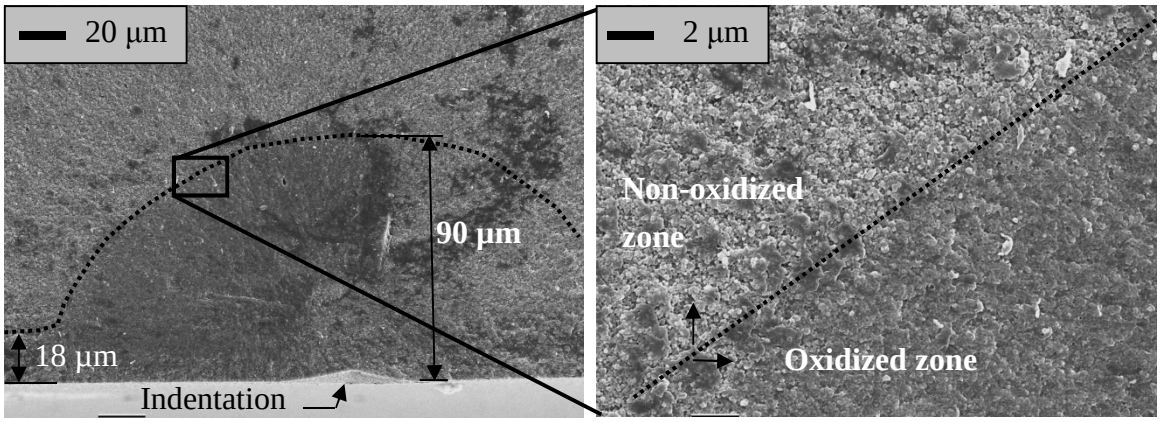

Fig. 3.16. SEM images show a Vickers indentation from the fractured surface of an as-healed specimen after high-temperature bending test conducted at 1200ºC.

3.3.4 Oxidation resistance

Figure 3.17 shows the SEM images of cross-sectioned surface of Ni/Al_2O_3 nanocomposites after oxidation at 1200ºC for 24 h and 1300ºC for 12 h. In the region from the surface to the depth of 35 μm, the grains that are larger than Ni particles were oxidation product-$NiAl_2O_4$ formed by oxidation test (Fig. 3.17a). Nano-Ni particles could be visible as the bright dots in the region deeper 35 μm from the surface. For the reasons above, the region composed of the $NiAl_2O_4$ grains and Al_2O_3 was defined as the oxidized zone. Figure 3.17b shows the thickness of oxidized zone is 65 μm after oxidation test 1300ºC for 12 h. A thin surface layer that has the same color of $NiAl_2O_4$ was observed on both samples as shown in Fig. 3.17. From XRD results, the thin surface layer formed on the sample surface was determined as the $NiAl_2O_4$ layer.

Figure 3.18 shows the thickness of oxidized zone of the nanocomposites as a function of oxidation time at various temperatures. With increasing oxidation temperature, the thickness of the oxidized zone increased. The growth of oxidized zone obeyed the parabolic law:

$$x^2 = k_p t, \tag{3.1}$$

where x is the thickness of oxidized zone; k_p the parabolic rate constant, and t oxidation time.

Figure 3.19 shows the parabolic rate constant, k_p, as a function of reciprocal oxidation temperature for the growth of oxidized zone for Ni/Al_2O_3 nanocomposites in comparison with the previous reported study on Ni/Al_2O_3 composites [92]. Slopes of both the lines were almost equal. The values of apparent activation energy for the growth rate of oxidized zone in Ni/Al_2O_3 nanocomposites and the previous reported Ni/Al_2O_3 composites were 400 $kJmol^{-1}$ and 414 $kJmol^{-1}$, respectively.

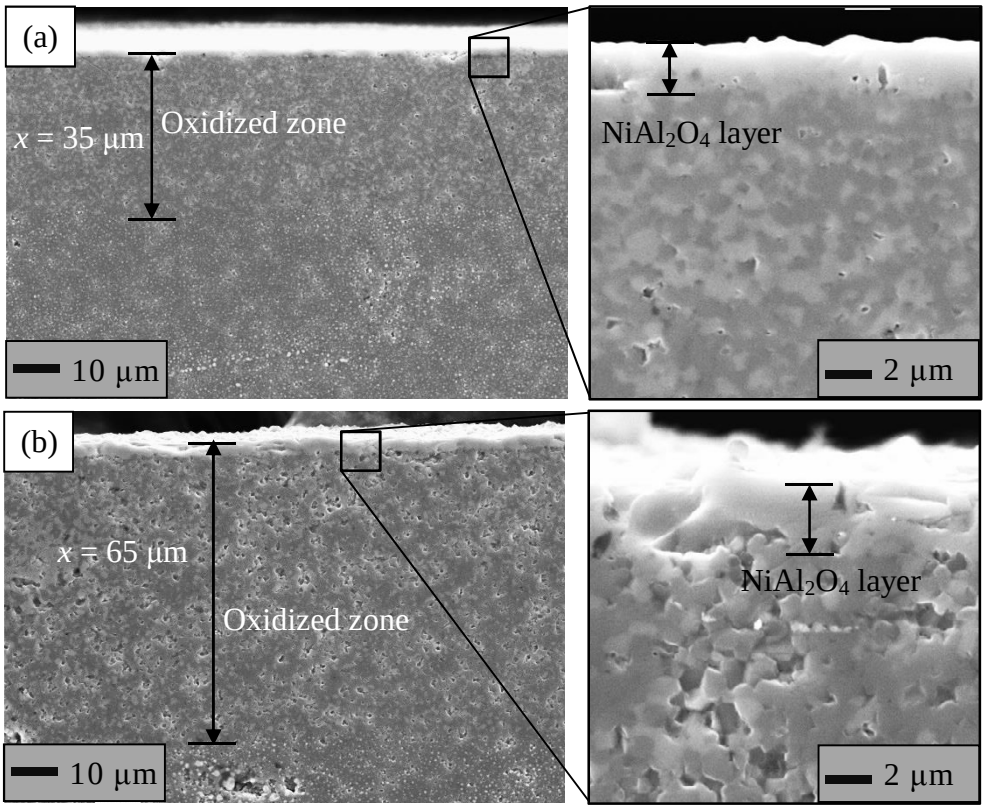

Fig. 3.17. SEM images show the cross-sectioned surface of Ni/Al_2O_3 nanocomposites after oxidation at (a)1200ºC for 24 h and (b) 1300ºC for 12 h in the air. A thin surface layer composed of $NiAl_2O_4$ was observed on both samples.

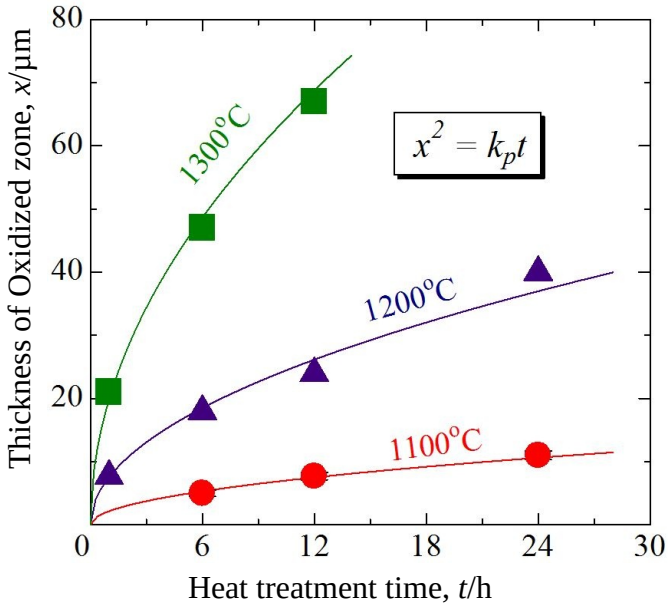

Fig. 3.18. Thickness of oxidized zone as a function of oxidation time at various temperatures for Ni/Al_2O_3 nanocomposites.

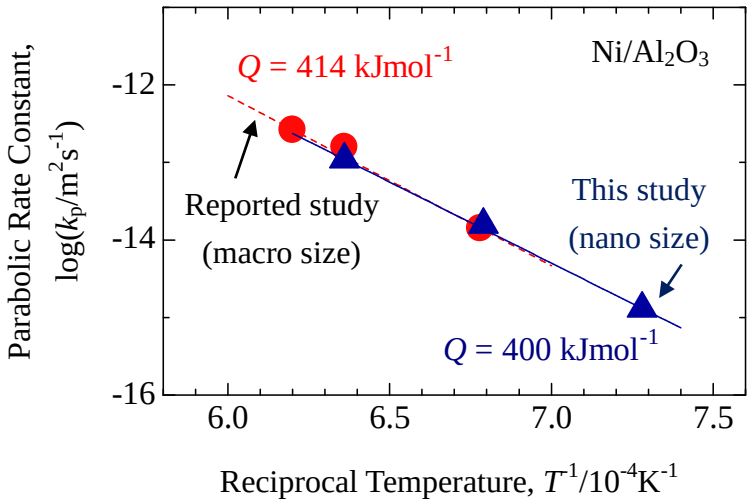

Fig. 3.19. Temperature dependence of parabolic rate constant on oxidation of Ni/Al_2O_3 nanocomposites in comparison with reported Ni/Al_2O_3 (Al_2O_3 grain size of1.1 µm) [92].

As shown in Fig. 3.17, Ni particles react with O_2 within the Al_2O_3 matrix at high temperatures to form oxidation product as the following equilibrium:

$$2Ni + 2Al_2O_3 + O_2 = 2NiAl_2O_4 \quad (3.2)$$

From the Fick's 1st law:

$$J_o = \frac{-D_o C_o}{RT}\frac{d\mu_o}{dX} \quad (3.3)$$

Where J_o is Diffusion flux of Oxygen ions; D_o Diffusion coefficient; C_o Molar concentration; R Gas constant; T Temperature; μ_o Chemical potential of oxygen; X Thickness of the internal-oxidized zone.

From the Gibbs free energy of oxygen:

$$\mu_{o_2} = \mu^0_{o_2} + RTlnP_{o_2} \quad (3.4)$$

Where $\mu^0_{o_2}$ is Chemical potential in a given standard state (constant); P_{o_2} Oxygen partial pressure.

Consider the $\mu_{o_2} = 2\ \mu_o$

$$d\mu_o = \frac{RT}{2}\mathrm{d}\ln P_{o_2} \quad (3.5)$$

From (3.3) and (3.5):

$$J_o = \frac{-D_o C_o}{2} \frac{dlnP_{o_2}}{dX} \quad (3.6)$$

Integrate equation (3.6):

$$J_o = \frac{-D_o C_o}{2X} \ln\left(\frac{P_{o_2}^2}{P_{o_2}^1}\right) \quad (3.7)$$

Where $P_{o_2}^1$ is the oxygen partial pressure at the interface between the surface layer and the internal-oxidized zone; $P_{o_2}^2$ the oxygen partial pressure at the interface between the internal-oxidized zone and the non-oxidized zone.

In consideration of volume fraction of Ni which affects the development of the internal-oxidized zone, the J_o can be expressed as the equation below:

$$J_o = \frac{f_{V_{Ni}}}{V_{Al_2O_3}} \frac{dX}{dt} \quad (3.8)$$

Where $f_{V_{Ni}}$ is Volume fraction of Ni; $V_{Al_2O_3}$ Molar volume of the matrix.

t - Oxidation time.

From equations (3.7) and (3.8):

$$\frac{f_{V_{Ni}}}{V_{Al_2O_3}} \frac{dX}{dt} = \frac{-D_o C_o}{2X} \ln\left(\frac{P_{o_2}^2}{P_{o_2}^1}\right) \quad (3.9)$$

Assuming that D_o and C_o are constant for *X* and *t*,

$$X^2 = V_{Al_2O_3} \frac{D_o C_o}{f_{V_{Ni}}} \ln\left(\frac{P_{o_2}^1}{P_{o_2}^2}\right) t \quad (3.10)$$

Since the diffusion path is attributed to the grain boundaries of the matrix, the grain size factor k_{gs} is taken into account as following:

$$D_o = D_{gb}\, k_{gs} \quad (3.11)$$

Where D_{gb} is Coefficient of grain boundary diffusion; k_{gs} Grain size factor (fraction of grain sizes). The factor implies the difference in grain size of the matrix. $k_{gs} > 1$ means the improvement in microstructure. $k_{gs} = d_1/d_2$ ($d_2 < d_1$)

From equations (3.10) and (3.11):

$$X^2 = k_{gs} V_{Al_2O_3} \frac{D_{gb} C_o}{f_{V_{Ni}}} \ln\left(\frac{P_{o_2}^1}{P_{o_2}^2}\right) t \quad (3.12)$$

From the equation 3.12, the rate constant for the development of the internal-oxidized zone is directly proportional with the grain size factor. The rate constant can be increased twice if the grain size is smaller two times of magnitude. The formation of the

internal-oxidized zone can be predictable. However, experimental results indicated the formation of oxidized zone in Ni/Al_2O_3 nanocomposites in this study was comparable with the previous reported study on Ni/Al_2O_3 composites (macro Al_2O_3 grain size) [92].

Figure 3.20 shows SEM images observed on the fractured surface of Ni/Al_2O_3 composites with macro grain size after oxidation at 1300ºC for 12 h. The average Al_2O_3 grain size in the oxidized zone was 1.5 μm (Fig. 3.20b) while it was 1.3 μm in the non-oxidized zone (Fig. 3.20c). The existence of pores in the oxidized zone was attributed to outward diffusion of cations. Similarly, Figure 3.21 shows the differences in the microstructure of Ni/Al_2O_3 nanocomposites after oxidation at 1300ºC for 12 h. The average Al_2O_3 grain size in the oxidized zone was 1.3μm (Fig. 3.21b) while it was 0.75μm in the non-oxidized zone (Fig. 3.21c). Taking account of Al_2O_3 microstructure after sintering, the average Al_2O_3 grain sizes in Ni/Al_2O_3 composites and Ni/Al_2O_3 nanocomposite were 1.1μm and 0.5 μm, respectively. Ni/Al_2O_3 nanocomposites were sintered at 1200ºC which was lower than that of the investigated conditions. Oxidation at temperatures higher than sintering temperature caused grain growth of the composites. On the other hand, Ni particles dispersed in Al_2O_3 matrix act as grain growth inhibitors. Outward diffusion of cations in oxidized zone during oxidation induced the reduction of Ni concentration. Consequently, grain growth occurred during oxidation tests especially in the oxidized zone. The similarities of Al_2O_3 grain size in oxidized zone causes the similarities of oxidation behavior. In summary, nanostructure on Ni/Al_2O_3 is effective for mechanical behavior. However, there was no significant influence in high-temperature oxidation and its related phenomena because of grain growth in their oxidation zone.

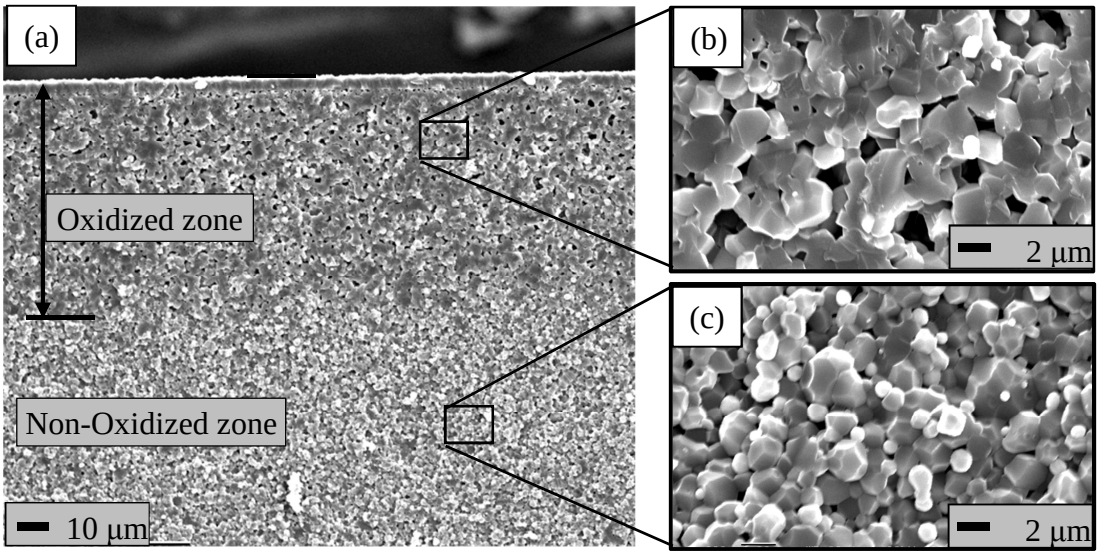

Fig. 3.20. SEM images showing fractured surface of Ni/Al_2O_3 composites with macro Al_2O_3 grain size after oxidation at 1300ºC for 12 h.

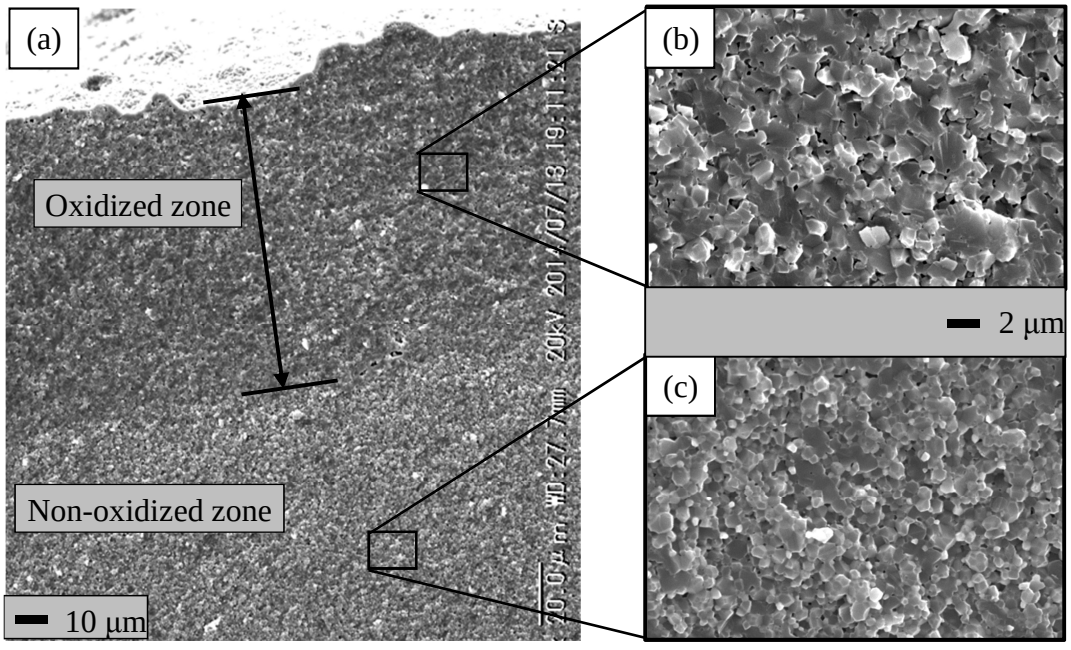

Fig. 3.21. SEM images showing fractured surface of Ni/Al_2O_3 nanocomposites after oxidation at 1300ºC for 12 h.

3.4 Conclusions.

Fully densified 5 vol% Ni/Al_2O_3 nanocomposites were fabricated by PECS to investigate their mechanical properties, surface crack-disappearance by heat-treatments in air, strength recovery at room and high temperatures; and oxidation resistance. The following conclusions are based on these properties:

1. Mechanical properties

Ni/Al_2O_3 nanocomposites fabricated by PECS with a proper powder processing achieved highly density, ultrafine microstructure with average 0.5 μm grain size of Al_2O_3 and 0.1 μm particle size of Ni. As a consequence, consolidated specimens exhibited outstanding fracture toughness of 6.1 $MPam^{1/2}$ and maintained high bending strength of 995 MPa. With the ultrafine microstructure, the nanocomposites also obtained 20 GPa in Vickers hardness which was even higher than that of monolithic Al_2O_3.

2. Surface crack-disappearance by heat-treatments in air

Investigation of surface crack-disappearance via heat-treatment in air was conducted at temperatures ranging from 1100~1300ºC for 1~24 h. Surface cracks with 180 μm in length completely disappeared by heat-treatments in air at 1100ºC for 24 h or 1200ºC for 6 h. Ultrafine microstructure of the nanocomposites resulted in slightly higher effectiveness of the surface crack-disappearance.

3. Strength recovery at room and high temperatures

Bending strength of 5 vol% Ni/Al_2O_3 nanocomposites as a function of testing temperature is investigated at temperatures ranging from room temperature to 1200ºC. Self-healing performance at high temperatures of the nanocomposites is evaluated by conducting high-temperature bending tests for as-sintered, as-cracked and as-healed specimens. Bending strength of as-sintered specimens dramatically decreases from 995 MPa at room temperature to 205 MPa at 1200ºC. Additionally, the plastic deformation of the as-sintered specimens occurs when the testing temperature reaches to 1200ºC. The

values of high-temperature bending strength of as-healed specimens are comparable with these of as-sintered specimens. Similar to that of as-sintered specimens, bending strength of as-healed specimens is degraded as increase in testing temperature. This fact implies the recovery of bending strength by the self-healing function is able to achieve at temperatures as high as 1200ºC. Unlike the mechanical behaviors at high-temperatures of as-sintered and as-healed specimens, the bending strength of as-cracked specimens slightly increases with increasing testing temperature. This phenomenon is attributed to the effect of the self-healing mechanism during high-temperature bending tests.

4. Oxidation resistance

Investigation for oxidation behavior of Ni/Al_2O_3 nanocomposites was conducted at temperatures ranging from 1100~1300ºC for 1~24 h. Oxidation resistance of Ni/Al_2O_3 nanocomposites was examined through the growth rate of oxidized zone after heat-treatments in air. The growth of oxidized zone obeyed the parabolic law. The apparent activation energy for the growth of oxidized zone was determined to be 400 $kJmol^{-1}$. The influence of Al_2O_3 grain size on oxidation behavior of nanocomposites was discussed. According from the theoretical model, the Al_2O_3 grain size factor is proportional with the parabolic rate constant. However, experimental results show the influence of Al_2O_3 grain size on oxidation behavior was insignificant. It is attributed to the grain growth of Al_2O_3 matrix, especially in oxidized zone during the heat-treatments.

Chapter IV
Self-healing Function and High-temperature Strength of Ni/(ZrO_2+Al_2O_3) Nanocomposites

4.1 Background.

With regard to the mechanical properties of Ni/Al_2O_3 nanocomposites studied in the previous chapter, dispersion of 3 mol% Y_2O_3 stabilized tetragonal ZrO_2 (YZ) in Ni/Al_2O_3 nanocomposites was proposed. Stabilized tetragonal zirconia (t-ZrO_2) is well known as an excellent ceramic which has superior mechanical properties due to transformation-toughening mechanism [93, 94]. Under a stress of crack propagation, tetragonal zirconia particles located around the crack transformed to monoclinic zirconia phase (m-ZrO_2) which induced large volume expansion. The stress induced by volume expansion inhibited against crack propagation that caused them to be stronger and tougher at room temperature. With regard to Al_2O_3 based composites co-dispersed with Ni and t-ZrO_2, Chen et al. reported that the fracture toughness of Ni/(t-ZrO_2+Al_2O_3) composites was higher than the sum of fracture toughness of composites containing only t-ZrO_2 or Ni particles [95]. Nonetheless, t-ZrO_2 is also known as an ionic conductor which would affect oxidation resistance as well as self-healing function of the composites. Ionic conductivity of t-ZrO_2 is due to oxygen vacancies induced by doping some stabilizing materials such as yttria (Y_2O_3), calcia (CaO) or magnesia (MgO) in order to stabilize t-ZrO_2 phase at room temperature [96, 97]. Relating to this fact, Nanko et al. reported high temperature oxidation of Ni particle dispersed t-ZrO_2 composites, in which, O^{2-} diffusion rate was much higher than that of Ni^{2+} that caused volume expansion and consequently resulted in appearance of cracks in oxidized zone [98]. With respect to the study, dispersion of t-ZrO_2 in Ni/Al_2O_3 was considered to be only 10 vol%.

In this chapter, mechanical properties at room temperature such as Vickers hardness, fracture toughness and bending strength of 5 vol% Ni/(10 vol% YZ+Al_2O_3) ceramic nanocomposite were investigated. Investigation of self-healing function of the nanocomposite was conducted at temperatures ranging from 1100 to 1300ºC for 1~24 h in

air. In order to estimate the performance of the nanocomposite, as well as its self-healing function at high temperatures, three-point bending tests were conducted at temperatures ranging from 800 to 1200ºC for as-sintered, as-cracked and as-healed specimens. Oxidation resistance of the nanocomposites is investigated through the growth rate of oxidized zone induced by heat-treatments in air at temperatures ranging from 1100 to 1300ºC for 1~24 h. The influences of YZ dispersion on mechanical properties, self-healing performance and oxidation resistance of the nanocomposites are discussed.

4.2 Experimental procedure.

Specimens used in this study were 5 vol% Ni/(10 vol% YZ+ Al_2O_3), fabricated by the following procedures. The starting powder mixture was prepared by making a slurry mixture containing $Ni(NO_3)_2.6H_2O$ (Kojundo Chemical Laboratory Co. Ltd, purity 99.9%), α-Al_2O_3 (Taimei Chemicals Co. Ltd, TM-DAR, average particle size 0.14 μm, purity 99.99%), 3 mol% Y_2O_3 stabilized ZrO_2 (YZ) (Tosoh Corporation, TZ-3YB, average particle size 0.3 μm, purity 99.9%) and distilled water. Afterward, the slurry mixture was ball-milled in a plastic bottle with 5-mm-diameter alumina balls for 24 h. Then the slurry was dropped into a boiling flask which had been pre-heated at 400ºC to dry up water and decompose nickel nitrate immediately. After grinding by a mortar, the powder mixture was reduced in a stream of Ar-1%H_2 gas mixture at 600ºC for 12 h in order to obtain fine nickel particles dispersed in the YZ-Al_2O_3 matrix. The powder mixture was ball-milled in a plastic bottle with ethanol and 5-mm-diameter alumina balls for 24 h to lessen agglomeration of the powder mixture after reduction. Drying at 80ºC for 12 h in a drying oven and manual crashing by a mortar were done afterward. The powder mixture then was sintered in a graphite die by pulsed electric current sintering (PECS) technique at die temperature of 1300ºC for 5 min holding time, under 50 MPa uniaxial pressure in a vacuum. Relative density (R.D.) of all fabricated specimens and used in this study attained at least 99% of the theoretical density. Fig. 4.1 shows a scanning electron microscope (SEM) image of fractured surface of an as-sintered sample. Nickel particles, which could be observed as bright contrast dots, were homogeneously dispersed in the

matrix. The average particle size of Ni particles was approximately 100 nm, while that of Al_2O_3 and YZ were approximately 300 nm.

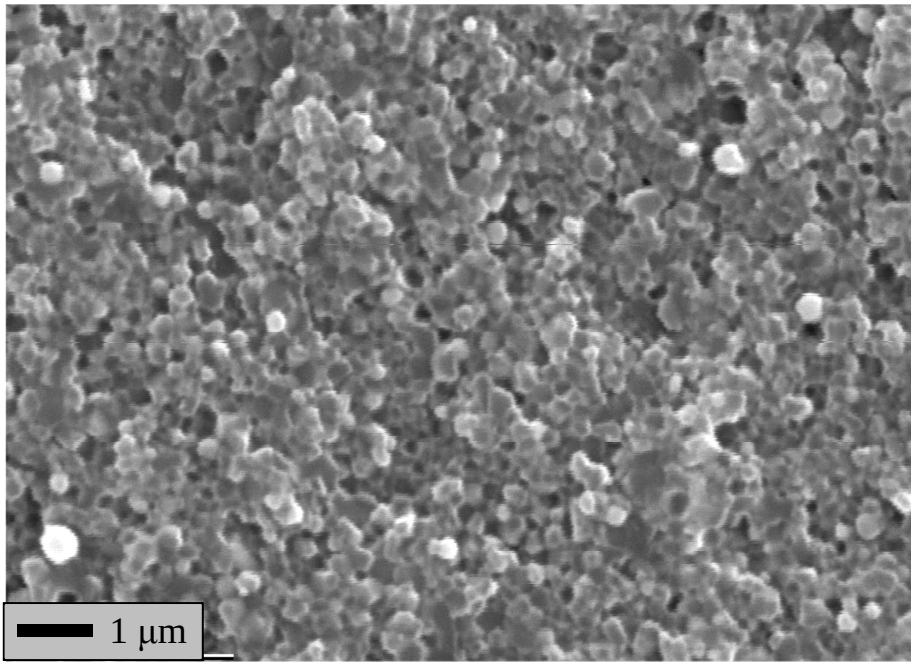

Fig. 4.1. SEM image of fractured surface of as-sintered sample.

Evaluation of the specimens was conducted as the following steps. As-sintered samples were cut into a rectangular shape (3×4×26 mm) for conducting three-point-bending tests. Samples surface were ground by using a grinding wheel with 30-μm-diamond grains and then polished with 2-μm-diamond particle slurry. The polished samples are referred to as-sintered sample, hereafter. After polishing, three Vickers indentations were introduced on center of the sample tension surface by applying a loading of 49 N for 10 s in air in order to induce pre-cracks on the surface. The samples with introduced Vickers indentations are referred to as-cracked samples, hereafter. The geometry of surface cracks introduced on the sample surface by Vickers indentations and placement of samples during three-point bending test could be referred to Fig. 3.3. Each Vickers indentation produces four cracks on sample surface as shown in Fig. 4.2a. The crack size was approximately 200 μm in length. Fig. 4.2b shows the cross-sectional view of a Vickers indentation observed on fractured surface. The dashed line indicates the

front of the semi-elliptical crack introduced by the Vickers indentation. The crack depth was approximately 100 μm. Afterward, mechanical properties such as hardness (H_v) and fracture toughness (K_{IC}) were evaluated by Vickers hardness method and Indentation fracture method [77], respectively. As-cracked samples were heat-treated at temperature ranging from 1100 to 1300ºC for 1 to 24 h in air at 400ºC/h heating rate for investigation of self-healing function. Heat-treatment temperature was monitored by using an R-type thermocouple located near the samples. Surface crack-disappearance was evaluated by fraction of surface crack length before and remaining after heat-treatment, ΔC. The evaluation in detail can be referred in the article written by *Maruoka* et al. [76, 74]. Three-point bending tests were conducted in air with a cross-head speed of 0.5 mm/min at room temperature and temperatures ranging from 800 to 1200ºC for as-sintered, as-cracked and as-healed samples. Testing schedule of high temperature bending tests was conducted with the same one described in Fig. 3.4. The as-cracked samples that were heat-treated at 1200ºC for 6 h in air obtained completely surface crack-disappearance. Therefore, they are called as-healed samples, hereafter. For investigation of oxidation resistance of the nanocomposites, oxidation tests were conducted at temperatures ranging from 1100 to 1300ºC for 1 up to 24 h in the air with a heating rate 400ºC/h. The tested samples were put on alumina balls (3 mm in diameter) in an alumina crucible and exposed in the air at the investigated conditions. Oxidized samples were then cross-sectioned and polished with 2 μm-diamond particle slurry. Oxidation evolution of heat-treated samples was evaluated via the growth rate of oxidized zone observed on cross-sectioned surface by SEM. Analysis of tested specimens is conducted with phase identification by using XRD and microstructure observation by SEM.

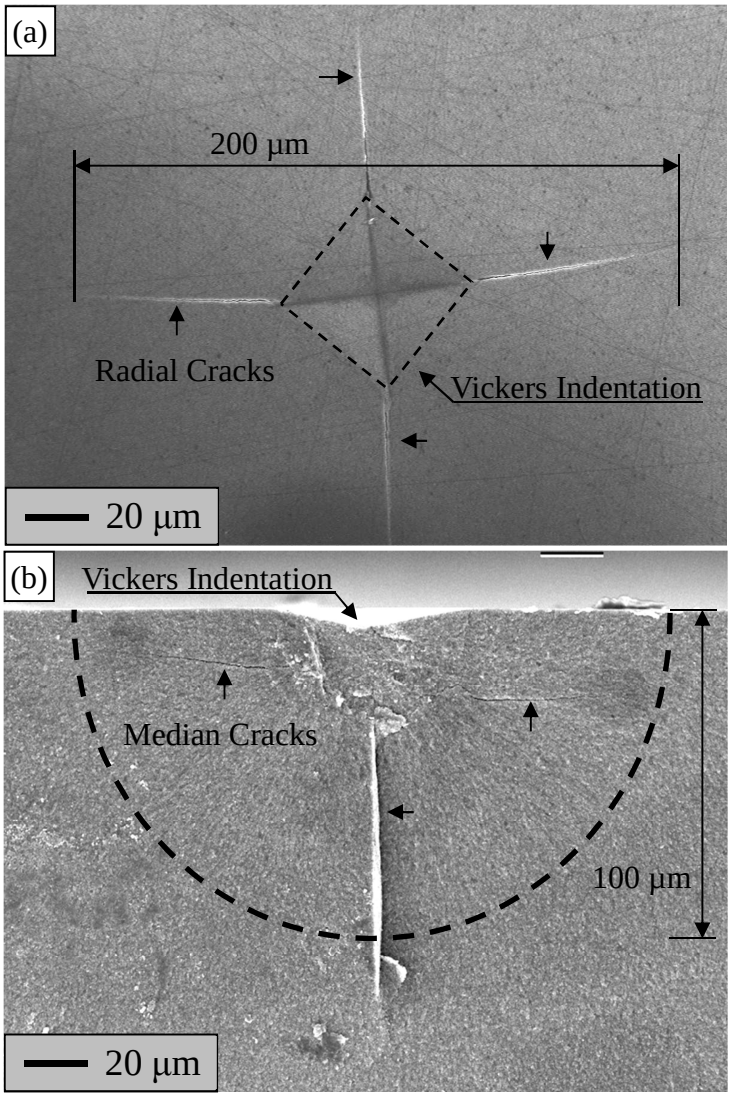

Fig. 4.2. SEM images of Vickers indentation from the top view (a) and cross-sectional view of an as-cracked sample after bending test (b).

4.3 Results and discussion.

4.3.1 Mechanical properties.

Table 1 shows mechanical properties of 5Ni/(10YZ+Al_2O_3) as-sintered specimens investigated at room temperature. At a loading of 49 N for 10 s, the average length of the diagonal left by the pyramidal diamond indenter was 67 μm. Following JIS R 1610 standard, Vickers hardness (H_v) of the as-sintered samples was calculated to be 20±0.3 GPa. The fracture toughness (K_{IC}) of the material calculated by Niihara's equation [77] was

6.1±0.5 MPam$^{1/2}$. The three-point bending strength (σ_b) with 16-mm span length at room temperature of as-sintered specimens was 1218±110 MPa.

Table 4.1. Mechanical properties of 5Ni/(10YZ+Al_2O_3) evaluated at room temperature

Sample	*R.D.*/ %	H_v/ GPa	K_{IC}/ MPam$^{1/2}$	σ_b/ MPa
5Ni/(10YZ+Al_2O_3)	99.6	20±0.3	6.1±0.5	1218±110

Table 4.2 presents the mechanical properties of 5Ni/(10YZ+Al_2O_3) nanocomposites in comparison with the others reported for Al_2O_3 based composites fabricated by various methods. Depending on starting materials and fabrication methods, some alumina based composites achieved very fine Al_2O_3 grain size but had not completely densified yet. On the other hand, some composites had higher density. Nonetheless, grain growth rapidly occurred during sintering process. Generally, bending strength and fracture toughness are considered to be mutually exclusive [99, 100]. For instance, higher porosity leads to higher bending strength, while higher porosity causes lower fracture toughness. Because intrinsic toughening mechanisms are linked to viscosity and thus strength, a compromise is always reached in structure materials where either one of the properties is set aside. In order to improve their mechanical properties, dispersion of YZ was proposed. As expected, 5Ni/(10YZ+Al_2O_3) achieved markedly high bending strength, while fracture toughness was maintained. With regard to Ni/(YZ+Al_2O_3), Chen et al. also reported that the fracture toughness of the composite significantly increased, while it still maintained high bending strength [95]. Fig. 4.3 shows the conflict between bending strength and fracture toughness of alumina based composites. The dashed line and solid line indicate the limit of Ni/Al_2O_3 and Ni/(YZ+Al_2O_3), respectively. It indicates that fracture toughness and bending strength of Ni/Al_2O_3 composites are difficult to increase, simultaneously. By dispersion of YZ, mechanical properties of Ni/(YZ+Al_2O_3) were greater than that of other reported values for Ni/Al_2O_3.

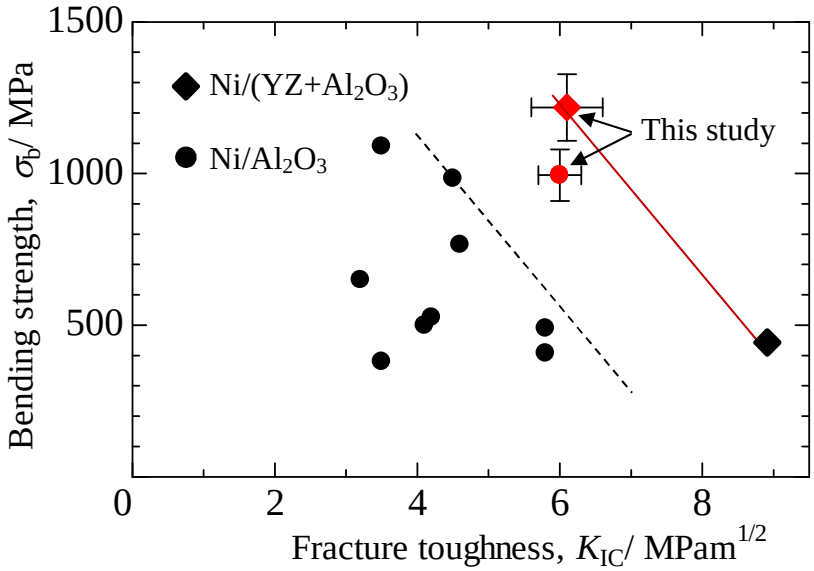

Fig. 4.3. Fracture toughness versus bending strength for alumina based composites.

Table 4.2. Room temperature mechanical properties of Ni/(YZ+Al_2O_3) and Ni/Al_2O_3 composites fabricated by various methods.

Composite	Fabrication	R. D. %	$d_{Al_2O_3}$ μm	H_v GPa	K_{IC} MPam$^{1/2}$	σ_b MPa
5Ni/(10YZ+Al_2O_3) [This study]	PECS	99.9	0.3	20	6.1	1218
7.5Ni/(7.5YZ+Al_2O_3) [95]	Pressureless	>98	-	-	9	480
5Ni/Al_2O_3 [Previous chapter]	PECS	>99	0.5	20	6.1	995
5Ni/Al_2O_3 [78]	Pressureless	>96	0.5	-	4.2	526
7Ni/Al_2O_3 [101]	Pressureless	90	-	-	-	439
3Ni/Al_2O_3 [102]	Pressureless	95	1.49	14	5.8	408
5Ni/Al_2O_3 [21]	Hot press	>98	0.64	-	3.5	1090
5.5Ni/Al_2O_3 [79]	Hot press	>98	1.2	-	4.1	500
5Ni/Al_2O_3 [80]	PECS	>98	1.4	16	3.2	650
5Ni/Al_2O_3 [76]	PECS	>99	1.1	20	5.8	490
3Ni/Al_2O_3 [103]	PECS	>98	-	-	4.6	766
3Ni/Al_2O_3 [104]	PECS	>98	-	-	4.5	984
α-Al_2O_3 [81]	Pressureless	>98	5	15	3.5	380

4.3.2 Surface crack-disappearance.

Figure 4.4 shows SEM images of specimen surface with introduced surface cracks before heat-treatment. Fig. 4.5 shows the surface cracks after heat-treatment at 1100ºC for 12 and 24 h or at 1200ºC for 1 and 6 h. The dashed lines indicate the edges of the Vickers indentation. From each corner of the Vickers indentation, a crack with 55 μm in length propagated as observed in Fig. 4.4a. The width of the crack near the vertex of the Vickers indentation was determined to be approximately 1 μm (Fig. 4.4b). After heat-treatment at 1100^{o}C for 12 h in air, oxidation product that can be observed as bright contrast particles was formed on sample surface, as shown in Fig. 4.5a. The fraction of crack-disappearance at this condition was determined to be 75±15%. For longer heat-treatment time, heat-treatment at 1100^{o}C for 24 h, particle-like oxidation product formed and covered sample surface that leads to the disappearance of the cracks, as shown in Fig. 4.5b. At 1200^{o}C, complete surface crack-disappearance can be achieved with a short heat-treatment time such as 1 h, as shown in Fig. 4.5c. Heat-treatment at 1200^{o}C for 6 h in air makes significant formation of oxidation product, as shown in Fig. 4.5d.

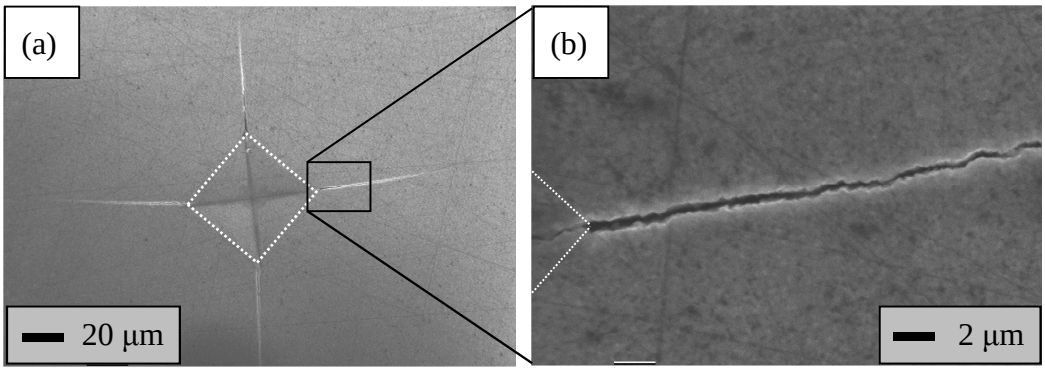

Fig. 4.4. SEM images showing the top view of (a) Vickers indentation and (b) surface crack of as-cracked specimens before heat-treatment in the air.

Figure 4.6 shows XRD patterns for phase identification of exposed surface before and after heat-treatment in air. Before heat-treatment, there were three dominant compounds that were α-Al_2O_3, YZ and Ni detected on the sample surface. After heat-treatment in air, peaks of $NiAl_2O_4$-oxidation product appeared. With higher temperature and longer

heat-treatment duration, these $NiAl_2O_4$ peaks became more intensive and gradually replaced for appearance of metallic Ni peaks.

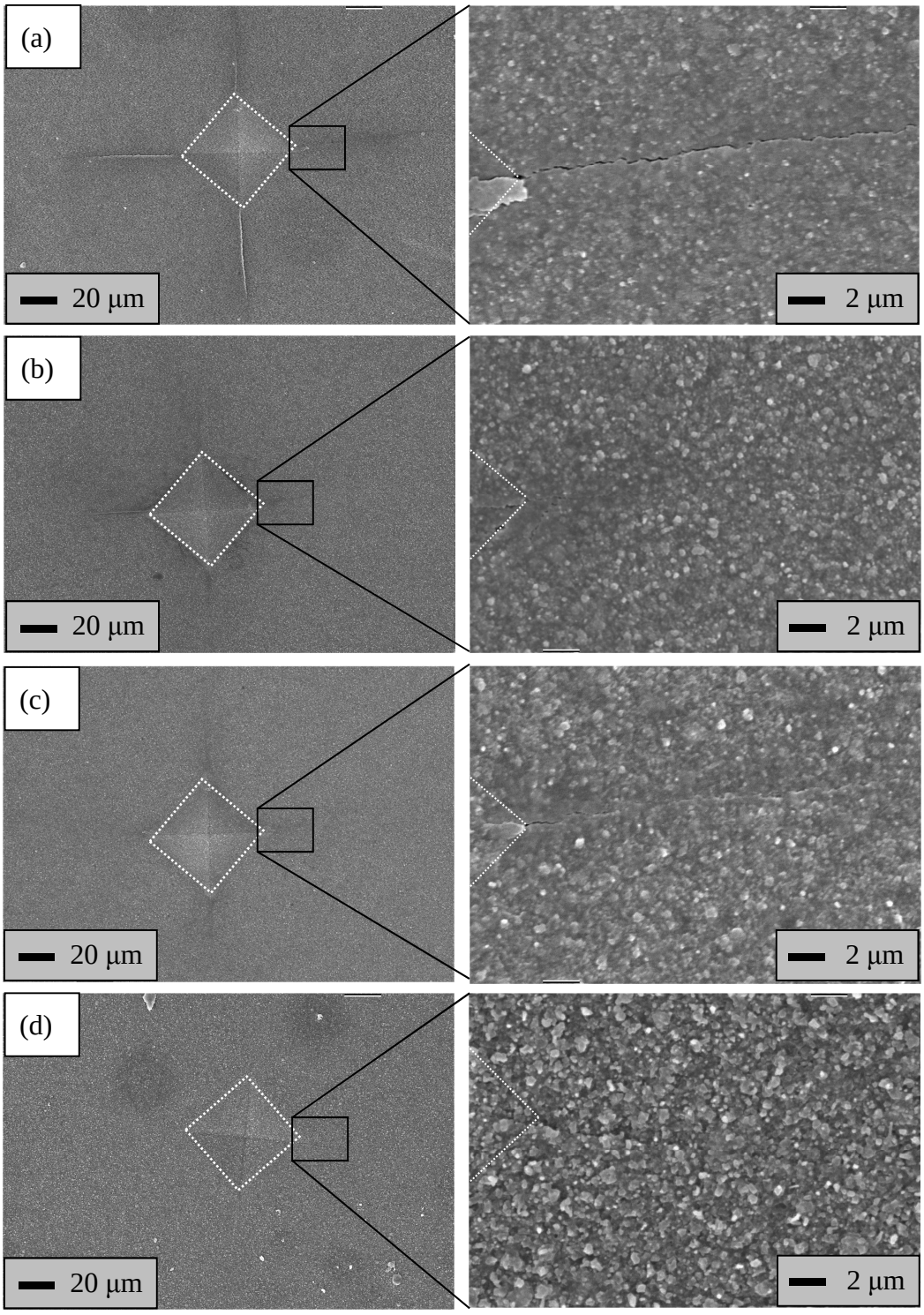

Fig. 4.5. SEM images show the top view of as-cracked specimens after heat-treatments at (a) 1100ºC for 12 h, (b) 1100ºC for 24 h, (c) 1200ºC for 1 h and (d) 1200ºC for 6 h in air.

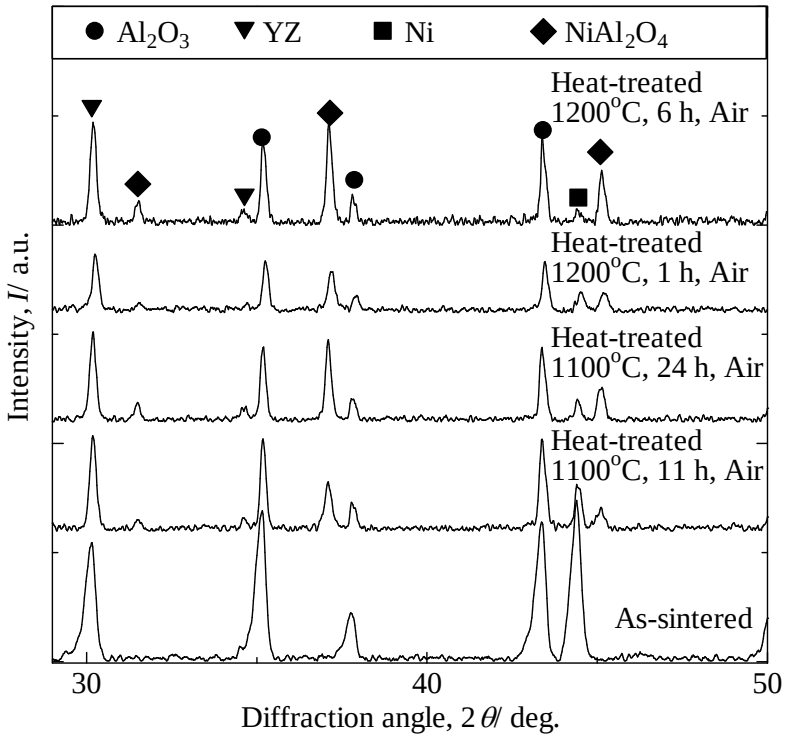

Fig. 4.6. XRD patterns for phase identification of exposed sample surface before and after heat-treatment.

Self-healing mechanism of Ni/Al_2O_3 nanocomposites has been clarified in numerous articles over the past few years [65, 74-76]. Oxidation of Ni in Al_2O_3 matrix at high temperatures develops the oxidation product which fills up and covers the surface cracks. Self-healing function is depended on outward diffusion of Ni^{2+} which plays a major role in formation of oxidation product on top sample. Thicker layer of the oxidation product leads to more effective self-healing performance. As shown in Fig. 4.6, $NiAl_2O_4$-the only oxidation product, was detected regardless of heat-treatment time and temperature. According to the ternary phase diagram of the Ni-Al-O [82], NiO-Al_2O_3-ZrO_2 [105] system, NiO does not coexist with either Al_2O_3 or ZrO_2. Nanko et al. [92] reported high temperature oxidation behavior of nano-Ni/Al_2O_3. In the study, a 5-μm-thickness layer of $NiAl_2O_4$ and 200-μm-depth oxidized zone were observed on the surface of sample oxidized at 1300°C for 3 d in air. Taking account of self-healing function and oxidation resistance, amount of YZ dispersion must be considered due to its specific characteristic. YZ is known as ion conductors which could affect diffusion of ion and cation [93, 94].

According to Nanko *et al.* [98], diffusion of oxygen ion in Ni/YZ system was significantly fast that caused crack propagation surrounding oxidized Ni particles. With respect to its mechanical properties, larger amount of YZ dispersion in Ni/Al_2O_3 may induce greater mechanical properties. However, it also may involve in worse oxidation resistance and insufficiency of self-healing function. By 10 vol% YZ dispersion in Ni/Al_2O_3, the nanocomposite achieved improved mechanical properties and had self-healing function as same as Ni/Al_2O_3 nanocomposites.

4.3.3 Self-healing-induced strength recovery.

Figure 4.7 plotted the bending strength of as-sintered, as-cracked and as-healed sample as function of tested temperature. At room temperature, bending strength of as-sintered samples was determined as 1218±110 MPa. Bending strength of as-cracked samples (three Vickers indentations introduced on each sample) only achieved 145±5 MPa. By heat-treatment at 1200^{o}C for 6 h in air, cracks on as-healed samples disappeared completely as shown in Fig. 4.5d. Nevertheless, as-healed samples only achieved 690±30 MPa in bending strength. At 800^{o}C, bending strength of as-sintered samples dropped to 525±40 MPa, while that of as-healed samples decreased to the value of 400±50 MPa. In the meantime, bending strength of as-cracked samples slightly increased to 190±5 MPa. At 1000^{o}C, bending strength of as-sintered, as-healed and as-cracked samples was 640±123, 445±20 and 360±6 MPa, respectively. At 1200^{o}C, the value of as-sintered samples was 460±120 MPa, while that of as-cracked samples maintained at 375±5 MPa. In contrast to the mechanical behavior of as-sintered samples at high temperatures, mechanical behavior of as-healed samples was markedly different at high temperatures. Bending strength of as-healed samples was 805±110 MPa, even higher than the value that was determined at room temperature.

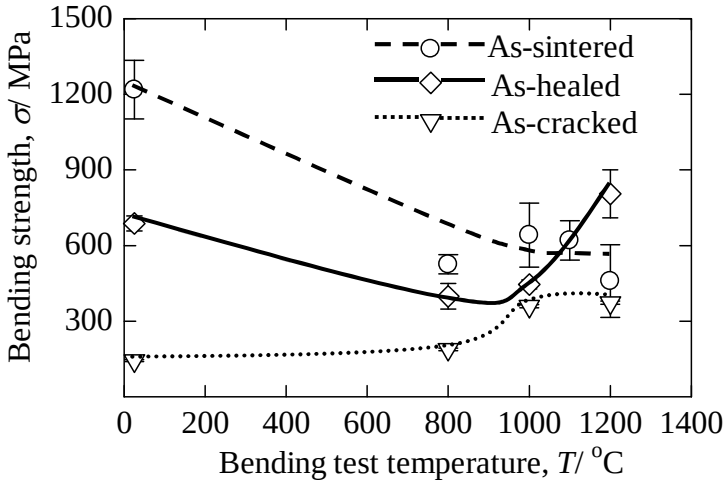

Fig. 4.7. Bending strength of as-sintered, as-cracked and heat-treated samples as function of tested temperatures.

High temperature bending test was conducted for as-cracked samples in order to estimate performance of damaged samples at high temperature. Brittle materials, such as alumina and other ceramics, fracture from the highest stress concentration at the largest defects. During the bending tests conducted at room temperature, as-cracked samples fractured along the surface cracks introduced by Vickers indentations, as shown in Fig. 4.8a. At high temperature, bending strength of as-cracked samples increased by increasing testing temperatures. Noticeably, bending strength of as-cracked samples at 1000 and 1200^{o}C was twice times higher than that of the samples conducted at room temperature. Observation for fractures of as-cracked samples conducted at 1000 and 1200^{o}C indicates that the samples fractured along 2 out of 3 Vickers indentations introduced, as shown in Fig. 4.8(c) and (d). Phase identification for as-cracked sample after high temperature bending test, as shown in Fig. 4.9, shows that $NiAl_2O_4$ peaks appeared clearly for the samples conducted at 1200^{o}C. Fig. 3.4 demonstrates the testing schedule of high temperature bending tests that may answer for the appearance of $NiAl_2O_4$. The samples were heated up to 1200^{o}C within 2 h in air, before the tests were conducted. *Maruoka* et al. [76] investigated recovery of mechanical strength as function of surface crack-disappearance fraction in Ni/Al_2O_3 system. They concluded that recovery of mechanical strength for nano-Ni/Al_2O_3 can be expected to be achieved when the fraction of surface crack-disappearance is over 50%. The increase of bending strength for

as-cracked samples at high temperatures is thus implied to the self-healing mechanism.

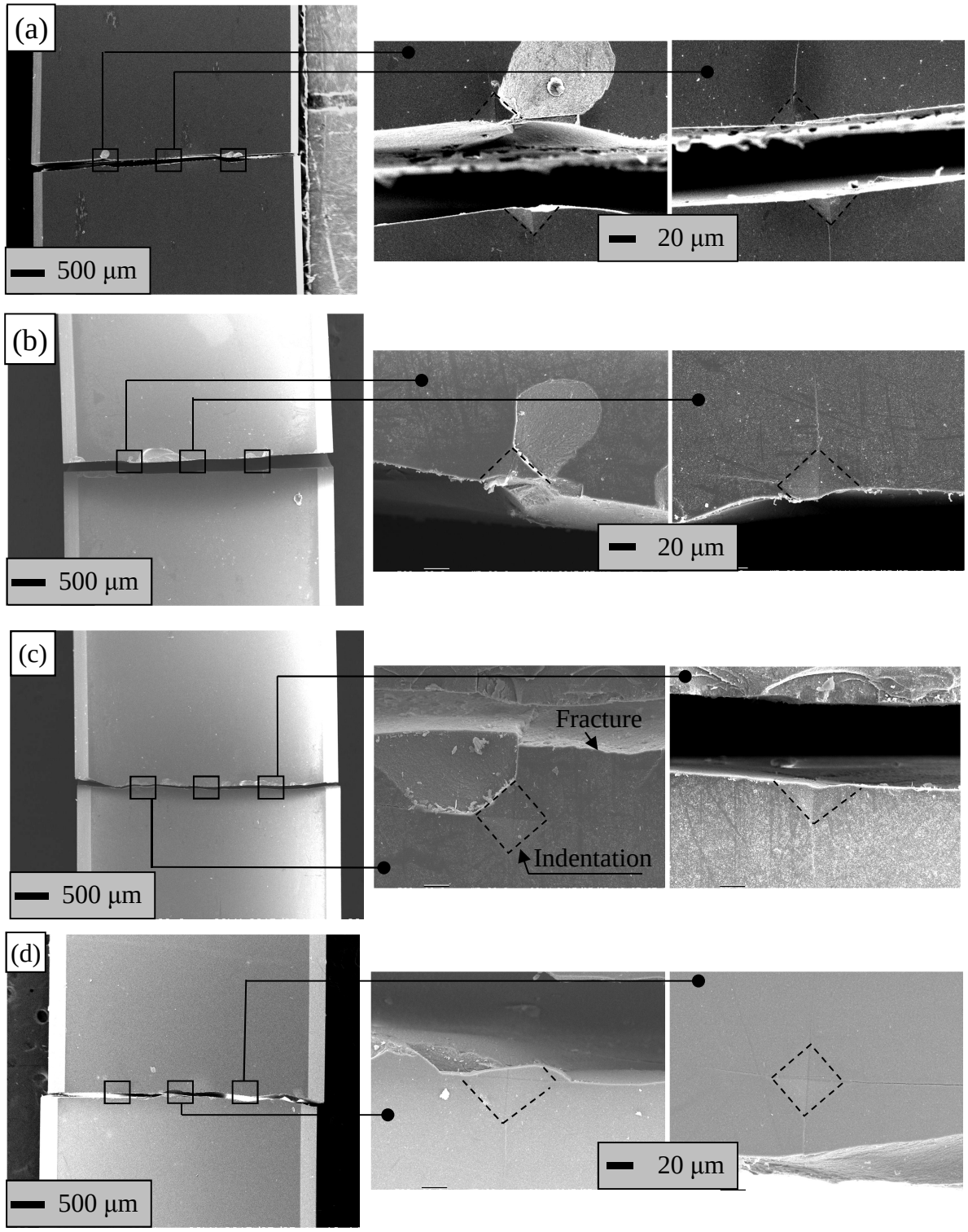

Fig. 4.8. SEM images of as-cracked samples showing the fracture after bending tests conducted at (a) room temperature, (b) 800, (c) 1000 and (d) 1200ºC.

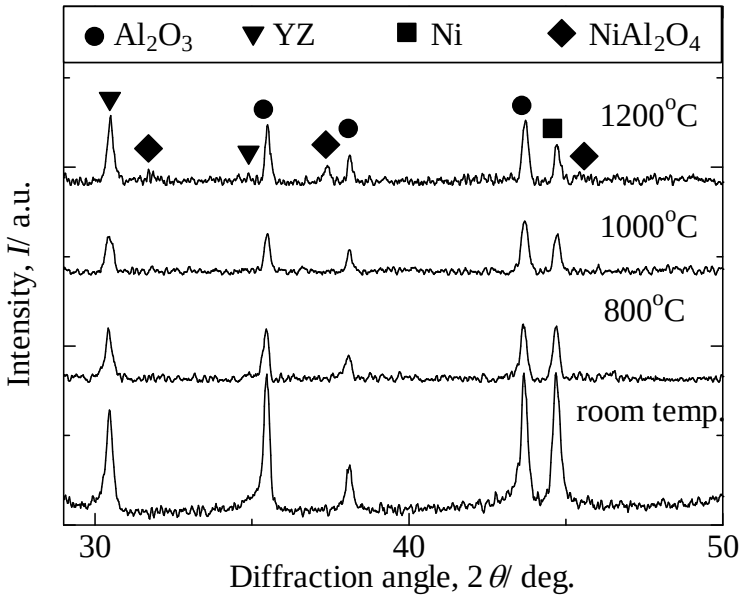

Fig. 4.9 XRD patterns of exposed sample surface for as-cracked samples after bending tests conducted at room temperature, 800, 1000 and 1200ºC.

Bending strength of as-sintered samples was tested at room and temperatures ranging from 800 to 1200ºC for the performance of the nanocomposite at high temperatures, as the first stage when it was fabricated. At room temperature, the as-sintered samples exhibited remarkably high bending strength. Nevertheless, it dramatically decreased when the testing temperature reached 800ºC. At 1000ºC, bending strength of as-sintered samples slightly increased compared to the value achieved at 800ºC. This fact could be explained by the existence of defects observed on samples tested at 800ºC as shown in Fig. 4.10(a). No defect could be found at the stress concentration point of sample after bending test at 1000ºC, as shown in Fig. 4.10(b). Accordingly, the dashed line shown in Fig. 4.7 is representative for the mechanical degradation of as-sintered samples as temperature increases. With regard to the degradation of the nanocomposite at high temperatures, Evans et al. reported that high temperature mechanical properties of general polycrystalline ceramics are dependent on slow crack growth caused by cavitations and/or grain boundary sliding [83]. In addition, Niihara et al. reported that the mechanical degradation at high temperatures of 5 vol% SiC/Al_2O_3 was getting worse than that of monolithic Al_2O_3

ceramic due to the mismatch stress between the dispersoids and the matrix [25]. The mismatch stress of the nanocomposite at high temperatures was caused by the difference in coefficients of thermal expansion (CTE) that propagated slow crack growth at cavities. Therefore, the difference in CTE must be taking into account with respect to high temperature mechanical properties of composites.

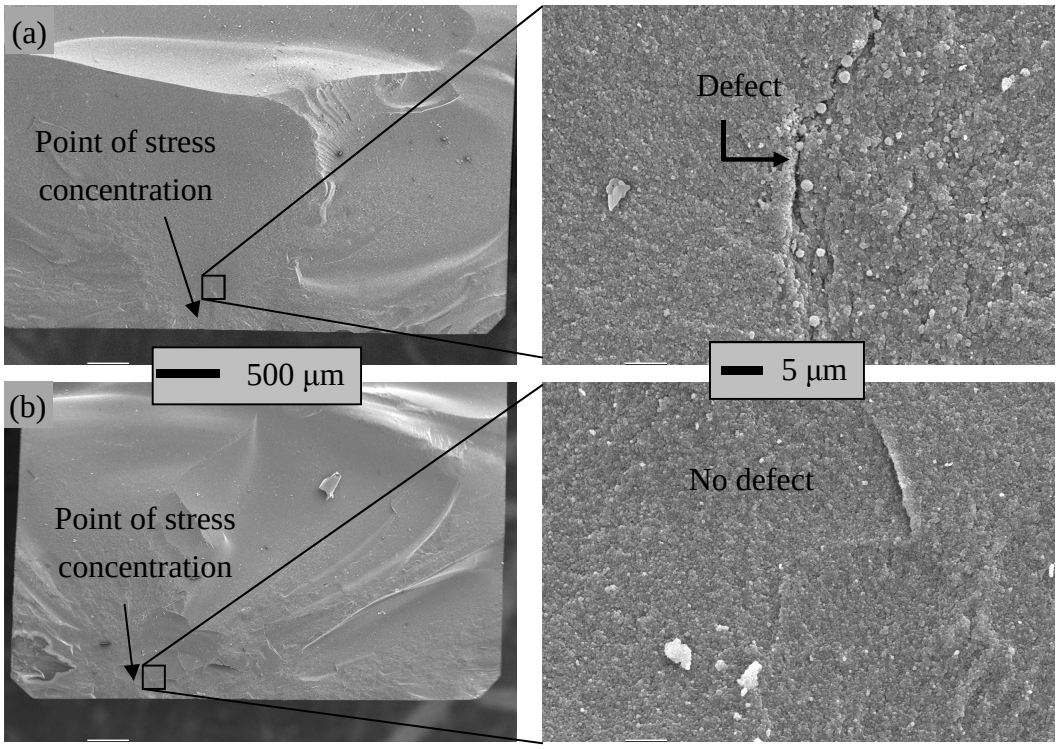

Fig. 4.10 SEM images of fractured surface observed on as-sintered samples after bending tests at (a) 800ºC and (b) 1000ºC.

In order to evaluate the effectiveness of self-healing function at high temperatures, bending tests were conducted for as-healed samples at room temperature, 800, 1000 and 1200ºC. Bending strength value of as-healed samples at room temperature was only 690 MPa, lower than that of as-sintered samples in spite of the fact that the surface cracks completely disappeared after heat-treated at 1200ºC for 6 h in air. Nonetheless, the situation is markedly different at high temperatures. Bending strength of as-healed samples at 1200ºC was 800 MPa, higher either as-healed samples tested at 1000, 800ºC or room temperature. Fig. 4.11 shows the fracture of as-healed samples after bending tests

at various temperatures. Fig. 4.11(a) shows the fracture of as-healed sample tested at room temperature propagated across one of the three Vickers indentations. At 800ºC, the fracture propagated across all the three Vickers indentations, which implied that the healed cracks were the higher stress concentration points, as shown in Fig. 4.11(b). At higher bending test temperatures, fracture of as-healed samples tested at 1000ºC propagated only one out of three Vickers indentations, as shown in Fig. 4.11(c), which is similar with that of samples tested at room temperature. Fig. 4.11(d) shows the fracture of as-healed samples tested at 1200ºC was in the different region from the region that the Vickers indentations were introduced, which indicates the region including Vickers indentation was no longer being the highest stress concentration. In order to understand this phenomenon, the authors suggest that the greater bending strength of as-healed samples at high temperatures was caused by stress relaxation between the oxidized region and non-oxidized region. Since the as-healed samples were heat-treated at 1200ºC for 6 h in air, metallic Ni particles that exposed in air were oxidized which caused volume expansion. Similar to the transformation-toughened mechanism of tetragonal-ZrO_2, sudden volume expansion of metallic Ni particles in the early stage might induce the volume expansion of nearby ZrO_2 particles due to transformation of tetragonal phase to monoclinic phase. Nanko et al. reported high temperature oxidation behavior of particle-Ni dispersed Y_2O_3 partially-stabilized ZrO_2 composites [98], in which, only oxygen ions inward diffused and there was no outward diffusion of nickel cations that caused volume expansion of oxidation product. The volume expansion of oxidation product within the matrix therefore induced appearance of cracks in oxidized region. The volume expansion of ZrO_2 and Ni oxide in oxidized zone might cause mismatch stress between the oxidized zone and non-oxidized zone. In consideration of damaged region caused by Vickers indentation as shown in Fig. 4.2(b), the region including the Vickers indentation, in which, metallic-Ni particles exposed, was the deepest region that caused highest stress concentration due to the mismatch stress. At 1200ºC, the mismatch stress of as-healed samples was much lower than that of the samples tested at room temperature because of phase transformation of ZrO_2 between monoclinic phase to tetragonal phase. Relaxation of the mismatch stress at high temperatures is attributed to play an important role

responsible for the greater mechanical properties of as-healed samples at high temperatures.

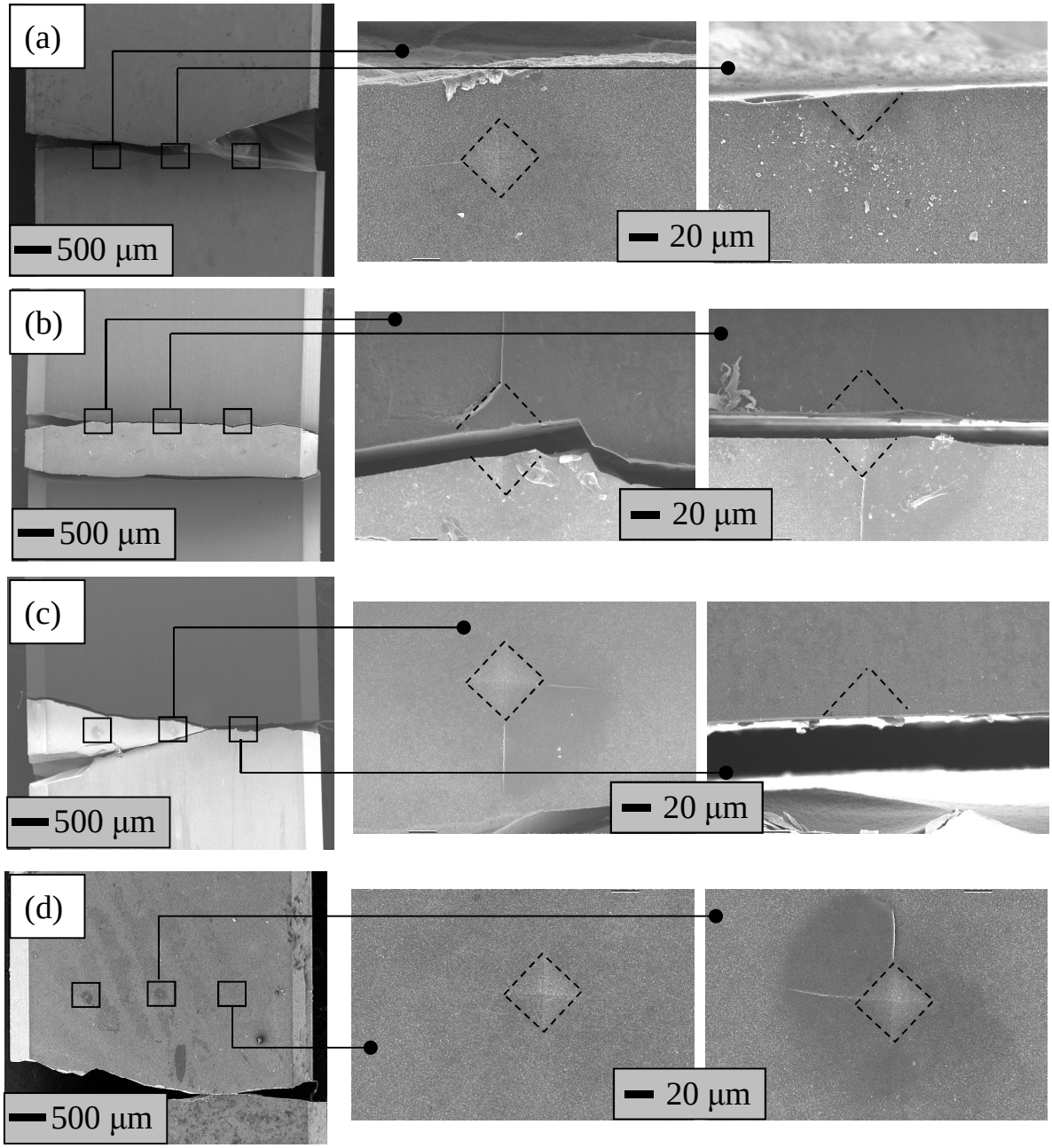

Fig. 4.11 SEM images of as-healed specimens fractured in bending tests conducted at (a) room temperature, (b) 800, (c) 1000 and (d) 1200ºC.

Figure 4.12 plotted the bending strength values of Ni/Al_2O_3 and Ni/(YZ+Al_2O_3) nanocomposites as the function of bending test temperatures. YZ dispersion obviously influences on high-temperature strength of Ni/Al_2O_3 nanocomposites at room temperature as well as high temperatures. As discussed in the previous chapter, Ni/Al_2O_3 nanocomposites exhibits poor mechanical strength at 1200ºC as they plastic deformed with the speed rate of 0.5 mm/min. With 10 vol% YZ dispersion, Ni/(YZ+Al_2O_3) nanocomposites achieved 460 MPa at 1200ºC and did not show plastic deformation.

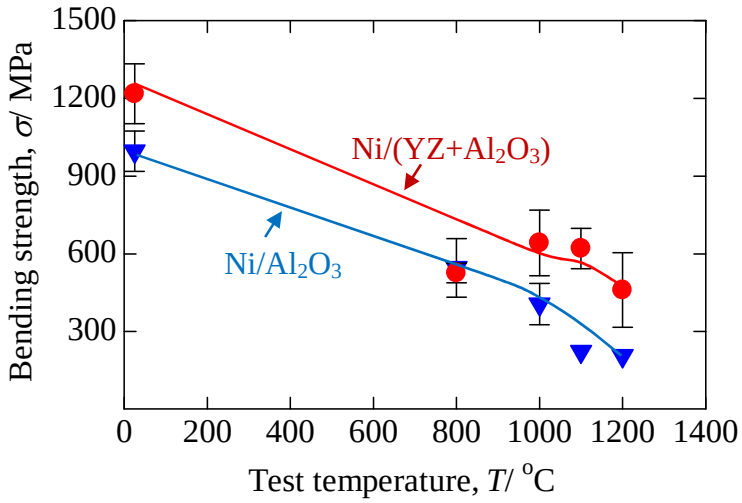

Fig. 4.12 High-temperature strength as a function of bending test temperature of Ni/Al_2O_3 and Ni/(YZ+Al_2O_3) nanocomposites.

4.3.4 Oxidation resistance.

Figure 4.13 shows SEM images observed on cross-sectioned surface of Ni/(YZ+Al_2O_3) nanocomposites after oxidations at 1300ºC for (a) 6 h and (b) 12 h. A thin surface layer formed on both samples. Thickness of the surface layer formed on sample oxidized at 1300ºC for 12 h (Fig. 4.13b) was approximately 1.5 µm which is slightly thicker than that formed on sample oxidized at 1300ºC for 6 h (1µm), as shown in Fig. 4.13a. The internal oxidized zone was defined to be the region containing the matrix, oxidation product and the cavitations induced by diffusions. As shown in Fig. 4.13, thickness of the oxidized zone developed as oxidation duration increased. The thickness

of oxidized zone as a function of oxidation time at various temperatures was plotted in Fig. 4.14. The growth of oxidized zone obeyed the parabolic law. Fig. 4.15 plotted the parabolic rate constant k_p on the growth of oxidized zone in Ni/(YZ+Al_2O_3) as a function of reciprocal oxidation temperature. The apparent activation energy for the growth of oxidized zone in Ni/(YZ+Al_2O_3) was calculated to be 503 kJmol^{-1}, which is higher than that of Ni/Al_2O_3 nanocomposites (400 kJmol^{-1}). The oxidation rate of Ni/(YZ+Al_2O_3) was also one order of magnitude higher than Ni/Al_2O_3 nanocomposites. In other words, oxidation resistance of Ni/(YZ+Al_2O_3) nanocomposites is worse than that of Ni/Al_2O_3 nanocomposites.

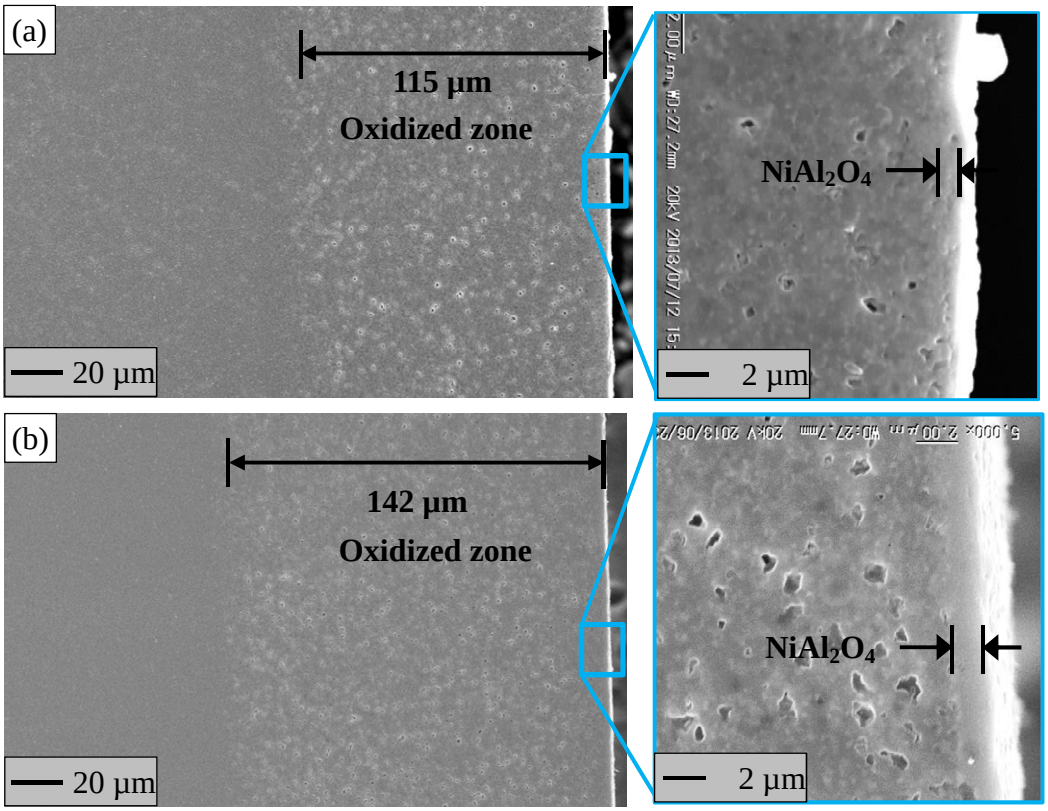

Fig. 4.13 SEM images show the cross-sectioned surfaces of Ni/(YZ+Al_2O_3) specimens after oxidation at (a) 1300ºC for 6 h and (b) 1300ºC for 12 h.

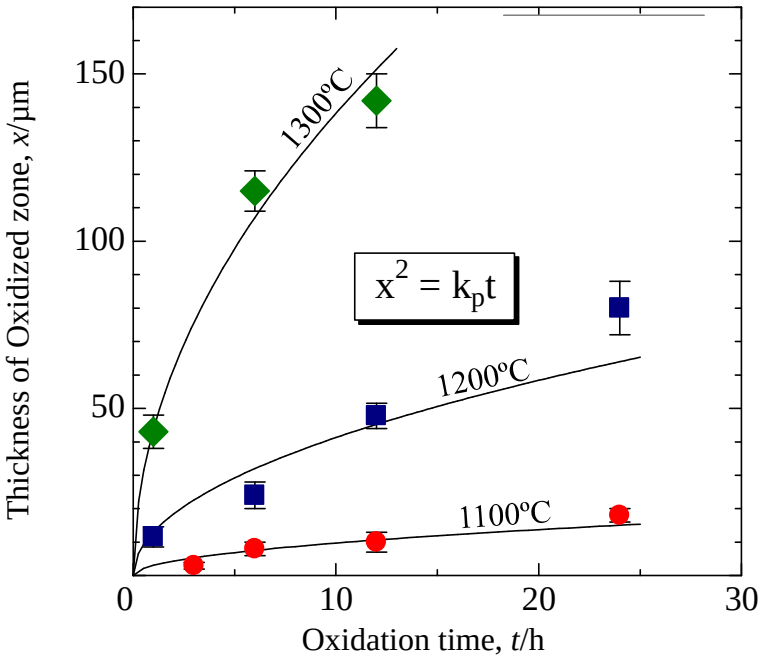

Fig. 4.14 Thickness of oxidized zone as a function of oxidation time at various temperatures for Ni/(YZ+Al_2O_3) nanocomposites.

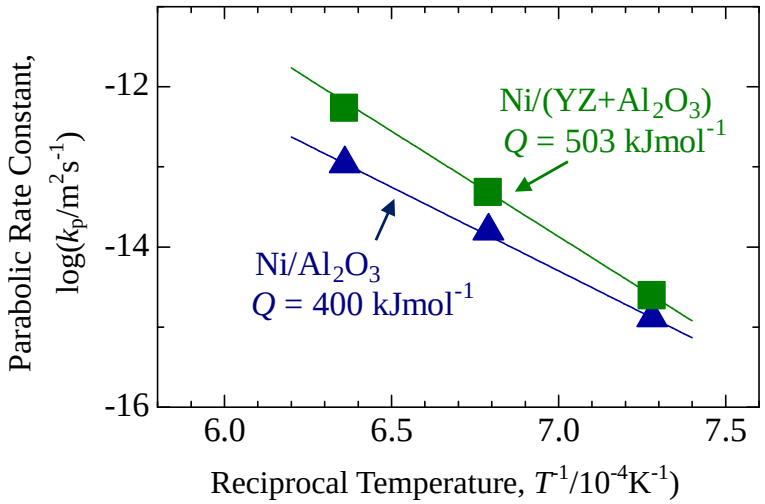

Fig. 4.15 Temperature dependence of parabolic rate constant on growth of oxidized zone in Ni/(YZ+Al_2O_3) and Ni/Al_2O_3 systems.

In general, oxidation behavior of Ni/Al_2O_3 composites is controlled by grain boundary diffusions as described in chapter II & III. Taking account of Ni/(YZ+Al_2O_3) microstructure as shown in Fig. 4.1, the average grain size was almost equal with that of Ni/Al_2O_3 nanocomposites. However, oxidation rate of Ni/(YZ+Al_2O_3) nanocomposites

was higher one order of magnitude than that of Ni/Al_2O_3 nanocomposites. It is due to the dispersion of YZ. YZ is known as an ion conductor as mentioned previously. Doping of Y_2O_3 creates oxygen vacancies which allow oxygen ions penetrate ZrO_2 crystals. It means that oxygen ions can diffuse through YZ granular. In other words, diffusion of oxygen ions in YZ includes grain boundary and bulk diffusions [106]. Hence, dispersion of YZ in Ni/(YZ+Al_2O_3) provides more diffusion path for oxygen ions. Higher amount of YZ dispersion leads to worse oxidation resistance of Ni/(YZ+Al_2O_3) nanocomposites. Therefore, introduction of YZ for higher mechanical properties must be taken into consideration from the oxidation kinetic point of view.

4.4 Conclusions.

Consolidated 5 vol% Ni/(10 vol% YZ+Al_2O_3) specimens were fabricated by PECS to investigate the self-healing function and mechanical strength at room and high temperatures. Characterizations of the nanocomposites were studied via mechanical properties at room temperature, surface crack-disappearance, high-temperature strength, and oxidation resistance. The following conclusions are based on each characteristic:

1. Mechanical properties

Investigations of some mechanical properties such as hardness, fracture toughness and bending strength of Ni/(YZ+Al_2O_3) nanocomposites were conducted at room temperature to estimate the influences of YZ dispersion. The consolidated Ni/(YZ+Al_2O_3) specimens achieved 6.1 $MPam^{1/2}$ in fracture toughness, 1218 MPa in bending strength, and 20 GPa in Vickers hardness. The results of the investigation indicated that YZ dispersion improved the bending strength of Ni/(YZ+Al_2O_3) nanocomposites while maintained high fracture toughness. In other words, mechanical properties of Ni/(YZ+Al_2O_3) nanocomposites are greater than that of Ni/Al_2O_3 nanocomposites reported in the previous chapter.

2. Surface crack-disappearance

The investigation of surface crack-disappearance by heat-treatment in air was conducted at temperatures ranging from 1100 to 1300ºC for 1 to 24 h. Results of the investigation indicated the surface crack-disappearance achieved by heat-treatment of 5Ni/(10YZ+Al_2O_3) was similar with that of 5Ni/Al_2O_3. For example, surface cracks with approximately 200 µm in length completely disappeared by heat-treatment in air at 1100ºC for 24 h or 1200ºC for 1 h. Dispersion of 10vol% YZ shows less influences on surface crack disappearance of Ni/(YZ+Al_2O_3).

3. Strength recovery at room and high temperatures

Self-healing performance at high temperatures of 5Ni/(10YZ+Al_2O_3) nanocomposites is evaluated by conducting high-temperature bending tests for as-sintered, as-cracked and as-healed specimens. The bending tests were carried out at temperatures ranging from room temperature to 1200ºC. At room temperature, dispersion of YZ contributed high bending strength (1200 MPa) and fracture toughness (6.1 $MPam^{1/2}$) to the nanocomposite. At high temperature, bending strength of the nanocomposite decreased markedly because of mismatch stress induced by the difference in thermal expansion coefficients of the matrix and dispersoids. High bending test conducted on as-cracked samples indicated that partially recovery of mechanical strength can be achieved immediately when the nanocomposite is applied at high temperatures. As-healed samples only achieved 690 MPa in bending strength at room temperature despite the fact that surface cracks completely disappeared. This phenomenon is caused by the mismatch stress between oxidized zone and non-oxidized zone. At high temperature, the mismatch stress was decreased that made the as-healed samples stronger than the as-healed sample tested at room temperature. Dispersion of YZ contributes to Ni/(YZ+Al_2O_3) nanocomposites higher mechanical properties either at room temperature or high temperatures.

4. Oxidation resistance

Oxidation tests for Ni/(YZ+Al_2O_3) were conducted at temperatures ranging from 1100 to 1300ºC for 1 to 24 h. Oxidation zone was composed of a surface layer and internal oxidized zone. The growth of internal oxidized zone obeyed the parabolic law. The parabolic rate constant on growth of oxidized zone for Ni/(YZ+Al_2O_3) was determined to be 503 $kJmol^{-1}$. The oxidation rate of Ni/(YZ+Al_2O_3) was one order of magnitude higher than Ni/Al_2O_3. In other words, dispersion of YZ degrades the oxidation resistance of Ni/(YZ+Al_2O_3) nanocomposites.

Chapter V
Self-healing Function of Ni/mullite Nanocomposites

5.1 Background.

Investigation of self-healing function for Ni/mullite is conducted as an alternative choice for self-healing function of oxide ceramic-based composites. As the strength degradation at high temperatures of Ni/Al_2O_3 and Ni/(YZ+Al_2O_3) nanocomposites, Ni dispersed mullite matrix composites are considered as a candidate for self-healing ceramics. Mullite matrix is known as a greater material than Al_2O_3 in terms of creep property and oxidation resistance [107, 108]. *Lessing* et al. reported the creep rate at 1450ºC of dense mullite was approximately one order of magnitude less than that of monolithic Al_2O_3 [109]. From the reasons above, Ni/mullite nanocomposites with self-healing function could be suitable for the high-temperature applications.

In this chapter, the investigation of self-healing function for 5 vol% Ni/mullite is conducted. The self-healing ability is estimated through the fraction of surface crack-disappearance before and after heat-treatment in air at 1000 to 1200ºC for 1-24 h. The effectiveness of self-healing function on their strength recovery is examined by three-point bending tests conducted for as-sintered, as-cracked and as-healed samples. In order to clarify the self-healing mechanism as well as the oxidation resistance of the composites, oxidation tests are carried out at temperatures ranging from 1200 to 1400ºC for 1 to 48 h. Some basic information on mechanical properties of the nano-Ni/mullite composites such as hardness and fracture hardness are also provided.

5.2 Experimental procedure.

Samples preparations of 5 vol% Ni/mullite composite was carried out as the following procedure. A slurry mixture containing $Ni(NO_3)_2.6H_2O$ (Kojundo Chemical Laboratory Co. Ltd), mullite powder (KCM Corporation, KM101, d = 0.7 μm) and distilled water was prepared by ball-milling for 24 h in a plastic bottle with alumina balls (5 mm in diameter). The slurry mixture was then dropped into a boiling flask that was pre-heated at 400ºC for

the dehydration. The dried powder was ground by using a grinding alumina mortar before the reduction process. The reduction process was carried out at 600ºC for 12 h in a stream of Ar-1%H_2 gas mixture to reduce NiO to Ni. For deagglomeration, the powder mixture was ball-milled in a plastic bottle with ethanol and the alumina balls for 24 h. Drying at 80ºC for 12 h and manual crashing by alumina mortar were carried out afterward. Consolidation of the powder mixture was conducted by pulsed electric current sintering technique (PECS) with a graphite die in a vacuum at 1550ºC for 5 min holding time and under 50 MPa in uniaxial pressure. The relative density (R.D.) of all the samples fabricated by this procedure attained at least 99% of the theoretical density. Fig. 5.1 shows the scanning electron microscope (SEM) image of the fractured surface of an as-sintered sample. The bright contrast dots are Ni particles that have the average particles size of 0.5 μm. The average grain size of mullite is approximately 2 μm. Several cavities which are also observed to be the same size with Ni particles formed by the detachment of Ni particles during the fracture process.

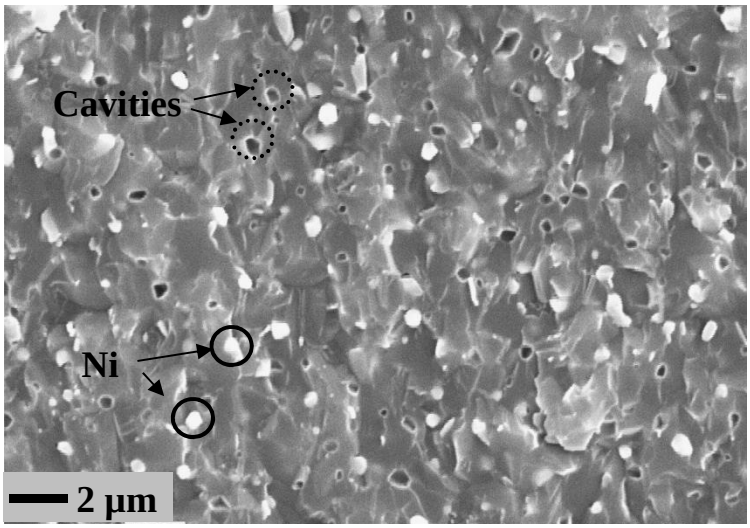

Fig. 5.1 SEM image shows the fractured surface of an as-sintered sample. Ni particles are visible as the bright dots. The cavities are attributed to the result of the intergranular fracture mechanism, in which, the fracture propagates along the interface between Ni particles and the matrix. The detachment of Ni particles during the fracture process induces the cavitation.

The evaluation of samples was conducted as the following steps. Sintered samples were cut into a rectangular shape (3x4x26 mm) for three-point bending tests. Sample surface was ground by a grinding wheel with diamond grains (30 μm) and then polished with diamond particle slurry (2 μm). The polished samples are referred to as-sintered samples, hereafter. After polishing, three Vickers indentations were introduced at the center of samples by applying a load of 19.6 N for 10 s to induce pre-cracks on the surface. The samples with the surface pre-cracks induced by Vickers indentations are referred to as-cracked samples, hereafter. Each Vickers indentation produces four cracks at their corners, as shown in Fig. 5.2(a). The crack size in total is approximately 180 μm in length. Fig. 5.2(b) shows the cross-sectional view of the Vickers indentation observed on the fractured surface. The dashed line indicates the front of the semi-elliptical crack introduced by the Vickers indentation. The crack depth is approximately 90 μm. To investigate the surface crack-disappearance, as-cracked samples were heat-treated in the air at a temperature ranging from 1000 to 1200ºC for 1-24 h with a heating rate of 400ºC/h. Heat-treatment temperature was monitored by using an R-type thermocouple located near the samples. The surface crack-disappearance was evaluated by the fraction (ΔC) of the twelve surface cracks length induced by three Vickers indentations before and after heat-treatment. Details of this evaluation method have been reported elsewhere [76]. To estimate the effectiveness of the self-healing function on their strength recovery, three-point bending tests were carried out at a 16 mm outer span length and a crosshead displacement rate of 0.5 mm/min at room temperature. Samples of bending tests were set into the loading geometry with the surface including Vickers indentations on the tensile surface, as shown in Fig. 3.4. Phase identification and microstructure observation of samples were carried out by using X-ray diffraction (XRD) and SEM, respectively. Evaluations of some mechanical properties such as hardness (H_v) and fracture toughness (K_{IC}) were evaluated by Vickers hardness method following JIS R 1610 standard, and Indentation fracture method [77], respectively. To estimate the influence of Ni dispersion on their mechanical properties, monolithic mullite was also fabricated with the similar sintering process of the nanocomposite. For investigation of oxidation resistance of the composites, oxidation tests were conducted at temperatures ranging from 1200 to 1400ºC

for 1 up to 48 h in the air with a heating rate 400ºC/h. The tested samples were put on alumina balls (3 mm in diameter) in an alumina crucible and exposed in the air at the investigated conditions. Oxidized samples were then cross-sectioned and polished with 2 µm-diamond particle slurry. Oxidation evolution of heat-treated samples was evaluated via the growth rate of oxidized zone observed on cross-sectioned surface by SEM. Analysis of tested specimens is conducted with phase identification by using XRD; microstructure observation by SEM and electron probe microanalysis (EPMA).

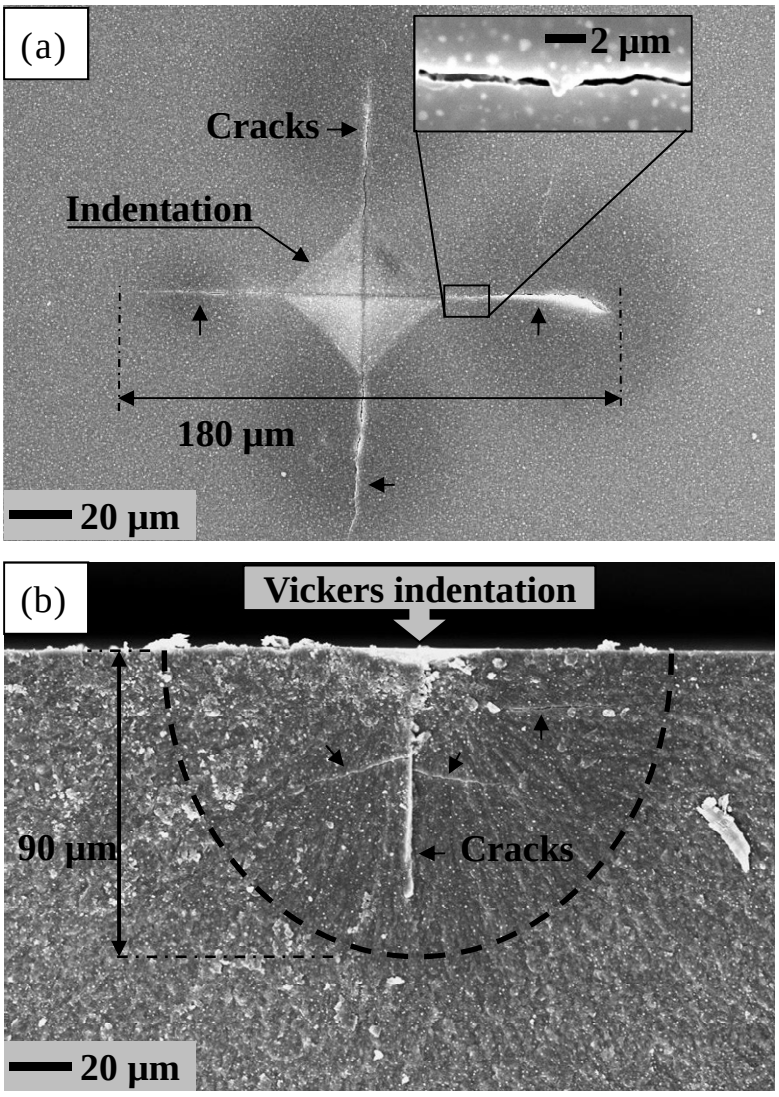

Fig. 5.2 SEM image shows the pre-cracks induced by Vickers indentations from the top view (a) and the cross-sectional view (b) of an as-cracked sample.

5.3 Results and discussion.

5.3.1 Mechanical properties.

Table 1 shows mechanical properties of 5 vol% Ni/mullite composite and monolithic mullite evaluated at room temperature. At a loading of 49 N, the average length of the diagonal left by the pyramidal diamond indenter was approximately 85μm. Vickers hardness (H_v) of 5Ni/mullite was measured to be 12.46±0.15 GPa. Fracture toughness (K_{IC}) of the composite calculated by applying Niihara's equation [77] was 2.85±0.26 $MPam^{1/2}$. By three-point bending tests conducted at room temperature, the Ni/mullite composites achieved 405±115 MPa in bending strength. The mechanical properties of monolithic mullite are also shown in Table 1.

Table 5.1 Mechanical properties of 5 vol% Ni/Mullite and monolithic mullite evaluated at room temperature.

Sample	*R.D.*/ %	*Grain Size*/ μm	H_v/ GPa	K_{IC}/ $MPam^{1/2}$	σ_b/ MPa
5Ni/mullite	99.6	~2	12.46±0.15	2.85±0.26	405±115
Mullite	99.2	~2	12.3±0.1	2.5±0.2	-

As shown in Table 1, the hardness and fracture toughness of 5 vol% Ni/mullite are comparable with that of monolithic mullite. Dispersion of Ni in mullite matrix did not give effect to their mechanical strength. This is attributed to low interface energy between Ni particles and the matrix. If the interface energy is lower than the transgranular fracture energy, the fracture mode would be the intergranular one. As shown in Fig. 5.1, the cavities which are the same in size with that of Ni particles appeared on the fractured surface due to the intergranular fracture mechanism (Fig. 3.10). The fracture propagated along the interface between Ni particles and the matrix that resulted in the appearance of the cavities. Similar behavior has been reported in Ni/Al_2O_3 system by Tuan *et al.* [85]. The intergranular fracture implies that the dispersion of Ni in Al_2O_3 matrix gives less effect on improvement of mechanical properties. This behavior is different with the fracture mechanism of SiC/Al_2O_3. The interface energy between SiC

and Al_2O_3 matrix is higher than the transgranular fracture energy that causes their fracture obeys the transgranular fracture mechanism [86].

5.3.2 Surface crack-disappearance.

Figure 5.3 presents SEM images of the introduced cracks on sample surface before and after heat-treatment at various conditions. The dashed lines indicate the edges of Vickers indentations. From each corner of the Vickers indentation, a crack with 50 μm in length propagated as observed in Fig. 5.3(a). After heat-treatment at 1000ºC for 6 h in the air, the surface cracks partially disappeared as the fraction of crack-disappearance was determined to be 35%. As shown in Fig. 5.3 (b), the grains like oxidation products formed on the sample surface. With heat-treatment at 1000ºC for 24 h in the air, surface cracks still partially disappeared as the fraction of crack disappearance was determined to be 85%. Fig. 5.3(c) shows the cracks completely disappeared after heat-treatment at 1100ºC for 6 h in the air. The cracks were totally filled up with the oxidation products that formed by the oxidation of Ni particles. For this reason, the as-healed samples were prepared by heat-treatment of as-cracked samples at 1100ºC for 6 h in the air. Heat-treatment at the same condition but in the Ar-1%H_2 flow which is the reduction environment of Ni particles did not show any healing ability, as shown in Fig. 5.3(d). Results of surface crack-disappearance are plotted in Fig. 5.4.

Figure 5.5 shows XRD patterns for phase identification of the exposed surface before and after heat-treatment at various conditions. Two dominant compounds which are Ni and mullite ($3Al_2O_3.2SiO_2$) were detected in as-sintered one. Only NiO phase appeared after heat-treatment at 1000 and 1100ºC for 6 h in the air. Because of the reduction environment of Ni metal, the NiO phase did not appear after heat-treatment at 1100ºC for 6 h in the Ar-1%H_2 gas mixture.

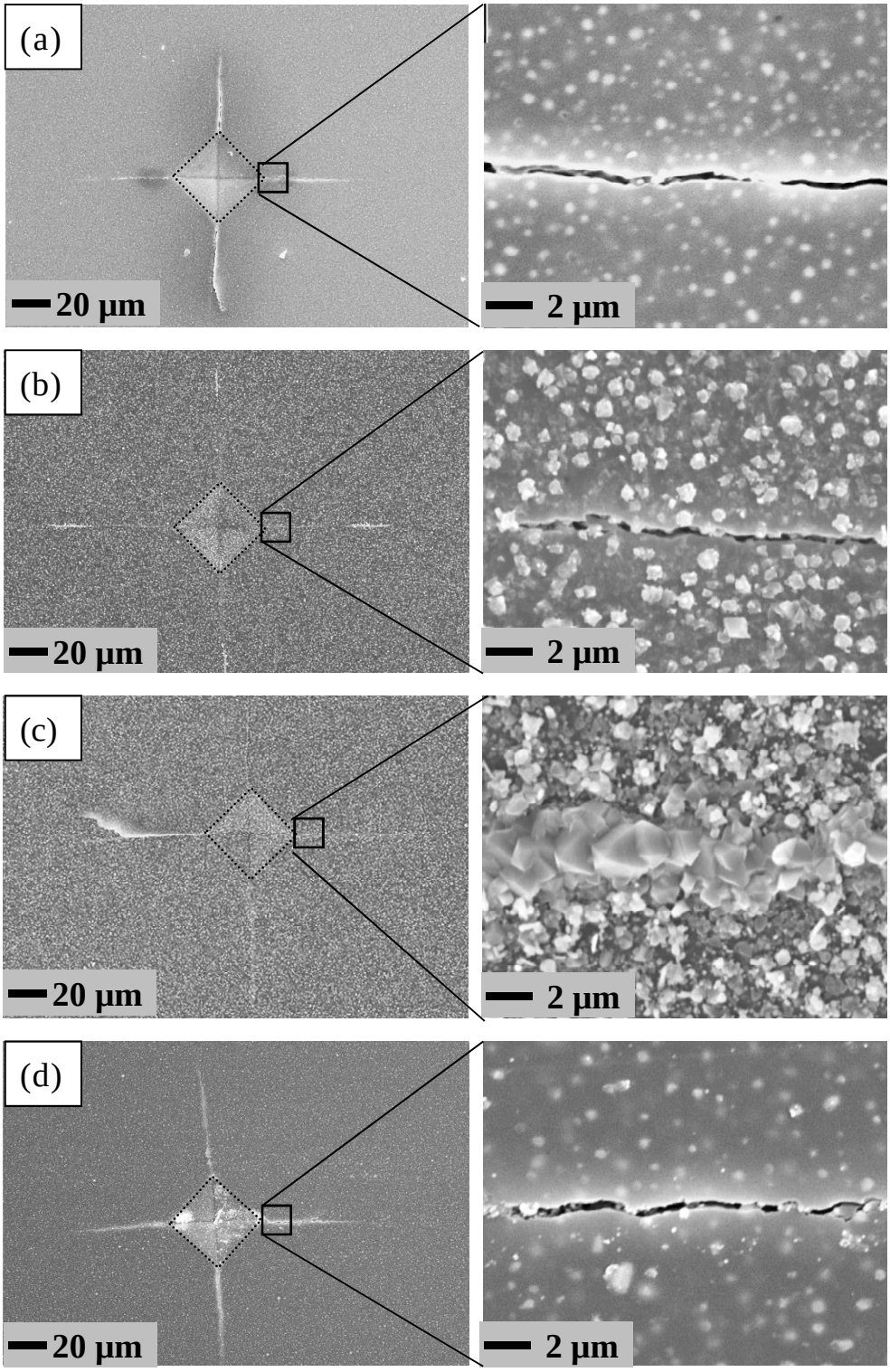

Fig. 5.3. SEM images of surfaces of as-cracked sample (a) and samples heat-treated at 1000ºC for 6 h in air (b), 1100ºC for 6 h in air (c), 1100ºC for 6 h in Ar-1%H_2 gas flow (d).

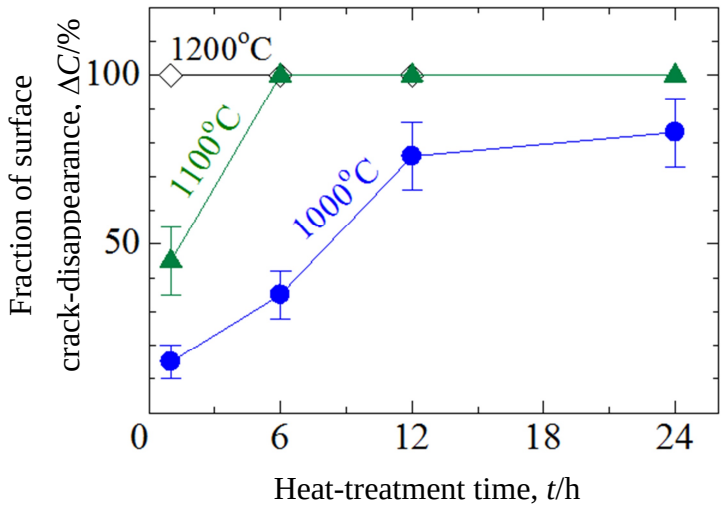

Fig. 5.4 The fraction of surface crack-disappearance as a function of heat-treatment time at various heat-treatment temperatures.

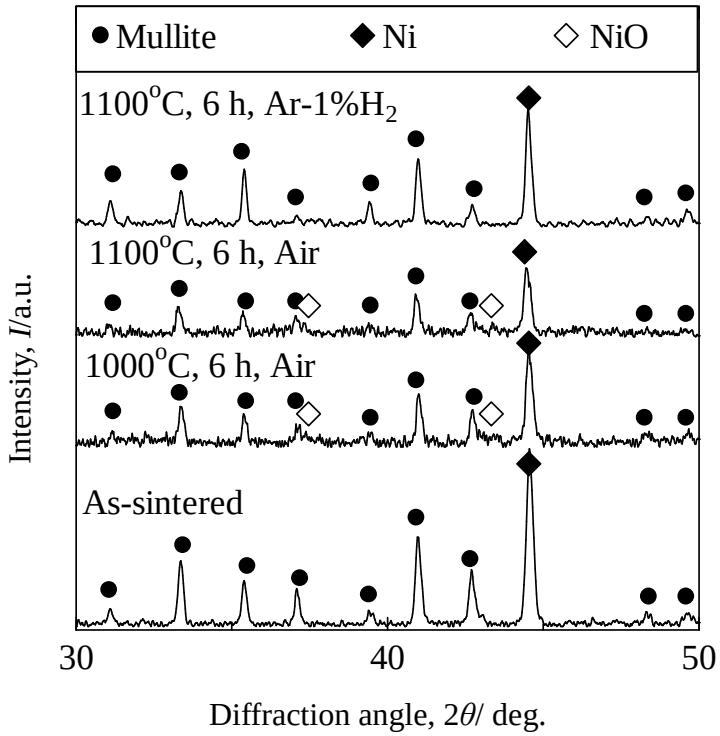

Fig. 5.5 XRD patterns obtained from the sample surface before and after heat-treatment at various conditions.

Figure 5.6 shows the fraction of surface crack disappearance as a function of heat-treatment temperatures for 5Ni/mullite with the previously reported results on 5Ni/(10ZrO_2+Al_2O_3) (in Chapter 4) and 5Ni/Al_2O_3 (in Chapter 3). The Ni/mullite

requires a lower heat-treatment temperature for surface crack-disappearance than the others nanocomposites. For example, Ni/mullite requires a heat-treatment at 1100ºC for 6 h to have a complete crack-disappearance. While heat-treatment at the same condition, Ni/(ZrO_2+Al_2O_3) and Ni/Al_2O_3 only achieved 65% and 45% of the fraction of crack-disappearance, respectively. This phenomenon is caused by the difference of outward Ni^{2+} diffusion in various matrices. Diffusion of Ni^{2+} is more active in mullite matrix than that in Al_2O_3 and (ZrO_2+Al_2O_3) matrices. Fig. 5.7 shows the cross-sectional view of a sample after heat-treatment at 1200ºC for 48 h in the air. The oxidation of Ni at high temperatures induced the diffusion of ions and cations. The diffusions created an oxidation product layer as well as the oxidized zone where metallic Ni particles no longer existed. With heat-treatment at the same condition, the oxidation products layer formed in Ni/mullite system was thicker than that formed in Ni/Al_2O_3. While the thickness of oxidized zone formed in Ni/mullite was less than that formed in Ni/Al_2O_3 system. In other words, the diffusion rate of Ni^{2+} in Ni/mullite was faster than that in Ni/Al_2O_3. In contrast, diffusion rate of O^{2-} in Ni/mullite was much slower than that in Ni/Al_2O_3.

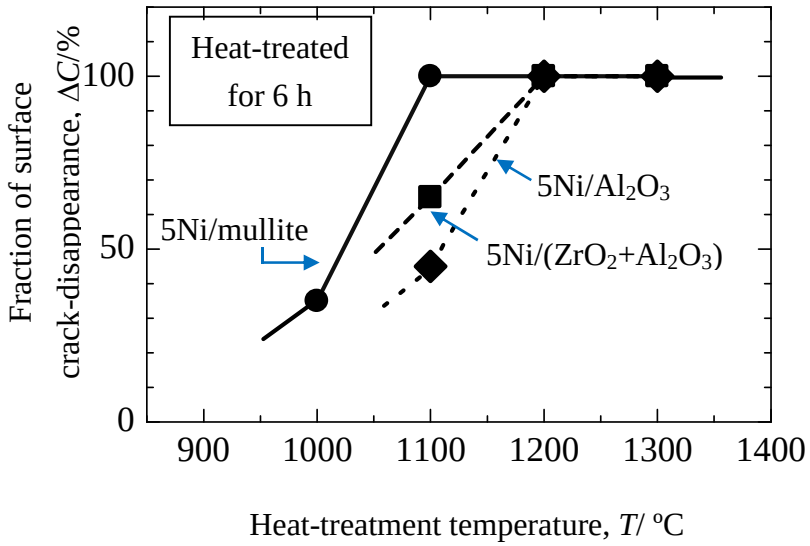

Fig. 5.6 The fraction of surface crack-disappearance as a function of heat-treatment temperature for 5Ni/mullite, 5Ni/(ZrO_2+Al_2O_3) and 5Ni/Al_2O_3.

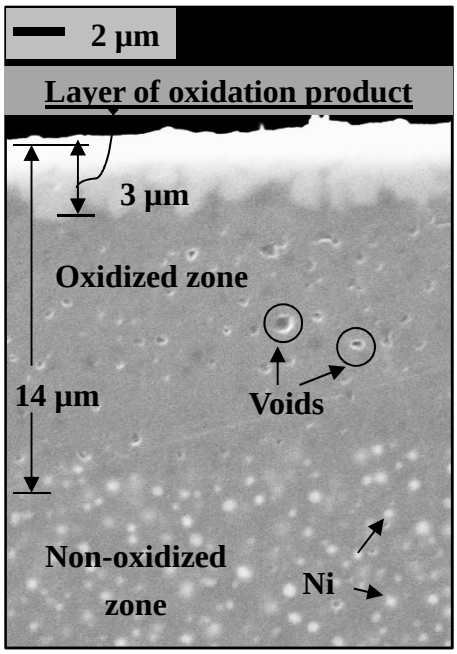

Fig. 5.7 The cross-sectional view of 5Ni/mullite heat-treated at 1200ºC for 48 h in air. Nickel particles are visible as the bright dots, existing at the non-oxidized zone. The voids in the oxidized zone are developed by the outward diffusion Ni^{2+}.

5.3.3 Strength recovery induced by self-healing.

Figure 5.8 shows the bending strength of as-sintered samples and samples heat-treated at various conditions. The as-sintered samples achieved 405±115 MPa in bending strength. With three Vickers indentations introduced on the tensile surface, bending strength of as-cracked samples was only 113±10 MPa. By heat-treatment at 1100ºC for 6 h in air, the as-healed samples exhibited a bending strength of 434±60 MPa which is comparable with that of as-sintered samples. The samples heat-treated in the Ar-1%H_2 gas mixture at 1100ºC for 6 h did not show any strength recovery as their bending strength only achieved 126±8 MPa.

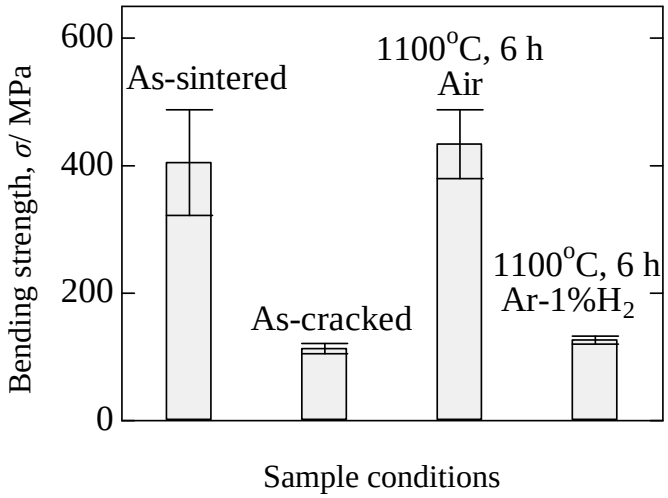

Fig. 5.8 Bending strength of as-sintered samples, as-cracked samples, samples heat-treated at 1100ºC for 6 h in air and samples heat-treated at 1100ºC for 6 h in Ar-1%H_2.

Figure 5.9 shows the fractures of samples by bending tests conducted for as-cracked, as-healed and sample heat-treated in the Ar-1%H_2 gas mixture. Fig. 5.9(a) shows the fracture of as-cracked sample propagated across all the Vickers indentations as they were the highest concentration points. The bending strength of as-cracked samples increased from 113 MPa to 443 MPa by heat-treatment at 1100ºC for 6 h in air. The value after the heat-treatment is comparable with that of as-sintered samples and indicates the full recovery of bending strength by the heat-treatment. The recovery of bending strength was caused by the crack-disappearance after heat-treatment. Fig. 5.10 shows the cross-sectional view of cracks after heat-treatment at 1100ºC for 6 h in air. It means that all of the cracks were not only healed from the top view but also from the cross-sectional view. As the cracks completely disappeared, the fracture of as-healed samples did not propagate across the Vickers indentations, as shown in Fig. 5.9(b). They were no longer the highest stress concentration points. Cracks did not disappear after heat-treatment in Ar-1%H_2 at 1100ºC for 6 h. As a result, the fracture of samples heat-treated at this condition propagated across all the three Vickers indentations, as shown in Fig. 5.9(c). They did not show any recovery in strength as their values of bending strength were as same as that of as-cracked samples. In other words, the recovery of bending strength was caused by the self-healing mechanism which was originated from the oxidation of Ni

particles at high temperatures.

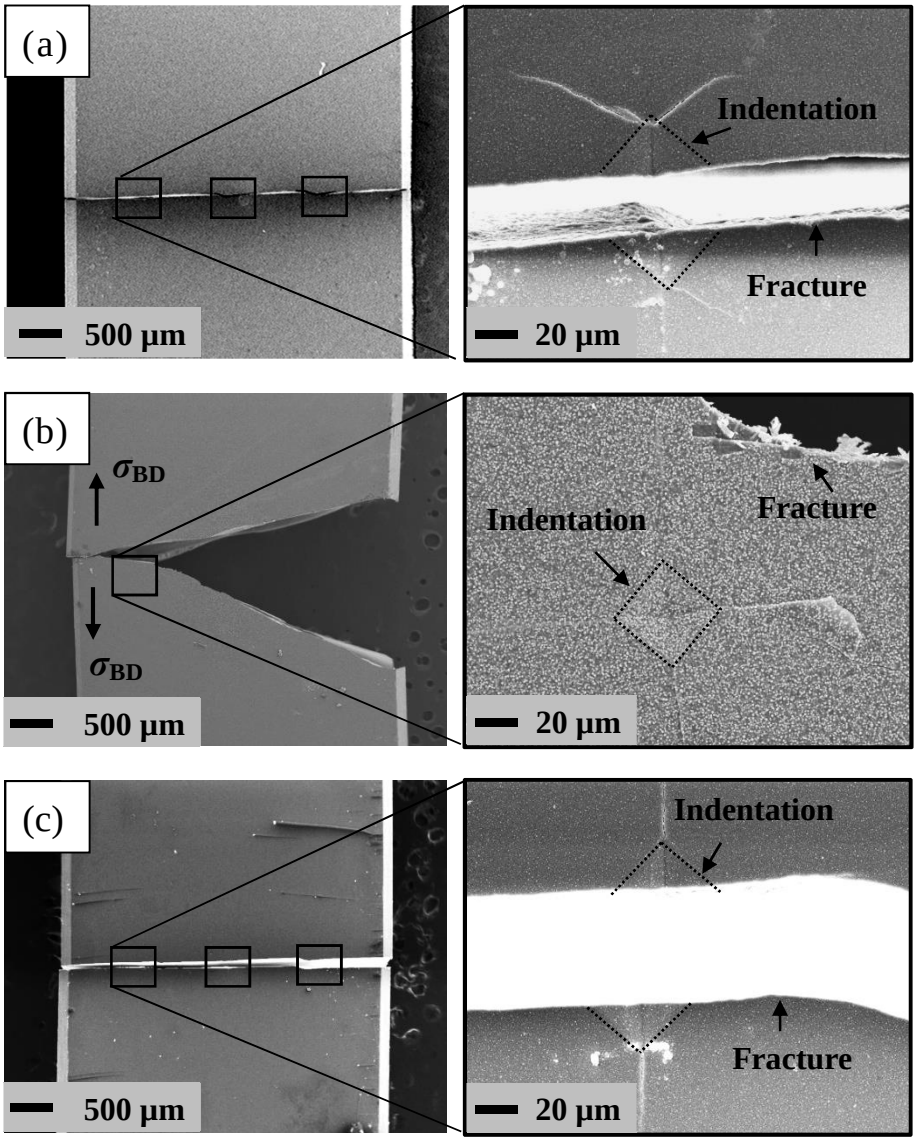

Fig. 5.9 SEM images show the fractures of samples by bending tests conducted for as-cracked (a), as-healed sample (heat-treated at 1100ºC for 6 h in air) (b) and sample heat-treated at 1100ºC for 6 h in Ar-1%H_2 gas mixture (c). The σ_{BD} indicates the orientations of stresses applied on the Vickers indentations by bending tests.

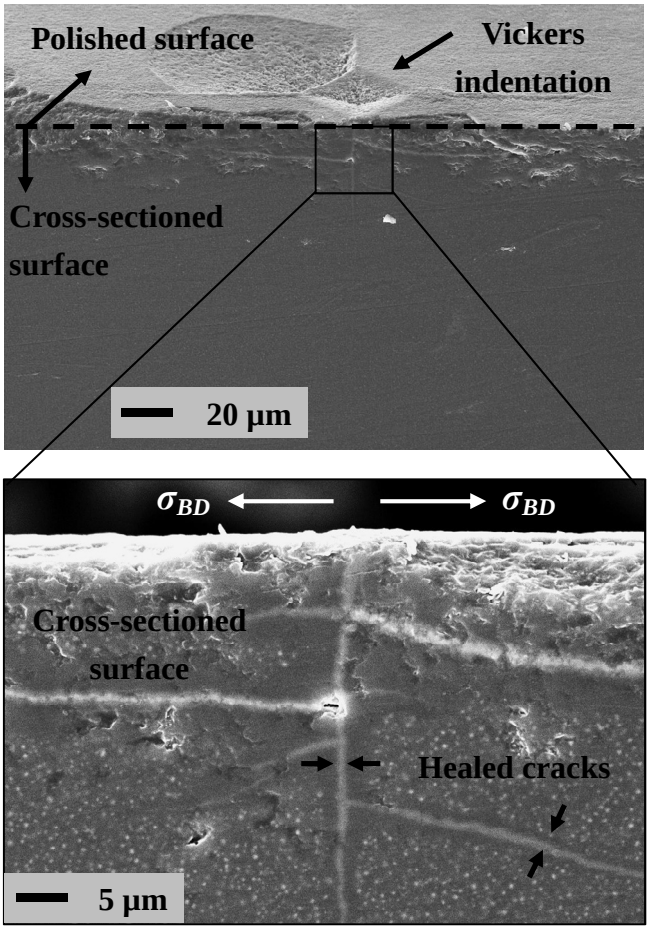

Fig. 5.10 SEM images show the cross-sectional view of the cracks after heat-treatment at 1100ºC for 6 h in air.

5.3.4 Oxidation resistance.

Oxidation tests were conducted at temperature range of 1200-1400ºC for 1-48 h to study the oxidation behavior as well as self-healing mechanism of Ni/mullite composites. Fig. 5.11 shows SEM images observed on cross-sectioned surface of Ni/mullite samples after oxidations at 1200ºC for various oxidation times. The surface layer is visible as the bright layer with the *y* thickness. Below the surface layer is the oxidized zone, in which, Ni particles oxidized and mostly outward diffused to the surface layer. The thickness of oxidized zone, *x*, was determined. Ni particles are visible as bright contrast dots in the region following the oxidized zone. The region containing Ni particles was thus considered as the non-oxidized zone. Fig. 5.12 shows the SEM images observed on the

cross-sectioned surface of Ni/mullite samples after oxidations at 1300ºC for various oxidation times. Oxidation behavior of Ni/mullite at 1300ºC for less than 6 h was similar with that oxidized at 1200ºC. Fig. 5.12(a) and (b) shows the surface seems to be composed by a single phase. Fig. 5.12(c) and (d) show composition of surface layer which includes dark contrast and bright contrast phases. Fig. 5.13 shows the cross-sectioned surfaces of samples oxidized at 1400ºC where the contrast can be easy noticed.

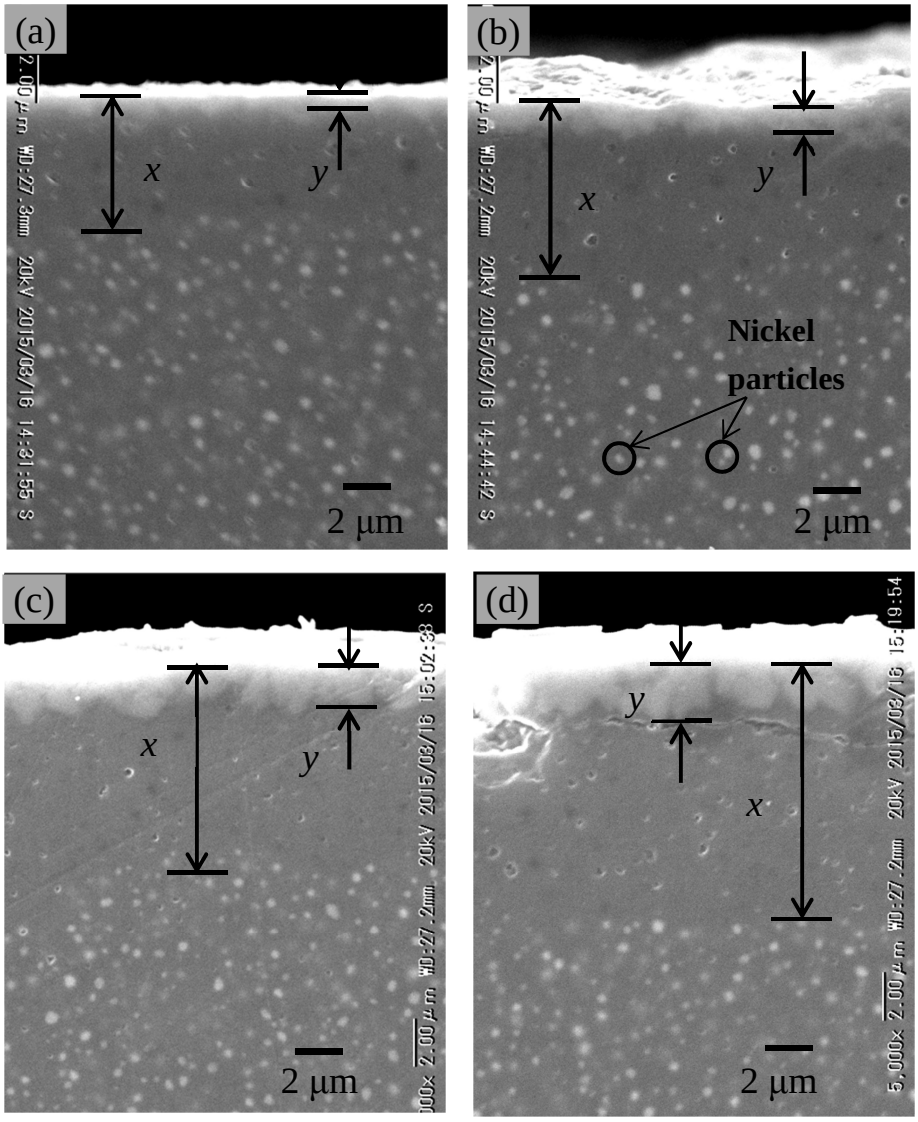

Fig. 5.11 SEM images show the cross-sectioned surfaces of Ni/mullite specimens after oxidation at 1200ºC for (a) 6 h, (b) 12 h, (c) 24 h and (d) 48 h.

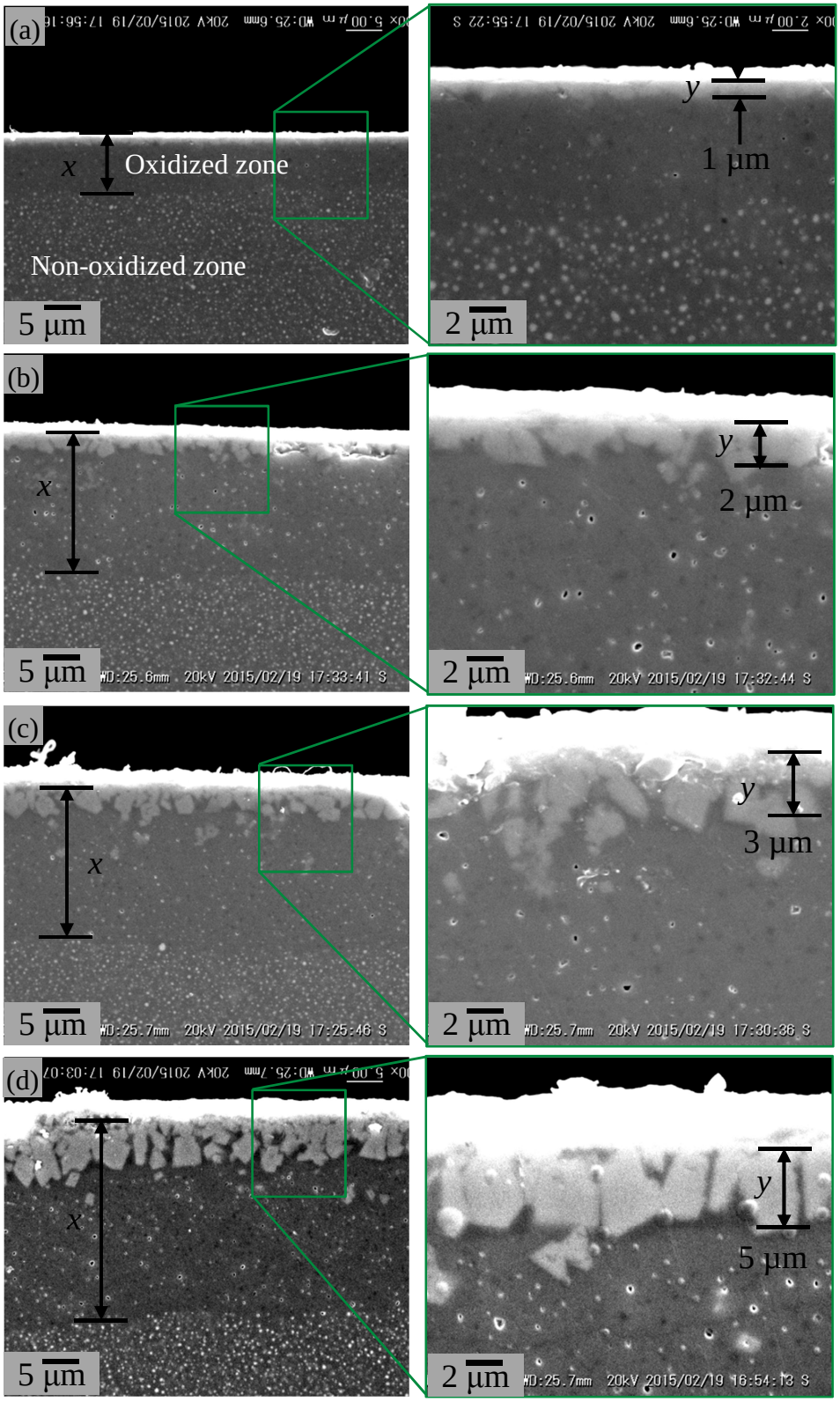

Fig. 5.12 SEM images show the cross-sectioned surfaces of Ni/mullite specimens after oxidation at 1300ºC for (a) 1 h, (b) 6 h, (c) 12 h and (d) 24 h.

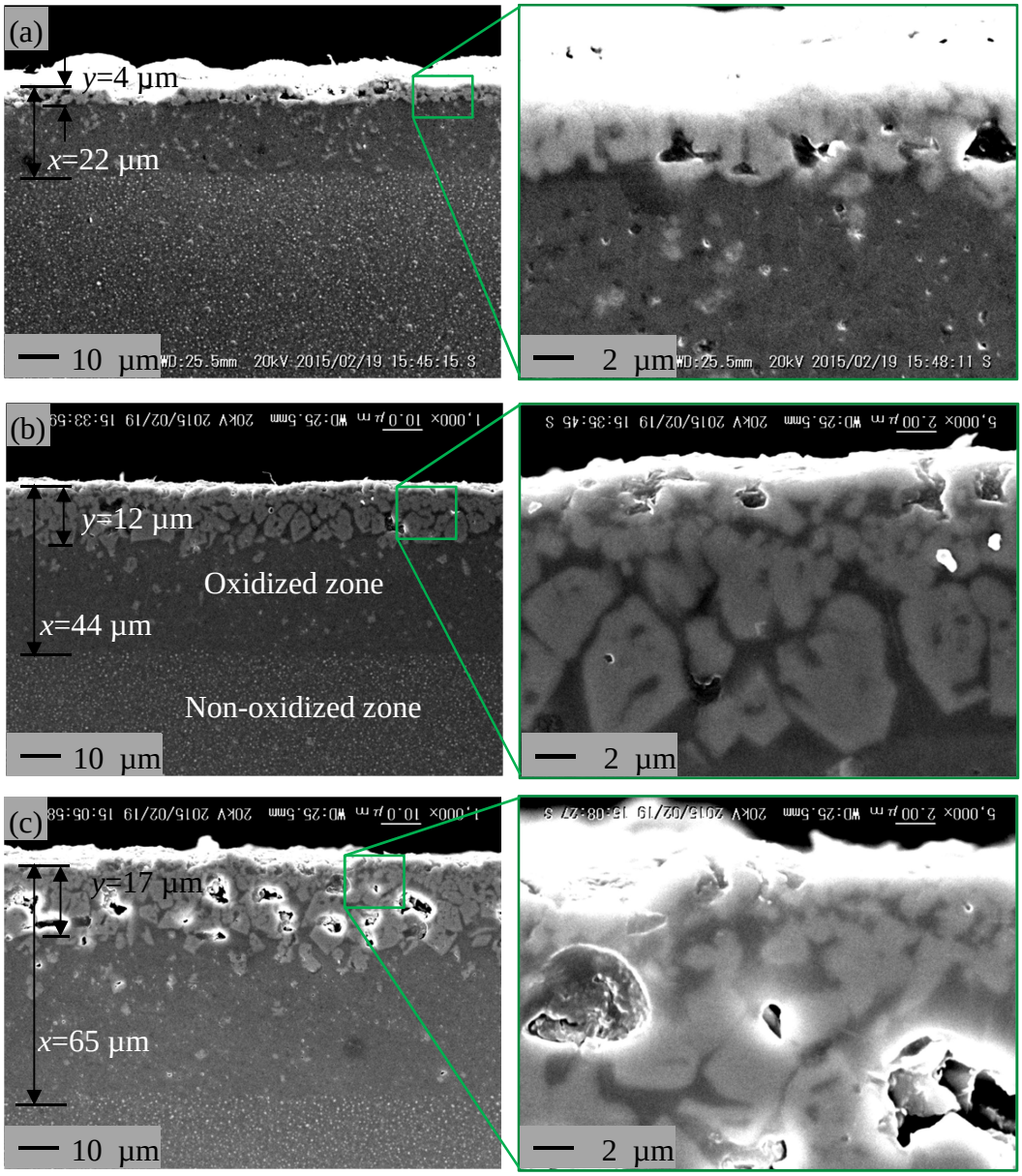

Fig. 5.13 SEM images show the cross-sectioned surfaces of Ni/mullite specimens after oxidation at 1400ºC for (a) 1 h, (b) 6 h, and (c) 12 h.

Figure 5.14 shows XRD patterns obtained from the samples before/after oxidations at 1300ºC for various oxidation times. As-sintered sample contained only Ni and mullite phase as the two dominant phases were detected. NiO phase formed significantly after oxidation at 1300ºC for 1 h. Some weak signals from spinel phase were also detected. XRD patterns of samples after oxidations at 1300ºC for 6-24 h present the significant oxidation products formed on sample surface which are NiO and the spinel. Since the

$NiAl_2O_4$ and Ni_2SiO_4 spinels have the same structure, it is not clear to determine the oxidation products. Fig. 5.15 shows XRD patterns of samples oxidized at 1400ºC for 1-12 h. Ni/mullite sample oxidized at 1400ºC for 1 h containing NiO and the spinel as similar as that of samples oxidized at 1300ºC. For longer time, signals of NiO phase gradually lessen and disappear. For example, phase composition on surface of sample oxidized at 1400ºC for 12 h was mainly the spinels.

Figure 5.16 plotted the thickness of oxidized zone as a function of oxidation time. With increasing oxidation time, the thickness of oxidized zone increased. The growth of oxidized zone obeyed the parabolic law. Fig. 5.17 shows the parabolic rate constant, k_p, of Ni/mullite as a function of reciprocal oxidation temperature. The value of apparent activation energy for the growth rate of oxidized zone in Ni/mullite was calculated to be 462 $kJmol^{-1}$. As shown in Fig. 5.17, the oxidation rate of Ni/mullite is one order of magnitude less than that of Ni/Al_2O_3 nanocomposites and two order of magnitude less than that of $Ni/(YZ+Al_2O_3)$ nanocomposites.

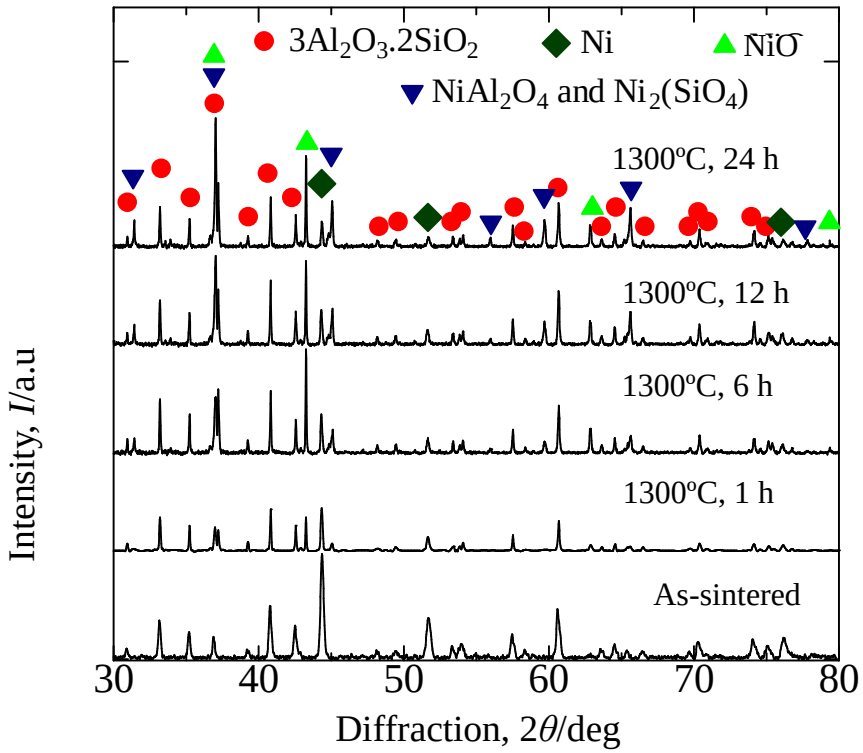

Fig. 5.14 XRD patterns obtained from the sample surface before and after oxidations at 1300ºC for various condition durations.

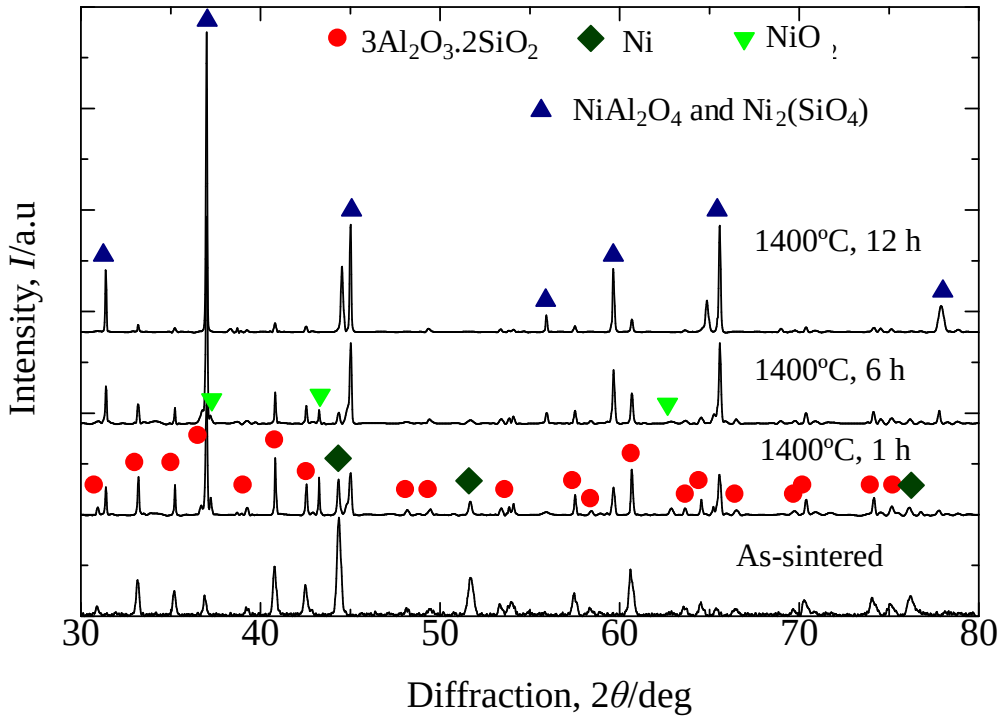

Fig. 5.15 XRD patterns obtained from the sample surface before and after oxidations at 1400ºC for various condition durations.

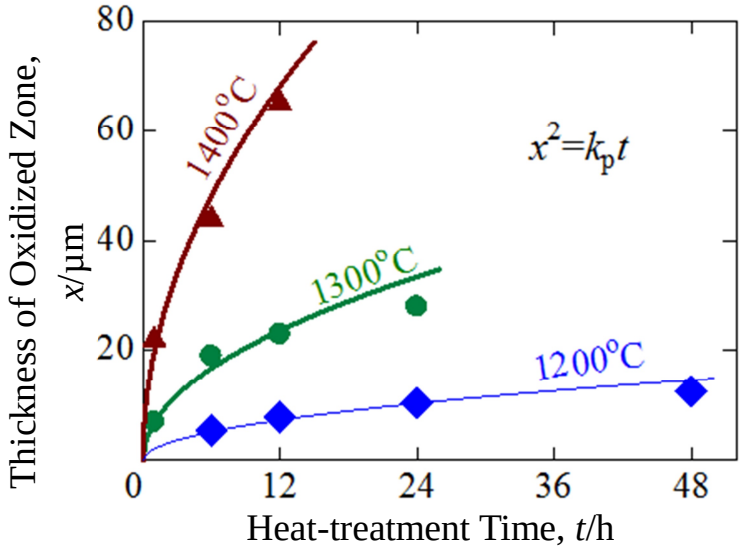

Fig. 5.16 Thickness of oxidized zone as a function of oxidation time at various temperatures for Ni/mullite composites.

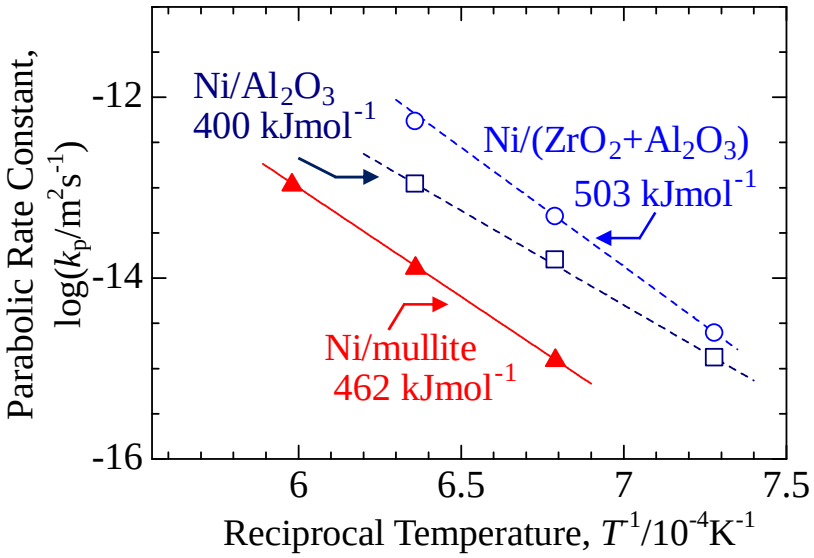

Fig. 5.17 Temperature dependence of parabolic rate constant on oxidation of Ni/mullite, Ni/Al_2O_3 and $Ni/(YZ+Al_2O_3)$systems.

Figure 5.18 shows the SEM images observed on fractured surface of Ni/mullite sample after oxidation at 1400ºC for 12 h. Microstructure of the top layer (Fig. 5.18a) was apparently different with that of the oxidized zone. It implies the surface layer is composed of oxidation products only. Fig. 5.19 shows the EPMA images to determine the composition of the surface layer. The arrows in Fig. 5.19(b) indicate the two distinct phases on the surface layer as mentioned in Fig. 5. 13(b) and (c). With the same positions, these arrows indicated the two distinct phases were $NiAl_2O_4$ and Ni_2SiO_4 as shown in Fig. 5.19 (c) and (d). Fig. 5.19(e) presents the existence of mullite matrix in the region below the surface layer. Whereas, Fig. 5.19(f) shows the Ni element mapping in which Ni element mostly located at the surface layer. For the reasons above, the surface layer is attributed to the composition of $NiAl_2O_4$ and Ni_2SiO_4 when Ni/mullite oxidized at 1400ºC for 12 h (Fig.5.20).

The results of oxidation investigation for Ni/mullite indicated the composition of the surface layer is varied when the oxidation condition is differed. The composition of the surface layer at various oxidation conditions is summarized in Table 5.2.

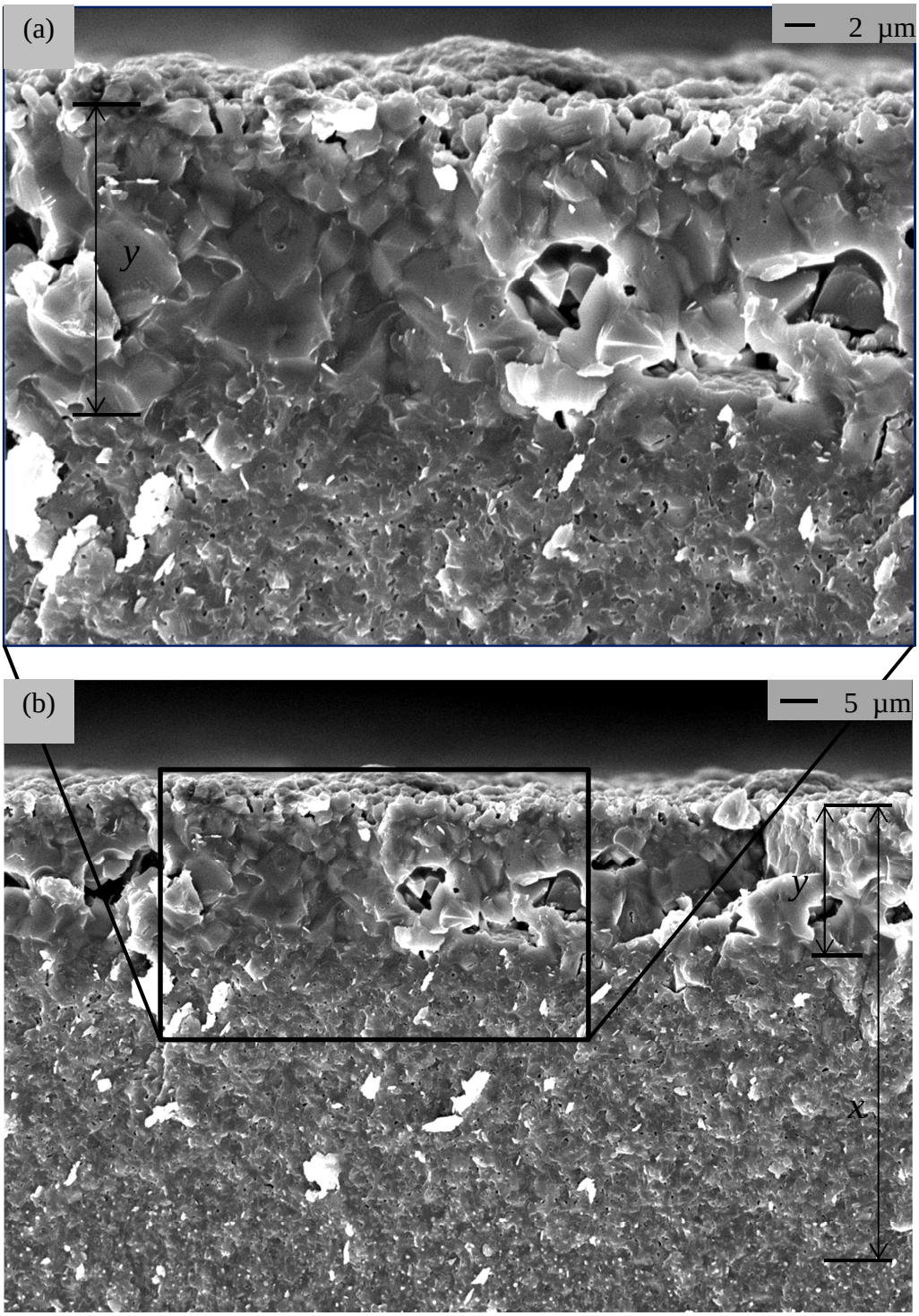

Fig. 5.18 SEM images show the fractured surface of Ni/mullite specimen oxidized at 1400ºC for 12 h. The microstructure of the surface layer is obviously different with the oxidized zone.

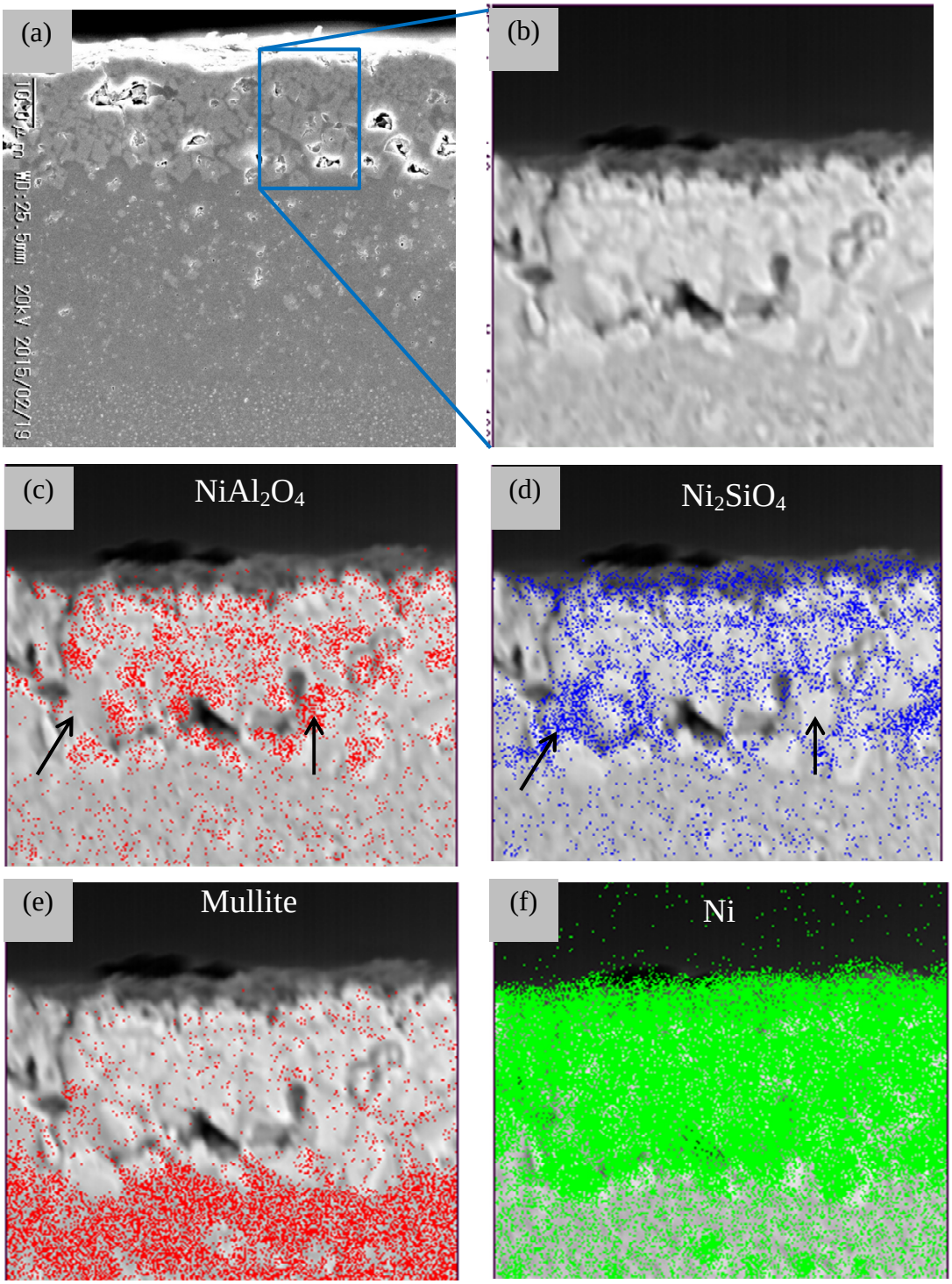

Fig. 5.19 EPMA images show the phase-patched map at (a-b) surface layer for (c) Ni-Al-O, (d) Ni-Si-O, (e) Al-Si-O and (f) Ni-element distribution of Ni/mullite specimen oxidized at 1400ºC for 12 h.

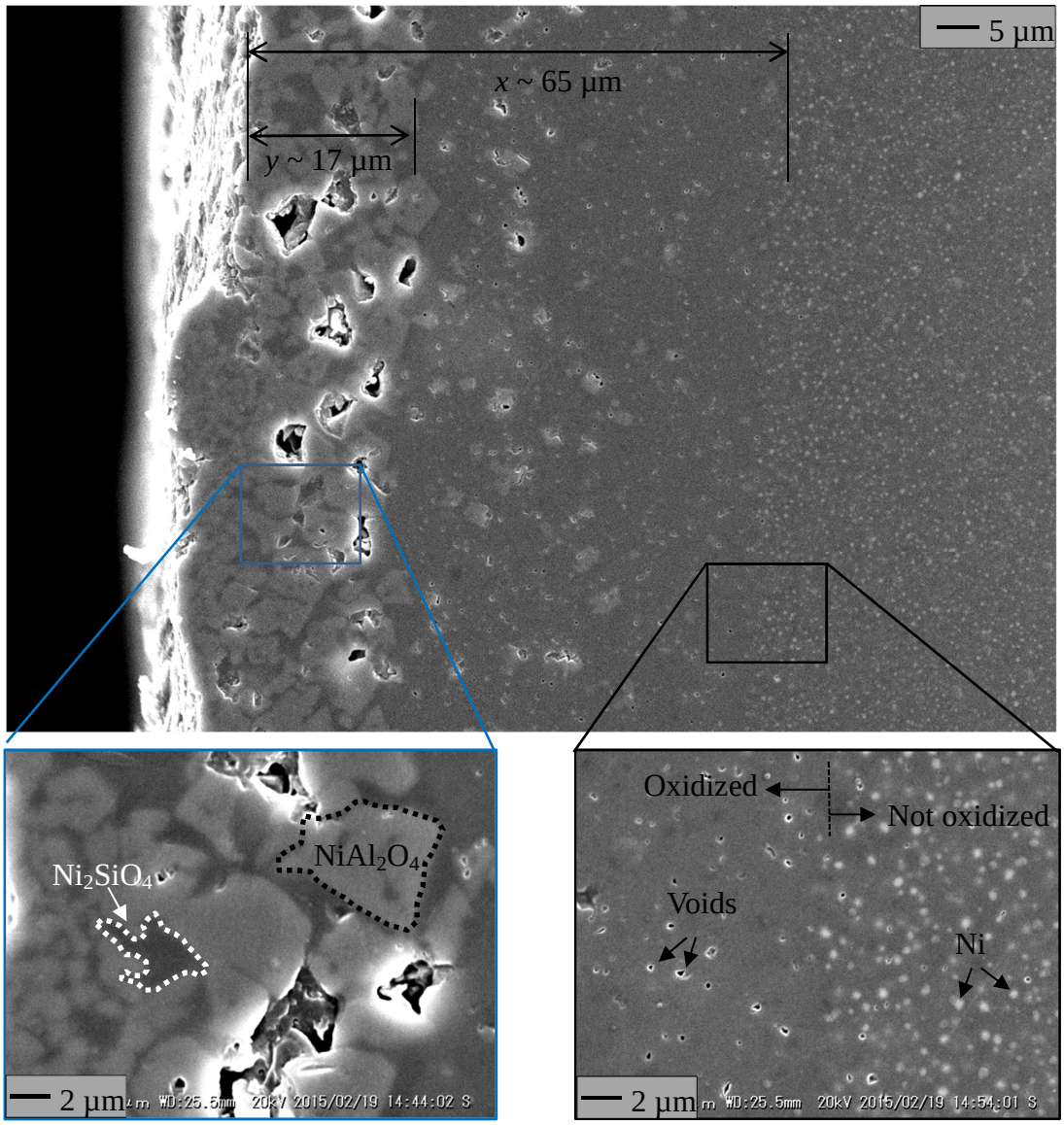

Fig. 5.20 SEM images observed on (a) the cross-sectioned surface of Ni/mullite specimen oxidized at 1400ºC for 12 h, showing the composition of (b) surface layer and (c) the border between oxidized zone and non-oxidized zone.

Table 5.2 Composition of the surface layer formed on Ni/mullite samples at various oxidation conditions.

Oxidation conditions		Composition
1200ºC, up to 48 h		NiO (dominant) and Spinel
1300ºC, up to 24 h		NiO and Spinel
1400ºC	1~6 h	NiO and Spinel
	> 12 h	Spinels

5.4 Conclusions.

Fully-densified mullite nanocomposites with 5 vol% nano-Ni dispersion are fabricated by pulsed electric current sintering technique to investigate their self-healing function. The investigation on self-healing is conducted at the temperature ranging from 1000 to 1200ºC for 1-24 h in the air. Ni/mullite composite requires lower heat treatment conditions to have self-healing function than the other composites such as Ni/Al_2O_3, Ni/(ZrO_2+Al_2O_3). Ni/mullite composites also have a greater oxidation resistance than Ni/Al_2O_3 and Ni/(ZrO_2+Al_2O_3) nanocomposites. The following conclusions are based on the mechanical properties, surface crack-disappearance by thermal oxidation, self-healing-induced strength recovery and oxidation resistance of Ni/mullite composites.

1. Mechanical properties.

Some basic information on mechanical properties of fabricated Ni/mullite composites are provided. Hardness, fracture toughness and bending strength of the composites were determined to be 12.46 GPa and 2.85 $MPam^{1/2}$, 405 MPa respectively. Investigation on mechanical properties on monolithic mullite indicated that dispersion of Ni in mullite matrix did not give effect to their hardness and fracture toughness. Observation on microstructure of Ni/mullite suggests the toughening mechanism in Ni/mullite system may follow the intergranular fracture mechanism.

2. Surface crack-disappearance via thermal oxidation.

The surface crack-disappearance in Ni/mullite system can be achieved by heat-treatments in the air at temperatures ranging from 1000 to 1300ºC. For example, surface cracks with a total length of 180 μm completely disappeared by heat-treatment at 1100ºC for 6 h in air. By heat-treatment in Ar-1%H_2 gas mixture at 1100ºC for 6 h, surface cracks on Ni/mullite samples did not disappear. It clarifies the self-healing mechanism of Ni/mullite is caused by oxidation of Ni phase within the mullite matrix.

3. Self-healing-induced strength recovery.

Three-point bending tests were conducted at room temperature for as-sintered, as-cracked and as-healed samples to estimate the effectiveness of self-healing on strength recovery. As the surface cracks completely disappeared by heat-treatment at 1100ºC for 6 h in the air, the bending strength of as-healed samples recovered from 113 MPa (as-cracked ones) to 434 MPa which is comparable with that of as-sintered samples (405 MPa). As-cracked samples heat-treated in Ar-1%H_2 gas mixture at 1100ºC for 6 h did not show the strength recovery, as they only achieved 125 MPa in bending strength.

4. Oxidation resistance.

Investigation for oxidation behavior of Ni/mullite composites was conducted at temperatures ranging from 1200~1400ºC for 1~48 h. Oxidation resistance of Ni/mullite composites was examined through the growth rate of oxidized zone after heat-treatments in air. Oxidation of Ni phase within mullite matrix creates the formation of a surface layer and the oxidized zone. The growth of oxidized zone and the surface layer obeyed the parabolic law. The apparent activation energy for the growth of oxidized zone was determined to be 462 $kJmol^{-1}$. Oxidation rate of Ni/mullite is one order of magnitude less than that of Ni/Al_2O_3. The composition of the surface layer was determined to be mainly NiO at temperatures below 1300ºC. Above 1400ºC, the surface layer is composed of $NiAl_2O_4$ and Ni_2SiO_4 spinels. Formation mechanism of the surface layer was attributed to a combination of internal and external oxidations.

Chapter VI
Conclusions and Suggestions for Future Works

6.1 Conclusions.

The overall aim of the present dissertation is to develop self-healing ceramics for high temperature applications. Self-healing functions of Ni/Al_2O_3, Ni/(ZrO_2+Al_2O_3) and Ni/mullite nanocomposites were investigated and discussed from the kinetic point of view. Ni/Al_2O_3 nanocomposites exhibit a great self-healing performance at high temperatures caused by the oxidation of Ni particles. Ni/Al_2O_3 nanocomposites could be suitable for the components in hot sections of gas turbine engines. However, high-temperature strength of Ni/Al_2O_3 nanocomposites must be improved. Dispersion of YZ is one of the solutions for high-temperature strength of Ni/Al_2O_3 nanocomposites. YZ dispersion does not influence significantly on self-healing performance. Nevertheless, YZ accelerates the oxidation rate of the composites. For further studies, the oxidation resistance of Ni/(YZ+Al_2O_3) could be improved by dopants of silicon carbide (SiC), silicon (Si) or yttrium (Y). Ni/mullite nanocomposites possess the best self-healing performance among the investigated composites. With a great oxidation resistance and excellent self-healing performance, Ni/mullite nanocomposites are potential for high-temperature applications. For further applications, mechanical properties of Ni/mullite must be improved. The main conclusions are summarized as follows:

6.1.1 Self-healing function of Ni/Al_2O_3 nanocomposites.

Nickel dispersed Al_2O_3 nanocomposites have attracted much interest because of excellent self-healing function and magnetic properties. Unlike the volume expansion-induced self-healing of SiC dispersed ceramic-based composites, active diffusion of Ni^{2+} along the Al_2O_3 grain boundaries creates a surface layer composed of $NiAl_2O_4$-the oxidation product which induces the self-healing function of Ni/Al_2O_3. With the diffusion mechanism, self-healing of Ni/Al_2O_3 is expected to achieve repeatedly. Moreover, it is expected to extend their service life and increase reliability. For the

reasons above, self-healing function of 5 vol% Ni dispersed Al_2O_3 nanocomposites was investigated via the major characteristics such as surface crack-disappearance, strength recovery and oxidation resistance.

The surface crack-disappearance was investigated at temperatures ranging from 1100-1300ºC for 1-24 h in the air. The surface cracks with approximately 200 μm in length introduced by Vickers indentions completely disappeared after heat-treatments at 1200ºC for 6 h or 1300ºC for 1 h in the air. The self-healing mechanism was clarified to be the oxidation of Ni phase which induced the formation of the $NiAl_2O_4$ surface layer. In comparison with the self-healing of SiC/Al_2O_3, the volume expansion factor (ϕ) of Ni/Al_2O_3 was 1.2 times, smaller than that of SiC/Al_2O_3 (ϕ=2 times). However, the surface crack-disappearance of Ni/Al_2O_3 with diffusion mechanism requires lower heat-treatment conditions than that of SiC/Al_2O_3.

Investigation of strength recovery obtained by the self-healing effects was conducted by three-point bending tests at 25-1200ºC for as-sintered, as-cracked and as-healed samples. The as-sintered samples achieved approximately 1000 MPa in bending strength at room temperature, 400 MPa at 1000ºC and 200 MPa at 1200ºC. The degradation of high-temperature strength of the composites was attributed to the intergranular fracture mechanism of Ni/Al_2O_3 and the mismatch stress caused by the difference in thermal expansion between dispersoids and matrix. Due to the low interfacial energy, dispersion of Ni exhibits poor effects on inhibition of grain boundary sliding. As-cracked samples with introduced Vickers indentations obtained only 120 MPa at room temperature and 130 MPa at 1200ºC. By heat-treatment at 1200ºC for 6 h in the air before the bending tests, as-healed samples exhibited the bending strength values which are comparable with that of as-sintered samples regardless of the bending test temperatures. Results of the investigation indicated the self-healing function of Ni/Al_2O_3 is available at high temperatures as well as room temperature.

Oxidation resistance of Ni/Al_2O_3 was investigated at temperature ranging from 1100-1300ºC for 1-48 h in the air to clarify the self-healing mechanism, as well as the development of oxidized zone. The oxidation of Ni particles within Al_2O_3 matrix at high temperatures induced the outward diffusion of Ni^{2+} and inward diffusion of O^{2-}. The

outward diffusion of Ni^{2+} creates the surface layer which is responsible for the self-healing effectiveness. The inward diffusion of O^{2-} creates an oxidized zone composed of $NiAl_2O_4$ grains and Al_2O_3 matrix which may influence on self-healing effectiveness, as well as mechanical properties of the composites. From the results of this investigation, the growth of oxidized zone obeyed the parabolic law with the apparent activation energy of 400 $kJmol^{-1}$. Based on the investigation, an equation was established to describe the influence of Ni volume fraction and grain boundary diffusion as following:

$$X^2 = k_{gs} V_{Al_2O_3} \frac{D_{gb} C_o}{f_{V_{Ni}}} \ln\left(\frac{P_{O_2}^1}{P_{O_2}^2}\right) t;$$

where X is thickness of the oxidized zone; t Oxidation time; $f_{V_{Ni}}$ Volume fraction of Ni; $V_{Al_2O_3}$ Molar volume of the matrix; k_{gs} Grain size factor.

Since the diffusion path in Ni/Al_2O_3 system is attributed to the grain boundaries of the matrix, the grain size factor (k_{gs}) is taken into account. The k_{gs} is representative for the influence of Al_2O_3 grain sizes. As shown in the equation, the parabolic rate constant of the growth of oxidized zone is directly proportional with the grain size factor and inversely proportional with the volume fraction of Ni.

6.1.2 Self-healing function of Ni/(ZrO_2+Al_2O_3) nanocomposites.

The surface crack-disappearance obtained by heat-treatment in the air of $Ni/(YZ+Al_2O_3)$ was similar to that of Ni/Al_2O_3. According to the results of this investigation, $Ni/(YZ+Al_2O_3)$ showed slightly higher efficiency in surface crack-disappearance than Ni/Al_2O_3. For example, surface cracks on $Ni/(YZ+Al_2O_3)$ sample completely disappeared by heat-treatment at 1200ºC for 1 h in air. While surface cracks on Ni/Al_2O_3 sample only disappeared 80% by heat-treatment at the same conditions. Results of the investigation for high-temperature strength indicated the positive influence of YZ dispersion on the bending strength of the composites. The bending strength at 1200ºC of $Ni/(YZ+Al_2O_3)$ was 460 MPa which was higher than that of Ni/Al_2O_3 (200 MPa). Dispersion of YZ also increased the bending strength of as-healed samples which was even higher than that of as-sintered samples at high temperatures. Nonetheless, the oxidation resistance of $Ni/(YZ+Al_2O_3)$ was worse than that of Ni/Al_2O_3. The growth of

oxidized zone in Ni/(YZ+Al_2O_3) obeyed the parabolic law with the apparent activation energy of 503 $kJmol^{-1}$.

6.1.3 Self-healing function of Ni/mullite nanocomposites.

Fully-densified mullite nanocomposites with 5 vol% nano-Ni dispersion exhibit a greater self-healing performance than that of Ni/Al_2O_3 or Ni/(YZ+Al_2O_3) nanocomposites. Surface cracks with a total length of 180 μm completely disappeared by heat-treatment at 1100ºC for 6 h in the air. Bending strength of the as-cracked samples which were prepared with three Vickers indentations on the tensile surface only achieved 113 MPa. By the surface crack disappearance, as-healed samples exhibited a recovered bending strength of 434 MPa which was comparable with that of as-sintered samples (405 MPa). With heat-treatment in Ar-1%H_2 at 1100ºC for 6 h, the samples showed neither surface crack-disappearance nor strength recovery. It clarified that the oxidation of Ni particles at high temperatures induced the self-healing mechanism.

Results of the investigation for oxidation resistance indicated the Ni/mullite nanocomposites had a greater oxidation resistance than that of Ni/Al_2O_3 or Ni/(YZ+Al_2O_3). The oxidation of Ni within the mullite matrix created the significant formation of a surface layer composed of NiO, $NiAl_2O_4$ and Ni_2SiO_4. The oxidized zone was defined to be the region containing only the mullite matrix. The growth of oxidized zone obeyed the parabolic law with the apparent activation energy of 462 $kJmol^{-1}$. The growth rate of oxidized zone in Ni/mullite was one order of magnitude less than that of Ni/Al_2O_3. For mechanical properties of Ni/mullite nanocomposites, dispersion of Ni showed less effect on toughening of mullite matrix due to the intergranular fracture mechanism. The values of hardness and fracture toughness of Ni/mullite were comparable with that of monolithic mullite.

6.2 Suggestions for future works.

Self-healing function of ceramic-based composites are potential solutions for high-temperature applications. The composites could be utilized as an environmental barrier coating (EBC) layer for hot section components of gas turbine engines being used today, or even utilized as based materials in the further future. Nowadays, the components utilized in the hot section of gas turbine engines are made of Ni-based superalloys. The components are operated under a severe environment combined of high temperatures, complicate corrosion environment, high stresses such as fracture, creep, fatigue failures and so on. To survive at such high temperatures, thermal barrier coating layers and cooling methods are applied for the superalloys. Even though, the superalloys still can be operated at temperatures which almost reach to their melting temperature. With the demands for higher efficiency of gas turbine engines, development of novel materials which are able to withstand at higher temperatures is necessary.

SiC fiber reinforced SiC matrix composite (SiC/SiC) is one of the most promising ceramic matrix composites (CMC) for the high-temperature applications because of their outstanding properties. Over the past decades, numerous studies have been conducted to develop SiC/SiC composites which are expected to be utilized for the next generation of gas turbine engines. As a non-oxide ceramic, corrosion of SiC/SiC at high temperatures in the air/steam environments must be taken under advisement. SiC/SiC and other silica formers degrade with time in the high steam environment of the gas turbine combustor due to accelerated oxidation and subsequent volatilization of the silica due to reaction with high pressure water. As a result, an EBC is required in conjunction with the SiC/SiC composites in order to meet long life goals. In further future, novel CMC’s composed of oxide ceramics must be also developed for these applications. Self-healing ceramic-based composites could meet all the requirements of either EBC for SiC/SiC or the novel CMC’s in further future.

6.2.1 Development of self-healing ceramic composites for EBC.

Self-healing function of ceramic based composites could be excellent solutions for EBC layers which play a major role in protection of the substrate at high temperatures in corrosion environments. Cracking of the EBC layers induced by either foreign object damage or a time of operation could cause the degradation of their protection ability. With the self-healing ability of the EBC, cracks can be healed by itself at the operated conditions. Healing of cracks leads to the recovery of the EBC protection ability which is expected to extend their service life as described in Fig. 6.1.

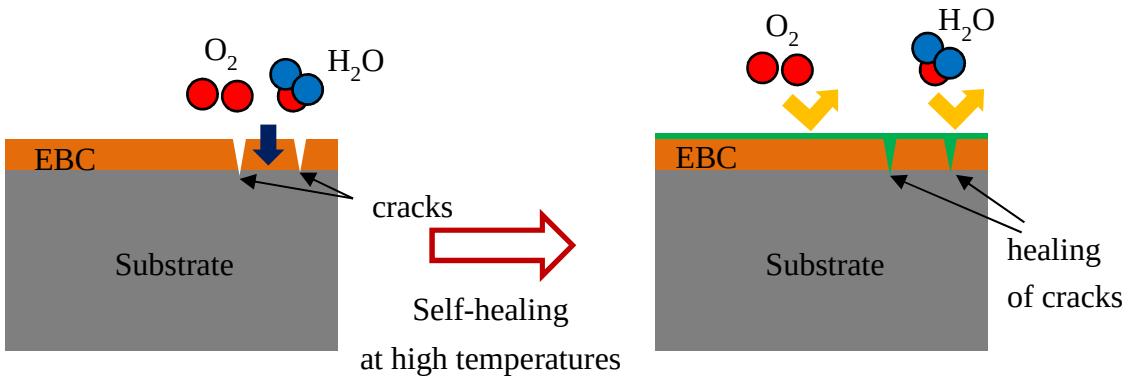

Fig. 6.1. Illustration describes the self-healing performance for EBC.

Some potential candidates for EBC are listed in Table 6.1. Dispersoids of metals such as Ni, Co, NiAl produce stable oxidation products at high temperatures. Nonetheless, the differences in coefficient of thermal expansion (CTE) between dispersoids and the matrices could be a biggest challenge in fabrications and operations of the composites. Some MAX phases exhibit excellent self-healing performance due to their protective oxidation products (Al_2O_3, ZrO_2, TiO_2 and so on). However, dispersion of these MAX phases in the matrices could degrade their oxidation resistance rapidly. For further applications, self-healing functions of these composites must be studied carefully.

Table 6.1. Potential candidates for EBC categorized by types of dispersoids and ceramic-based matrices.

Functions	Materials		Advantages	Disadvantages
Dispersoids	Metals	NiAl, Ni, Co	Great self-healing	CTE, density
	MAX phases	$Zr_2Al_4C_5$ Ti_2AlC_2	Protective oxidation products	Worse oxidation resistance
Ceramic-based matrix	Mullite ($3Al_2O_3.2SiO_2$)		CTE, Low cost production	Low mechanical properties.
	Yttrium silicate (Y_2SiO_5, Y_2SiO_7) Ytterbium silicate (Yb_2SiO_5)		CTE, excellent oxidation resistance	High cost production

6.2.2 Development of self-healing ceramic composites for hot section components.

As described in the previous section, corrosion and oxidation of the non-oxide ceramic matrix composites such as SiC/SiC CMC's and other silica formers must be concerned. The SiC/SiC CMC's still can be oxidized after a time of operation when the EBC loses their protection functions. Therefore, development of self-healing function of oxide ceramic-based composites for the hot section components is proposed as shown Figure 6.2.

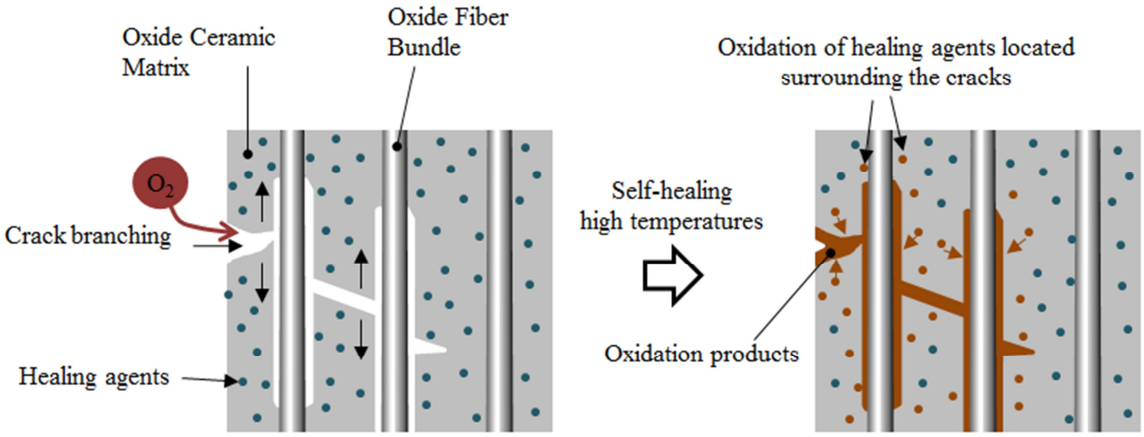

Fig. 6.2. Illustration describes the self-healing performance of oxide ceramic-based composites for the hot section components of gas turbine engines.

The potential candidates for the oxide ceramic matrix could be Al_2O_3, mullite and so on. Some possibilities for healing agents are metals (Ni, Co, NiAl) or some MAX phases

($Zr_2Al_4C_5$; Ti_2AlC_2). In consideration of mechanical properties at high temperatures for the matrices, multi-dispersions such as Ni-SiC, Ni-Si, Ni-$NiAl_2O_4$ could be potential solutions for the healing agents. To apply the self-healing ceramics for this purpose, a comprehensive study must be carried out with all aspects such as self-healing ability, oxidation behavior, and mechanical properties at high temperatures.

For expectations, the development of CMC's with self-healing function is expected to be a great solution for the high-temperature applications. With the self-healing ability, the novel EBC can have a greater protection function that results in longer service life, more reliability, lower maintaining and operating costs and so on. For a bright future, the hot section components can be made of self-healing ceramic composites which have excellent heat and corrosion resistance, greater-high temperature strength. Moreover, success of this study may bring many benefits and improvements for the next generation gas turbine engines which have higher efficiency, produce less CO_2 emission and so on.

References

[1] W. D. Kingery, H. K. Bowen and D. R. Uhlmann, Introduction to ceramics, New York: John Wiley & Sons, Inc., 1975.

[2] D. W. Budworth, An introduction to Ceramic Science, Oxford: Pergamon Press, 1970.

[3] D. W. Richerson, Modern Ceramic Engineering, Properties,Processing and Use in Design, Second Edition, New York: Marcel Dekker, INC, 1992.

[4] C. B. Carter and M. G. Norton, Ceramic Materials Science and Engineering, New York: Springer, 2013.

[5] R. J. E. Glenny, J. E. Northwood and A. B. Smith, "Materials for Gas Turbine," *International Metallurgical Reviews,* vol. 20, no. 1, pp. 1-28, 1975.

[6] B. B. Seth, "Supperalloys: The Utility Gas Turbine Perspective," *Superalloys 2000, TMS, Wrrendale,* pp. 3-16, 2000.

[7] M. Okazaki, "High-temperature strength of Ni-base superalloy coatings," *Science and Technology of Advanced Materials,* vol. 2, pp. 357-366, 2001.

[8] G. W. Meetham, "High Temperature Materials in Gas Turbine Engines," *Materials & Design,* vol. 9, no. 4, pp. 213-219, 1988.

[9] M. Yuri, J. Masada, K. Tsukagoshi, E. Ito and S. Hada, "Development of 1600C-Class High-efficiency Gas Turbine for Power Generation Applying J-Type Technology," *Mitsubishi Heavy Industries Technical Review,* vol. 50, no. 3, pp. 1-10, 2013.

[10] J. Cook, J. E. Gordon, C. C. Evans and D. M. Marsh, "A mechanism for the control of crack propagation in all-brittle systems," *Proceedings of the Royal society of London,* vol. 282, no. 1391, pp. 508-520, 1964.

[11] A. G. Evans, "Perspective on the Development of High-Toughness Ceramics," *Journal of the Amerincan Ceramic Society,* vol. 73, no. 2, pp. 187-206, 1990.

[12] M. P. Harmer, H. M. Chan and G. A. Miller, "Unique Opportunities for Microstructural Engineering with Duplex and Laminar Ceramic Composites," *Journal of the American Ceramic Society,* vol. 75, no. 7, pp. 1715-1728, 1992.

[13] Y. S. Chou and D. J. Green, "Silicon carbide platelet/alumina composites: III, toughening mechanism," *Journal of the American Ceramic Society,* vol. 76, no. 8, pp. 1985-1992, 1993.

[14] J. Liu, H. Yan and K. Jiang, "Mechnical properties of graphene platelet-reinforced alumina ceramic composites," *Ceramics International,* vol. 39, pp. 6215-6221, 2013.

[15] J. Dusza, J. Morgiel, A. Duszova, L. Kvetkova, M. Nosko, P. Kun and C. Balazsi, "Microstruccture and fracture toughness ofSi3N4 graphene platelet composites," *Journal of the European Ceramic Society,* vol. 32, pp. 3389-3397, 2012.

[16] J. Liu, H. Yan, M. J. Reece and K. Jiang, "Toughening of zirconia-alumina composites by the addition of graphene platelets," *Journal of the European Ceramic Society,* vol. 32, pp. 4185-4193, 2012.

[17] L. A. Simpson and A. Wasylyshyn, "Fractrue energy of Al2O3 containing Mo fibers," *Journal of the American Ceramic Society,* vol. 54, no. 1, pp. 56-57, 1971.

[18] P. F. Becher and G. C. Wei, "Toughening behavior in SiC-Whisker-reinforced alumina," *Journal of the American Ceramic Society,* vol. 62, no. 12, pp. C267-C269, 1984.

[19] K. W. White and L. Guazzone, "Elevated-temperature toughening mechanism in a SiCw/Al2O3 composite," *Journal of the American Ceramic Society,* vol. 74, no. 9, pp. 2280-2285, 1991.

[20] P. Hing and G. W. Groves, "The Strength and fracture toughness of polycrystalline magnesium oxide containing metallic particles and fibres," *Journal of Materials Science,* vol. 7, no. 4, pp. 427-434, 1972.

[21] T. Sekino, T. Nakajima, T. Ueda and K. Niihara, "Reduction and Sintering of a nickel-dispersed-alumina composite and its properties," *Journal of the American Ceramic Society,* vol. 80, no. 5, pp. 1139-1148, 1997.

[22] W. P. Tai and T. Wantanabe, "Preparation and mechanical properties of Al2O3 reinforced by submicrometer Co particles," *Journal of Materials Science,* vol. 33, no. 24, pp. 5795-5801, 1998.

[23] O. Abe, Y. Ohwa and Y. Kuranobu, "Possibitity of enhenced strength and self-recovery of surface damages of ceramics composites under oxidative conditions," *Journal of the European Ceramic Society,* vol. 26, no. 4-5, pp. 689-695, 2005.

[24] A. Sawaguchi, K. Toda and K. Niihara, "Mechanical and electrical properties of silicon nitride-silicon carbide nanocomposite material," *Journal of the American Ceramic Society,* vol. 74, no. 5, pp. 1142-1144, 1991.

[25] K. Niihara, A. Nakahira, T. Uchiyama and T. Hirai, "High-temperature mechanical properties of Al2O3-SiC composites," in *Fracture Mechanics of Ceramics, Vol 7*, R. C. Bradt, A. G. Evans, D. P. H. Hasselman and F. F. Lange, Eds., New York, Plenum Press, 1986, pp. 103-116.

[26] K. Niihara, "New design concept of structural ceramics. Ceramic nanocomposites," *Journal of Ceramic Society of Japan International Edition,* vol. 99, no. 10, pp.

945-952, 1991.

[27] G. Yamamoto, M. Omori, T. Hashida and H. Kimura, "A novel structure for carbon nanotube reinforced alumina composites with improved mechanical properties," *Nanotechnology,* vol. 19, p. 315708, 2008.

[28] K. Wang, Y. Wang, Z. Fan, J. Yan and T. Wei, "Preparation of graphene nanosheet/alumina composites by spark plasma sintering," *Materials Research Bulletin ,* vol. 46, pp. 315-318, 2011.

[29] O. Tapaszto, L. Tapaszto, M. Marko, F. Kern, R. Gadow and C. Balazsi, "Dispersion patterns of graphene and carbon nanotubes in ceramic matrix composites," *Chemical Physics Letters,* vol. 511, pp. 340-343, 2011.

[30] J. B. Wachtman, W. R. Cannon and M. J. Matthewson, Mechanical Properties of Ceramics, Second Edition, New Jersey: John Wiley & Sons, Inc, 2009.

[31] Q. Qin and J. Ye, Toughening Mechanisms in Composite Materials, Elsevier, 2015.

[32] I. W. Donald and P. W. McMillan, "Review Ceramic-matrix composites," *Journal of Materials Science,* vol. 11, pp. 949-972, 1976.

[33] W. Nakao, "Roles of high temperature oxidation in fiber reinforced self-healing ceramics," in *International Symposium on High-Temperature Oxidation and Corrosion*, Hakodate, Japan, June 25 2014.

[34] J. J. Petrovic and L. A. Jacobson, "Controlled Surface Flaws in Hot-Pressed SiC," *Journal of the American Ceramic Society,* vol. 59, no. 1-2, pp. 34-37, 1976.

[35] T. K. Gupta, "Crack Healing and Strengthening of Thermally Shocked Alumina," *Journal of the American Ceramic Society,* vol. 59, no. 5-6, pp. 259-262, 1976.

[36] S. R. Choi and V. Tikare, "Crack Healing Behavior of Hot Pressed Silicon Nitride Due to Oxidation," *Scripta Metallurgica et Materialia,* vol. 26, no. 8, pp. 1263-1268, 1992.

[37] M. C. Chu, S. Sato, Y. Kobayashi and K. Ando, "Damage healing and strengthening behaviour in intelligent mullite/SiC ceramics," *Fatigue & Fracture of Engineering Materials & Structures,* vol. 18, no. 9, pp. 1019-1029, 1995.

[38] P. Greil, "Generic principles of crack-healing ceramics," *Journal of Advanced Ceramics,* vol. 1, no. 4, pp. 249-267, 2012.

[39] S. Yoshioka and W. Nakao, "Methodology to evaluate availability of self-healing agent for structural ceramics," *Journal of Intelligent Material Systems and Structures,* p. 1045389X14544137, 2014.

[40] K. Houjou and K. Takahashi, "Crack-healing behavior of ZrO2/SiC composite ceramics and strength properties of crack-healing specimens," *International Journal*

of Structural Integrity, vol. 3, no. 1, pp. 41-52, 2012.

[41] X. P. Zhang, J. H. Ouyang, Z. G. Liu, Y. J. Wang and Y. Zhou, "Crack-healing behavior of hot-pressed TZ3Y20A-SiC ceramics," *Ceramics International,* vol. 40, pp. 6611-6615, 2014.

[42] K. W. Nam and J. R. Hwang, "The crack healing behavior of ZrO2/SiC composite ceramics with TiO2 additive," *Journal of Mechanical Science and Technology,* vol. 26, no. 7, pp. 2093-2096, 2012.

[43] G. M. Song, Y. T. Pei, W. G. Sloof, S. B. Li, J. T. M. De Hosson and S. v. d. Zwaag, "Oxidation-induced crack healing in Ti3AlC2 ceramics," *Scipta Materialia,* vol. 58, no. 1, pp. 13-16, 2008.

[44] G. Chen, R. Zhang, X. Zhang, L. Zhao and W. Han, "Oxidation-induced crack healing in Zr2Al4C5 ceramic," *Materials and Design,* vol. 30, no. 9, pp. 3602-3607, 2009.

[45] S. Li, L. Xiao, G. Song, X. Wu, W. G. Sloof and S. V. D. Zwaag, "Oxidation and Crack Healing Behavior of a Fine-Grained Cr2AlC Ceramic," *Journal or the American Ceramic Society,* vol. 96, no. 3, pp. 892-899, 2013.

[46] K. Takahashi, Y. S. Jung, Y. Nagoshi and K. Ando, "Crack-Healing Behavior of Si3N4/SiC Composite under Stress and Low Oxygen Pressure," *Materials Science and Engineering A ,* vol. 527, no. 15, pp. 3343-3348, 2010.

[47] M. Kasiarova, J. Dusza, M. Hnatko and P. Sajgalik, "Microstructure and Fracture-Mechanical Properties of Carbon Derived Si3N4+SiC Nanomaterials," *Materials Science and Engineering C,* vol. 26, no. 5-7, pp. 862-866, 2006.

[48] K. Ando, M. C. Chu, S. Matsushita and S. Sato, "Effect of Crack-Healing and Proof-Testing Procedures on Fatigue Strength and Reliability of Si3N4/SiC Composites," *Journal of the European Ceramic Society,* vol. 23, no. 6, pp. 977-984, 2003.

[49] F. Yao, K. Ando, M. C. Chu and S. Sato, "Static and cyclic fatigue behaviour of crack-healed Si3N4/SiC composite ceramics," *Journal of the European Ceramic Society,* vol. 21, no. 7, pp. 991-997, 2001.

[50] K. Ando, K. Houjyou, M. C. Chu, S. Takeshita, K. Takahashi, S. Sakamoto and S. Sata, "Crack-healing behavior of Si3N4/SiC ceramics under stress and fatigue strength at the temperature of healing (1000C)," *Journal of the European Ceramic Society,* vol. 22, no. 8, pp. 1339-1346, 2002.

[51] Z. Chlup, P. Flasar, A. Kotoji and I. Dlouhy, "Fracture behaviour of Al2O3/SiC nanocomposite ceramics after crack healing treatment," *Journal of the European Ceramic Society,* vol. 28, no. 5, pp. 1073-1077, 2008.

[52] K. Ando, B. S. Kim, M. C. Chu, S. Saito and K. Takahashi, "Crack-healing and mechanical behaviour of Al2O3/SiC composites at elevated temperature," *Fatigue & Fracture of Engineering Materials & Structures,* vol. 27, no. 7, pp. 533-541, 2004.

[53] T. Osada, W. Nakao, K. Takahashi, K. Ando and S. Saito, "Strength recovery behavior of machined Al2O3/SiC nano-composite ceramics by crack-healing," *Journal of the European Ceramic Society,* vol. 27, no. 10, pp. 3261-3267, 2007.

[54] I. A. Chou, H. M. Chan and M. P. Harmer, "Effect of Annealing Environment on the Crack Healing and Mechanical Behavior of Silicon Carbide-Reinforced Alumina Nanocomposites," *Journal of the American Ceramic Society,* vol. 81, no. 5, pp. 1203-1208, 1998.

[55] K. Takahashi, K. Uchiide, W. Nakao and K. Ando, "Crack-healing behavior of mullite/SiC multi-composite under stress," in *Proceeding of the First International Conference on Self Healing Materials*, Noordwijikaan Zee, The Netherlands, 18-20 April 2007.

[56] K. Ando, M. C. Chu, K. Tsuji, T. Hirasawa, T. Kobayyashi and S. Sato, "Crack healing behaviour and high-temperature strength of mullite/SiC composite ceramics," *Journal of the European Ceramic Society,* vol. 22, no. 8, pp. 1313-1319, 2002.

[57] K. Ando, K. Furusawa, M. C. Chu, T. Hanagata, K. Tuji and S. Sata, "Crack-Healing Behavior Under Stress of Mullite/Silicon Carbide Ceramics and the Resultant Fatigue Strength," *Journal of the American Ceramic Society,* vol. 84, no. 9, pp. 2073-2078, 2001.

[58] S. K. Lee, M. Ono, W. Nakao, K. Takahashi and K. Ando, "Crack-healing behaviour of mullite/SiC/Y2O3 composites and its application to the structural integrity of machined components," *Journal of the European Ceramic Society,* vol. 25, no. 15, pp. 3495-3502, 2005.

[59] F. Tavangarian and G. Li, "Crack healing and strength recovery in SiC/spinel nanocomposite," *Ceramics International ,* vol. 41, pp. 8702-8709, 2015.

[60] K. Takahashi, M. Yohouchi, S. K. Lee and K. Ando, "Crack-healing behavior of Al2O3 toughened by SiC whiskers," *Journal of the American Ceramic Society,* vol. 86, no. 12, pp. 2143-2147, 2003.

[61] W. Nakao, S. Mori, J. Nakamura, K. Takahashi, K. Ando and M. Yokouchi, "Self-crack-healing behaviorof mullite/SiC particle/SiC whisker multi-composites and potential use for ceramic springs," *Journal of the American Ceramic Society,* vol. 89, no. 4, pp. 1352-1357, 2006.

[62] L. Jun, Z. X. Zheng, H. F. Ding and Z. H. Jin, "Preliminary study of the crack healing

and strength recovery of Al2O3 matrix composites," *Fatigue & Fracture of Engineering Materials & Structures,* vol. 27, no. 2, pp. 89-97, 2004.

[63] G. P. Bei, B. J. Pedimonte, M. Pezoldt, J. Ast, T. Fey, M. Goeken and P. Greil, "Crack Healing in TiAl0.5Sn0.5C-Al2O3 composites," *Journal of the American Ceramic Society,* vol. 98, no. 5, pp. 1604-1610, 2015.

[64] D. Maruoka, Y. Sato and M. Nanko, "Recovery of mechanical properties on nano-Co particles dispersed Al2O3 via high-temperature oxidation," *Materials Transactions,* vol. 53, no. 10, pp. 1816-1821, 2012.

[65] A. L. Salas-Villasenor, J. Lemus-Ruiz, M. Nanko and D. Maruoka, "Crack-disappearance by high-temperature oxidation of alumina toughened by Ni nano-particles," *Advanced Materials Reseach,* vol. 68, pp. 34-43, 2009.

[66] M. Nanko, D. Maruoka and T. D. Nguyen , "Crack-healing function of metal/Al2O3 hybrid materials," *IOP Conf. Series: Materials Science and Engineering,* vol. 18, no. 082005, 2011.

[67] M. Nanko, D. Maruoka, V. H. Pham and D. T. Nguyen, "Crack Self-Repairing of Nano-Metal/Al2O3 Hybrid Materials," *Transactions on GIGAKU,* vol. 1, pp. 1022/1-6, 2012.

[68] X. P. Zhang, J. H. Ouyang, Z. G. Liu, Y. J. Wang and Y. M. Wang, "Crack-healing behavior and strength recovery of hot-pressed TZ3Y20A-MoSi2 Ceramics," *Materials Science and Engineering A,* vol. 648, pp. 299-304, 2015.

[69] S. Li, G. Bei, X. Chen, L. Zhang, Y. Zhou, M. Mackovic, E. Spiecker and P. Greil, "Crack healing induced electrical and mechanical properties recovery in a Ti2SnC ceramic," *Journal of the European Ceramic Society,* vol. 36, no. 1, pp. 25-32, 2016.

[70] G. Zhu, X. Wang, Q. Lu, G. Wu and P. Feng, "High-temperature crack-healing behaviour and strength recovery of (MoNb)Si2," *Applied surface Science ,* vol. 343, pp. 41-48, 2015.

[71] M. Nanko, "High-temperature oxidation of ceramic matrix composites dispersed with metallic particles," *Science and Technology of Advanced Materials,* vol. 6, pp. 129-134, 2005.

[72] M. Alagiri, C. Muthamizhchelvan and S. Ponnusamy, "Structural and magnetic properties of iron, cobalt and nickel nanoparticles," *Synthetic Metals,* vol. 161, no. 15-16, pp. 1776-1780, 2011.

[73] D. Maruoka and M. Nanko, "Influence of Si-Doping of Nano-Ni Dispersed Al2O3 Composites on High-Temperature oxidation," *Materials Transactions,* vol. 51, no. 9, pp. 1570-1573, 2010.

[74] D. Maruoka, Y. Sato and M. Nanko, "Crack-healing Effectiveness of Nano Ni+SiC Co-Dispersed Alumina Hybrid Materials," *Advanced Materials Research,* Vols. 89-91, pp. 365-370, 2010.

[75] D. Maruoka and M. Nanko, "Crack Healing of Nano-Ni/Al2O3 Hybrid Materials via High-Temperature Oxidation," *Materials Science Forum,* vol. 696, pp. 378-383, 2011.

[76] D. Maruoka and M. Nanko, "Recovery of mechanical strength by surface crack disappearance via thermal oxidation for nano-Ni.Al2O3 hybrid materials," *Ceramics International,* vol. 39, no. 3, pp. 3221-3229, 2013.

[77] K. Niihara, R. Morena and D. P. H. Hasselman, "Evaluation of K1C of brittle solids by indentation method with low crack-to-indent ratios," *Journal of Materials Science Letters,* vol. 1, pp. 13-16, 1982.

[78] R. Z. Chen and W. H. Tuan, "Pressureless Sintering of Al2O3/Ni Nanocomposites," *Journal of the European Ceramic Society,* vol. 19, no. 4, pp. 463-468, 1999.

[79] J. Lu, L. Gao, J. Sun, L. Gui and J. Guo, "Effect of nickel content on the sintering behavior, mechanical and dielectric properties of Al2O3/Ni composites from coated powders," *Materials Science and Engineering A,* vol. 293, pp. 223-228, 2000.

[80] B. S. Kim, T. Sekino, T. Nakayama, M. Wada, J. S. Lee and K. Niihara, "Pulse electric current sintering of alumina/nickel nanocomposites," *Materials Research Innovations,* vol. 7, no. 2, pp. 57-61, 2003.

[81] R. G. Munro, "Evaluated Material Properties for a Sintered alpha-Alumina," *Journal of the American Ceramic Society,* vol. 80, no. 8, pp. 1919-28, 1997.

[82] K. P. Trumble and M. Ruhle, "The thermodynamics of spinel interphase formation at diffusion-bonded Ni/Al2O3 interfaces," *Acta Metallurgica et Materialia,* vol. 39, pp. 1915-1924, 1991.

[83] A. G. Evans and W. Blumenthal, "High temperature failure mechanisms in ceramic polycrystals," in *Deformation of Ceramic Materials II*, New York, Plenum Press, 1984, pp. 487-505.

[84] T. Sekino, T. Nakajima, S. Mihara, S. Ueda and K. Niihara, "Interface structure of ceramic/metal nanocomposites," in *Materials Processing and Design: Grain-Boundary-Controlled Properties of Fine Ceramics II*, Westerville, American Ceramic Society, 1994, pp. 243-251.

[85] R. Z. Chen and W. H. Tuan, "Interfacial fracture energy of Al2O3/Ni nanocomposites," *Journal of Materials Science Letters,* vol. 20, pp. 2029-2030, 2001.

[86] S. Jiao, M. L. Jenkins and R. W. Davidge, "Interfacial fracture energy-mechanical behaviour relationship in Al2O3/SiC and Al2O3/TiN nanocomposites," *Acta*

Materialia, vol. 45, no. 1, pp. 149-156, 1997.

[87] Y. Maehara and T. G. Langdon, "Review: Superplasticity in Ceramcis," *Journal of Materials Science,* vol. 25, pp. 2275-2286, 1990.

[88] F. Wakai, "Superplasticity of Ceramics," *Ceramics International,* vol. 17, no. 3, pp. 153-163, 1991.

[89] Y. Yoshizawa and T. Sakuma, "High-temperature deformation and cavitation in fine-grained alumina," *Materials Science and Engineering A,* vol. 176, pp. 447-453, 1994.

[90] L. A. Xue and I. W. Chen, "Superplastic Alumina at Temperatures below1300C Using Charge-Compensating Dopants," *Journal of the American Ceramic Society,* vol. 79, no. 1, pp. 233-38, 1996.

[91] L. A. Xue and I. W. Chen, "Deformation and grain growth of low-temperature-sintered high-purity alumina," *Journal of the American Ceramic Society,* vol. 73, no. 11, pp. 3518-21, 1990.

[92] M. Nanko, M. Mizumo, M. Watanabe, K. Matsumaru and K. Ishizaki, "High-temperature oxidation of nano-Ni dispersed Al2O3 composites in air," *Advances in Technology of Meterials and Materials Processing Journal,* vol. 6, no. 2, pp. 240-243, 2004.

[93] R. C. Garvie, R. H. Hannink and R. T. Pascoe, "Ceramic steel," *Nature,* vol. 258, pp. 703-704, 1975.

[94] P. M. Kelly and L. R. Francis Rose, "The martensitic transformation in ceramics-its role in transformantion toughening," *Progress in Materials Science,* vol. 47, pp. 463-557, 2002.

[95] R. Z. Chen, Y. T. Chiu and W. H. Tuan, "Toughening alumina with both nickel and zirconia inclusions," *Journal of the European Ceramic Society,* vol. 20, pp. 1901-1906, 2000.

[96] C. Pascual, J. R. Jurado and P. Duran, "Electrical behaviour of doped-yttria stabilized zirconia ceramic materials," *Journal of Materials Science,* vol. 18, pp. 1315-1322, 1983.

[97] A. Eichler, "Tetragonal Y-doped zirconia: Structure and ion conductivity," *Physical Review B,* vol. 64, p. 174103, 2001.

[98] M. Nanko, M. Yoshimura and T. Maruyama, "High temperature oxidation of Y2O3 partially stabilized ZrO2 composites dispersed with Ni particles," *Materials Transactions,* vol. 44, pp. 736-742, 2003.

[99] R. O. Ritchie, "The conflicts between strength and toughness," *Nature Materials,* vol. 10, pp. 817-822, 2011.

[100] F. Bouville, E. Maire, S. Meille, B. Van de Moortele, A. J. Stevenson and S. Deville, "Strong, tough and stiff bioinspired ceramics from brittle constituents," *Nature Materials,* vol. 13, pp. 508-514, 2014.

[101] M. Lieberthal and W. D. Kaplan, "Processing and properties of Al2O3 nanocomposites reinforced with sub-micron Ni and NiAl2O4," *Materials Science and Engineering A,* vol. 302, pp. 83-91, 2001.

[102] T. Isobe, K. Daimon, K. Ito, T. Matsubara, Y. Hikichi and T. Ota, "Preparation and properties of Al2O3/Ni composite from NiAl2O4 spinel by in situ reaction sintering method," *Ceramic International,* vol. 33, pp. 1211-1215, 2007.

[103] T. Isobe, K. Daimon, T. Sato, T. Matsubara, Y. Hikichi and T. Ota, "Spark plasma sintering technique for reaction sintering of Al2O3/Ni nanocomposite and its mechanical properties," *Ceramics International,* vol. 34, pp. 213-217, 2008.

[104] U. Leela-adisorn, T. Matsunaga, Y. Kobayashi, S. M. Choi and H. Awaji, "Soaking method for fabrication of alumina-based nanocomposites," *Ceramic International,* vol. 31, pp. 803-809, 2005.

[105] W. S. Chang, S. Chen and P. Shen, "Phase Equilibria of zirconia-dispersed ceramic in NiO-Al2O3-ZrO2 system," *Materials Science and Engineering A,* vol. 145, pp. 113-118, 1991.

[106] K. Kowalski, A. Bernasik and A. Sadowshi, "Bulk and grain boundary diffusion of titanium in yttria-stabilized zirconia," *Journal of the European Ceramic Society,* vol. 20, no. 7, pp. 951-958, 2000.

[107] P. A. Lessing and R. S. Gordon, "Impurity and grain size effects on te creep of polycrystalline magnesia and alumina," in *Deformation of Ceramic Materials*, New York, Plenum Press, 1975, pp. 271-296.

[108] K. L. Luthra and H. D. Park, "Oxidation of Silicon Carbide-Reinforced Oxide-Matrix Composites at 1375 to 1575C," *Journal of the American Ceramic Society,* vol. 73, no. 4, pp. 1014-23, 1990.

[109] P. A. Lessing, R. S. Gordon and K. S. Mazdiyasni, "Creep of polycrystalline mullite," *Journal of the American Ceramic Society,* vol. 58, no. 3-4, p. 149, 1975.

Research Activities

List of papers

1. H. V. Pham and M. Nanko, “Crack-Healing Function of nano-Ni/(ZrO_2+Al_2O_3) Hybrid Materials”, Materials Science Forum, Vol. 804, 179-182 (2014). Doi: 10.4028/www.scientific.net/MSF.804.179
2. H. V. Pham and M. Nanko, “Self-healing and mechanical properties of reinforced nickel-dispersed alumina hybrid nanocomposites”, Journal of Ceramic Processing Research, Vol. 16, No. 5, 468-471 (2015).
3. H. V. Pham, D. Maruoka and M. Nanko, “Influences of Al_2O_3 Grain size on High-temperature Oxidation of nano-Ni/Al_2O_3 Composites”, Journal of Asian Ceramic Societies, Vol. 4, 120-123 (2016). Doi:10.1016/j.jascer.2016.01.003
4. H. V. Pham, M. Nanko and W. Nakao, “High-temperature Bending Strength of Self-healing Ni/Al_2O_3 Nanocomposites”, International Journal of Applied Ceramic Technology, in review.

List of International Conferences

1. Pham V. Hai and Nanko Makoto, Crack-healing function of nano-Ni/(ZrO_2+Al_2O_3) hybrid materials, the International Symposium on Eco-Materials Processing Design (ISEPD2014), Hanoi, Vietnam, Jan. 2014.
2. V. Hai Pham and Makoto Nanko, Crack-healing improvements on nano Ni dispersed Al_2O_3 hybrid materials, The 3rd International GIGAKU Conference in Nagaoka, Nagaoka, Japan, Jun. 2014.
3. Hai V. Pham, Daisuke Maruoka and Makoto Nanko, Influence of Al_2O_3 matrix on Crack-healing function and high temperature oxidation of nano-Ni/Al_2O_3 composites, International Symposium on High-temperature Oxidation and Corrosion (ISHOC2014), Hakodate, Japan, Jun. 2014.
4. V. Hai Pham and Makoto Nanko, Crack-healing function of Alumina Hybrid Materials with Co-dispersion of Nano-Ni and ZrO_2, The International Conference on Materials Science and Engineering, Darmstadt, Germany, Sep. 2014.
5. V. H. Pham and M. Nanko, Self-healing and mechanical properties of nickel dispersed alumina hybrid nanocomposites, The 3rd International Symposium on Hybrid Materials and Processing, Busan, Korea, Nov. 2014.
6. V. Hai Pham and Makoto Nanko, Mechanical Recovery of 5 vol% Ni/Mullite via Oxidation at High-Temperatures, The Fifth International Conference on Self-Healing Materials, NC, United States, Jun. 2015.
7. V. H. Pham and M. Nanko, High-temperature oxidation of 5 vol% Ni/mullite, Gordon Research Conference on High Temperature Corrosion, NH, United States, Jul. 2015.
8. V. Hai Pham and Makoto Nanko, High-temperature bending strength of self-healing Ni/(ZrO_2+Al_2O_3) nanocomposite, The International Conference on Materials Science and Technology (MS&T2015), OH, United States, Oct. 2015.
9. V. Hai Pham and Makoto Nanko, High-temperature bending strength of self-healing

Ni/Al_2O_3 nanocomposite, The Third International Conference on Powder Metallurgy in Asia (APMA2015), Kyoto, Japan, Nov. 2015.

10. Hai V. Pham and Makoto Nanko, Influence of ZrO_2 dispersion on High-temperature strength of Ni/Al_2O_3 nanocomposites, The 32^{nd} International Japan-Korea Seminar on Ceramics (JK-Ceramics 32), Nagaoka, Japan, Nov. 2015.

List of Domestic Conferences

1. Pham V. Hai and Nanko Makoto, Crack-healing function of Alumina hybrid materials with co-dispersion of Ni and ZrO_2, Fall Meeting of the Japan Institute of Metals and Materials, Kanazawa, Ishikawa, Sep. 2013.
2. Pham V. Hai and Nanko Makoto, Crack disappearance of nano-nickel and zirconia co-dispersed alumina composites via thermal oxidation, Annual Meeting of the Japan Society of Mechanical Engineers (M&P2013), Tokyo, Nov. 2013.
3. Pham V. Hai and Nanko Makoto, Mechanical properties of nano-Ni/Al_2O_3 toughened by ZrO_2 dispersion, Branch Meeting of the Japan Institute of Metals and Materials, Nagano, Dec. 2013.
4. Pham V. Hai and Nanko Makoto, Grain size influence of alumina matrix on crack-healing function of nano-Ni/Al_2O_3 hybrid materials, Spring Meeting of the Japan Institute of Metals and Materials, Tokyo, Mar. 2014.
5. Hai V. Pham and Makoto Nanko, Crack Disappearance and Mechanical Recovery of Ni/(ZrO_2+Al_2O_3) Nanocomposite, Annual Meeting of the Japan Society of Mechanical Engineers (M&P2014), Tokyo, Sep. 2014
6. Pham V. Hai and Nanko Makoto, Surface Crack-disappearance of Ni/Mullite Composite via High Temperature Oxidation, Branch Meeting of the Japan Institute of Metals and Materials, Niigata, Dec. 2014.
7. Pham V. Hai and Nanko Makoto, High Temperature Oxidation of Ni/Al_2O_3 Nanocomposites with Different Al_2O_3 Grain Size, Spring Meeting of the Japan Institute of Metals and Materials, Tokyo, Mar. 2015.
8. Pham V. Hai and Nanko Makoto, Mechanical Properties and Microstructure of Metal/Oxide Nanocomposites Produced by Pulsed Electric Current Sintering, Annual Meeting of the Japan Society of Mechanical Engineers (M&P2015), Hiroshima, Nov. 2015.

Honor and Awards

1. H. V. Pham and M. Nanko, Poster Award 3rd Prize, The International Conference on Materials Science and Engineering, Darmstadt, Germany, Sep. 2014.
2. H. V. Pham and M. Nanko, Outstanding Paper Award, The 3rd International Symposium on Hybrid Materials and Processing, Busan, Korea, Nov. 2014.
3. H. V. Pham and M. Nanko, Best Poster Award Student 3rd Place, Gordon Research Conference on High Temperature Corrosion, NH, United States, Jul. 2015.